DISS. ETH NO. 30224

ENHANCING PHYSICAL INTERACTIONS OF UNTETHERED MINIATURE MAGNETIC ROBOTS FOR BIOMEDICAL APPLICATIONS

A thesis submitted to attain the degree of

DOCTOR OF SCIENCES

(Dr. sc. ETH Zurich)

presented by

Ren Hao Soon

Master of Engineering, National University of Singapore

born on 21 October 1992

accepted on the recommendation of

Prof. Dr. Metin Sitti, Examiner

Prof. Dr. Mehmet Fatih Yanik, Co-examiner

Prof. Dr. Jiachen Zhang, Co-examiner

2024

Acknowledgements

I would like to take the opportunity to sincerely thank the following groups of people for the successful completion of my PhD.

Firstly, my family. I would like to thank them for their never-ending support and love. I am grateful to have such a supportive family. They are always unconditionally there for me and never once questioned my decision to pursue my dreams, however difficult it might have been for them. I only hope that I will be able to make it up to them someday somehow.

Secondly, my friends. I will refrain from thanking individuals here because it would be unfair to list anyone in any order. Not to mention they would give me hell if I forgot them… you know who you are. It has been a remarkable 4.5 years. Leaving family to live in a foreign land is never easy, but knowing them definitely made things more fun and less lonely.

Thirdly, my collaborators, supervisor Prof. Metin Sitti, technical and administrative staff and the Max Planck Society for their funding and support of my research. Without their belief in the value of engaging in high risk-high reward research and support, I wouldn't have had the time, space or resources to fully investigate my ideas. There were multiple failed attempts before this research came to fruition – what is shown is only the small, successful part of the research. In particular, Metin never discouraged me from tackling any research question I found interesting, nor did he stop me from purchasing any equipment necessary for my research. Even when the research wasn't going to plan or according to schedule, he continued believing in me and my abilities. For that, I am really thankful.

I dedicate this thesis to my family and to anyone who manages to finish reading it.

Ren Hao Soon

Stuttgart, January 2024

Abstract

Untethered miniature robots can harvest energy made available to them remotely, such as light, magnetic or acoustic energy, and convert them to other forms of energy, such as mechanical deformation. Magnetic actuation, in particular, has emerged as a promising method for robots in biomedical applications due to the magnetic field's ability to penetrate human tissues safely. Advancements in the field have enabled these robots to navigate precisely to a target site on land or in fluid-filled confined environments, while carrying payloads, such as drugs, genes, hydrogel structures and even patient cells for therapeutic applications. Despite these advances, the use of miniature magnetic robots in clinical applications is severely limited because only one form of functionality, namely the shape-morphing capability of the robot for locomotion or cargo delivery to tissue surfaces, is typically utilised. This work aims to overcome this lack of diversity in functionalities by proposing several methods which can be readily adopted on existing untethered miniature magnetic robots, actively triggered on demand and independently controlled, to enable advanced physical interactions between the robot and tissue. Such capabilities pave the way for the development of next-generation magnetic miniature soft robots capable of addressing real-world clinical applications.

To achieve this, a two-pronged strategy is adopted. Firstly, the "fully soft" assumption of such robots is challenged. Currently, there exists an assumption that the robots have to be fully soft for enhanced safety, or for continuum motion to be achieved. However, this imposes a significant, and sometimes unnecessary, constraint on these robots – especially since rigid materials exhibit certain material properties that are desirable and superior to soft materials. Secondly, high-frequency magnetic fields are utilised, to expand the number of control, and hence design parameters. Although the profile and magnitude of magnetic fields have been extensively exploited to achieve different locomotion modes, the effects of changing the frequency of the magnetic fields have been less explored. At such frequencies, specifically in the kHz regime, the magnetic fields still remain safe for human exposure, whilst being too high for actuation, thereby avoiding any interference with the robot's locomotion. As such, by relaxing these constraints, coupled with novel mechanical designs and implementation, advanced functionalities can be achieved to further enhance the capabilities of these robots. Three new functionalities for these robots are developed based on this strategy.

In the first part, we demonstrate a significant improvement in the force capabilities of these robots. Specifically, we propose a wireless spring-preloaded barbed needle release mechanism, which can provide up to 1.6 N of force to drive a barbed needle into soft tissues to allow robust on-demand anchoring on three-dimensional (3D) surfaces. The mechanism is wirelessly triggered using radiofrequency (RF) remote heating and can be easily integrated into existing untethered soft robotic platforms without sacrificing their mobility. Design guidelines aimed at maximising anchoring over the range of the most biological tissues (kPa range) and extending the operating depth of the device inside the body (up to 75%) are also presented. Enabled by these advances, we achieve robust anchoring on a variety of ex vivo tissues and demonstrate the usage of such a device when integrated with existing soft robotic platforms and medical imaging. Moreover, by simply changing the needle, additional functionalities such as controlled detachment and sub-surface drug delivery into 3D cancer spheroids are also demonstrated.

In the second part, we propose a design that enables substantial heat generation in an untethered miniature robotic system. Such a capability had not been developed because there is an inherent trade-off between effective remote heating at long distances and compliance. Specifically, rigid metallic body parts should be used for remote heating to ensure that the electrical conductivity and geometrical properties remain constant and stable for enhanced and reliable remote heating via Joule heating, yet the use of rigid materials inherently restricts and compromises the compliance of such untethered soft robots. The pangolin-inspired design introduced in this work allows users to achieve significant heating ($\Delta T > 70$ °C) at large distances (> 5 cm) within a short period of time (< 30 s), thereby realising on-demand localised heating in tandem with shape-morphing capabilities. Endowed with this new capability, advanced robotic functionalities, such as selective cargo release, in situ demagnetisation, hyperthermia and mitigation of bleeding, are demonstrated on tissue phantoms and ex vivo tissues.

In the final part, we demonstrate how electricity can be directly harvested and utilised in an untethered miniature robotic system. Electricity is one of the most widely used and versatile form of energy but there exist few miniature robotic systems which possess such a functionality. The size and weight constraints makes it difficult to implement conventional electronics such as batteries on these robots. Even in cases where such systems are demonstrated, the proposed solutions suffered from various practical and feasibility issues. These limitations include, but are

not limited to, a short working range or a requiring a specific set of environmental conditions, which greatly restricts their use to niche applications. To address this, we propose an untethered miniature robotic system which generates electricity by exploiting high-frequency magnetic fields. Magnetic fields can safely penetrate the body and can as such, allow power to be wirelessly transmitted across distances into the body. This in turn unlocks a wide range of potential applications for these robotic systems. While there has been extensive research into wireless power transfer systems, none of them had focused on their applicability to miniature untethered robotic systems.

Zusammenfassung

Ungebundene Miniaturroboter können die ihnen aus der Ferne zur Verfügung gestellte Energie, z. B. Licht, magnetische oder akustische Energie, nutzen und sie in andere Energieformen, z. B. mechanische Verformung, umwandeln. Insbesondere die magnetische Betätigung hat sich als vielversprechende Methode für Roboter in biomedizinischen Anwendungen erwiesen, da das Magnetfeld das menschliche Gewebe sicher durchdringen kann. Fortschritte auf diesem Gebiet haben es diesen Robotern ermöglicht, an Land oder in flüssigkeitsgefüllten, begrenzten Umgebungen präzise zu einem Zielort zu navigieren und dabei Nutzlasten wie Medikamente, Gene, Hydrogelstrukturen und sogar Patientenzellen für therapeutische Anwendungen zu transportieren. Trotz dieser Fortschritte ist der Einsatz von magnetischen Miniaturrobotern in klinischen Anwendungen stark eingeschränkt, da in der Regel nur eine Form der Funktionalität genutzt wird, nämlich die Fähigkeit des Roboters, seine Form zu verändern, um sich fortzubewegen oder Ladungen an Gewebeoberflächen zu transportieren. Diese Arbeit zielt darauf ab, diesen Mangel an Funktionsvielfalt zu überwinden, indem sie mehrere Methoden vorschlägt, die leicht auf bestehende ungebundene Miniatur-Magnetroboter übertragen werden können, die bei Bedarf aktiv ausgelöst und unabhängig gesteuert werden, um fortgeschrittene physische Interaktionen zwischen dem Roboter und dem Gewebe zu ermöglichen. Diese Fähigkeiten ebnen den Weg für die Entwicklung von magnetischen Miniatur-Softrobotern der nächsten Generation, die für reale klinische Anwendungen geeignet sind.

Um dies zu erreichen, wird eine zweigleisige Strategie verfolgt. Erstens wird die Annahme, dass solche Roboter „völlig weich“ sind, in Frage gestellt. Derzeit wird davon ausgegangen, dass die Roboter vollständig weich sein müssen, um die Sicherheit zu erhöhen oder um eine kontinuierliche Bewegung zu ermöglichen. Dies stellt jedoch eine erhebliche und manchmal unnötige Einschränkung für diese Roboter dar, zumal starre Materialien bestimmte Materialeigenschaften aufweisen, die wünschenswert und weichen Materialien überlegen sind. Zweitens werden Hochfrequenz-Magnetfelder eingesetzt, um die Zahl der Steuerungs- und damit der Konstruktionsparameter zu erweitern. Obwohl das Profil und die Stärke von Magnetfeldern ausgiebig genutzt wurden, um verschiedene Fortbewegungsarten zu erreichen, wurden die Auswirkungen einer Änderung der Frequenz der Magnetfelder weniger erforscht. Bei solchen Frequenzen, insbesondere im kHz-Bereich, sind die Magnetfelder für den Menschen immer noch

ungefährlich, während sie für die Betätigung zu hoch sind, so dass eine Beeinträchtigung der Fortbewegung des Roboters vermieden wird. Durch die Lockerung dieser Beschränkungen in Verbindung mit neuartigen mechanischen Konstruktionen und Implementierungen können fortschrittliche Funktionen erreicht werden, die die Fähigkeiten dieser Roboter weiter verbessern. Auf der Grundlage dieser Strategie werden drei neue Funktionalitäten für diese Roboter entwickelt.

Im ersten Teil zeigen wir eine deutliche Verbesserung der Kraftfähigkeiten dieser Roboter. Konkret schlagen wir einen kabellosen, federgespannten Auslösemechanismus für eine Widerhakennadel vor, der eine Kraft von bis zu 1,6 N aufbringen kann, um eine Widerhakennadel in weiches Gewebe zu stoßen und eine robuste Verankerung auf dreidimensionalen (3D) Oberflächen zu ermöglichen. Der Mechanismus wird drahtlos über eine Hochfrequenz-Fernheizung ausgelöst und lässt sich problemlos in bestehende, ungefesselte Softroboter-Plattformen integrieren, ohne deren Mobilität zu beeinträchtigen. Außerdem werden Konstruktionsrichtlinien vorgestellt, die darauf abzielen, die Verankerung im Bereich der meisten biologischen Gewebe (kPa-Bereich) zu maximieren und die Betriebstiefe des Geräts innerhalb des Körpers (bis zu 75 %) zu erweitern. Mit diesen Fortschritten erreichen wir eine robuste Verankerung in einer Vielzahl von Ex-vivo-Geweben und demonstrieren die Verwendung eines solchen Geräts, wenn es in bestehende Soft-Roboter-Plattformen und medizinische Bildgebung integriert wird. Darüber hinaus werden durch einen einfachen Wechsel der Nadel zusätzliche Funktionen wie die kontrollierte Ablösung und die Verabreichung von Medikamenten unter der Oberfläche in 3D-Krebs-Sphäroide demonstriert.

Im zweiten Teil schlagen wir ein Design vor, das eine erhebliche Wärmeerzeugung in einem ungefesselten Miniaturrobotersystem ermöglicht. Eine solche Fähigkeit wurde bisher nicht entwickelt, da es einen inhärenten Kompromiss zwischen effektiver Fernheizung über große Entfernungen und Nachgiebigkeit gibt. Insbesondere sollten starre metallische Körperteile für die Fernbeheizung verwendet werden, um sicherzustellen, dass die elektrische Leitfähigkeit und die geometrischen Eigenschaften konstant und stabil bleiben, damit eine verbesserte und zuverlässige Fernbeheizung über Joule-Heizung möglich ist; die Verwendung starrer Materialien schränkt jedoch die Nachgiebigkeit solcher ungefesselter weicher Roboter von Natur aus ein. Das in dieser Arbeit vorgestellte, vom Schuppentier inspirierte Design ermöglicht es den Nutzern, in kurzer Zeit

(< 30 s) eine signifikante Erwärmung (ΔT > 70 °C) über große Entfernungen (> 5 cm) zu erreichen und so eine bedarfsgerechte lokale Erwärmung in Verbindung mit Formveränderungsfähigkeiten zu realisieren. Ausgestattet mit dieser neuen Fähigkeit werden fortschrittliche Roboterfunktionen wie selektive Freisetzung von Ladung, In-situ-Entmagnetisierung, Hyperthermie und Blutungsminderung an Gewebephantomen und Ex-vivo-Geweben demonstriert.

Im letzten Teil demonstrieren wir, wie Elektrizität direkt in einem ungebundenen Miniaturrobotersystem gewonnen und genutzt werden kann. Elektrizität ist eine der am weitesten verbreiteten und vielseitigsten Energieformen, aber es gibt nur wenige Miniaturrobotersysteme, die über eine solche Funktionalität verfügen. Aufgrund der Größen- und Gewichtsbeschränkungen ist es schwierig, herkömmliche Elektronik wie Batterien in diesen Robotern zu implementieren. Selbst in den Fällen, in denen solche Systeme gezeigt wurden, litten die vorgeschlagenen Lösungen unter verschiedenen praktischen und machbaren Problemen. Zu diesen Einschränkungen gehören u. a. eine geringe Reichweite oder die Notwendigkeit, bestimmte Umgebungsbedingungen zu erfüllen, was ihre Verwendung auf Nischenanwendungen stark einschränkt. Um dieses Problem zu lösen, schlagen wir ein ungefesseltes Miniaturrobotersystem vor, das Elektrizität durch die Nutzung hochfrequenter Magnetfelder erzeugt. Magnetfelder können den Körper sicher durchdringen und ermöglichen so die drahtlose Übertragung von Strom über große Entfernungen in den Körper. Dies wiederum eröffnet eine breite Palette potenzieller Anwendungen für diese Robotersysteme. Es gibt zwar umfangreiche Forschungsarbeiten zu drahtlosen Energieübertragungssystemen, aber keine davon konzentrierte sich auf ihre Anwendbarkeit für ungebundene Miniaturrobotersysteme.

Contents

Nomenclature

a	Acceleration	p	Pressure
A	Magnetic vector potential	P	Power
$A_{\perp}$	Area (perpendicular)	P_{in}	Induced power
b	Breadth	R_S	Source resistance
B	Magnetic flux density	t	Time
c_p	Specific heat capacity (constant pressure)	T	Temperature
C	Electric scalar potential	V	Volume
C_D	Drag coefficient	V_F	Volume fraction
d	Distance to RF coil	V_{in}	Induced voltage
D	Distance to substrate	w	Thickness
E	Young’s modulus	w_d	Deflection of beam
E_{FC}	Flexural chord modulus of elasticity	x_n	Displacement at point n
f	Frequency	α	Thermal diffusivity
F	Force	β	Coefficient of thermal expansion
h	Convective heat transfer coefficient	δ	Skin depth
H_L	Heat loss	ϵ	Surface emissivity
I	Electrical current	η	Kinematic viscosity
I_{2nd}	Second moment of area	μ	Permeability
J	Current density	μ_k	Kinetic friction coefficient
k	Thermal conductivity	μ_S	Static friction coefficient
k_{sp}	Spring constant	ρ	Density
L	Length	σ	Electrical conductivity
m	Mass	τ	Torque
m_{mag}	Magnetic moment	Φ	Angle (orientation)
M_B	Bending moment	ϕ	Angle (sample to field)
n	Sample size		
N	Normal force		

List of Figures

List of Tables

Preface

This dissertation is a compilation of three papers which have been edited for brevity and clarity.

1) **R H Soon**, Z Ren, W Hu, U Bozuyuk, E Yildiz, M Li, M Sitti On-demand anchoring of wireless soft miniature robots on soft surfaces *Proceedings of the National Academy of Sciences*, 119 (34) e2207767119, 2022.
2) **R H Soon**, Z Yin, M A Dogan, N O Dogan, M E Tiryaki, A C Karacakol, A Aydın, P Esmaeili-Dokht, M Sitti Pangolin-inspired untethered magnetic robot for on-demand biomedical heating applications *Nature Communications*, 14(1), 3320, 2023.
3) **R H Soon,** P Esmaeili-Dokht, J Martus, A Aydın, M Sitti Untethered electrical magnetic robot for on-demand multi-functional biomedical applications *(in preparation)*.

Chapter 1: Introduction

1.1 Background

Untethered miniature robots, whose size typically range from several tens of micrometres up to several centimetres [1], have great potential in minimally invasive medical applications. Being untethered, these robots can easily navigate to inaccessible, high-risk regions inside the body, potentially opening up new avenues for clinicians to conduct minimally invasive procedures. One such area inside the body is the small intestine in the gastrointestinal (GI) tract. Although the endoscope and colonoscope allows for non-invasive access into parts of the GI tract for observation and procedures to be performed, a large part of the GI tract, namely the small intestine, still remains inaccessible to these surgical devices – the endoscope can only reach up until the jejunum while the colonoscope can cover the entire large intestine but cannot enter the small intestine. The tortuous nature of the small intestine hinders the navigation of tethered devices in confined spaces. Deeper insertion of the endoscope into regions after the jejunum is often limited by buckling and looping of the scope in the stomach [2]. As such, most of the small intestine (i.e. ileum, which is 3 m long on average) still remains inaccessible to these surgical tools, preventing interventional procedures such as localised drug delivery, hyperthermia and disease monitoring among others, from being performed. An untethered miniature robot which can perform these tasks where conventional medical instruments find hard to access would, therefore, be of great value and complement existing treatment strategies.

Untethered miniature robots can generally be designed with one of the two design philosophies: on-board and off-board approach. In the former, the robot is essentially a miniaturised version of a conventional robot and carries all components in a self-contained unit. This allows the robot to navigate in an open, ill-defined environment and allows the robot to function independently, without the need for any supporting infrastructure. On the other hand, in the off-board approach, the robots work by harvesting energy made available to them remotely, such as light, magnetic or acoustic energy, and converting them to other forms of energy, such as mechanical deformation. An off-board design approach, therefore, allows certain robotic components such as the power source, electronics and/or control system to be moved out of the robot. In doing so, these robots are made smaller but yet in a simpler fashion than an equivalent system – in terms of scale and function – designed using a conventional on-board approach where the robot has to carry everything itself. This allows the robot to be further miniaturised and grants it unprecedented mobility, making them especially well-suited for biomedical applications. In addition, to reduce the size further and enhance safety, these robots are typically fabricated with stimuli-responsive soft materials. The inherent mechanical compliance of soft materials enhances safety when deploying these robots inside the human body, while the stimuli-responsive nature of the material used allows the robots to be miniaturised even further – the robot's material can be directly used as either a sensor or actuator and as such, eliminate the need for certain on-board components. For these reasons, an off-board design approach is preferred and typically adopted in biomedical applications.

As might be expected, the key to the performance of off-board robots hinges greatly on how well the energy can be delivered from an external system to the robot. In biomedical applications, these sources of energy (i.e. magnetic, light and acoustic) are primarily selected on their ability to penetrate human tissues safely. Unlike light and acoustic energy sources, magnetic fields have better penetration, making it well-suited for biomedical applications. Optical methods require a direct, unhindered line-of-sight from the light source to the robot, and only have a maximum penetration depth of one or two centimetres under the human skin [3]–[5]. On the other hand, while acoustic methods do not have issues with the operating range, they perform poorly whenever there is a mismatch in acoustic impedance, as typically seen whenever there is an air-water interface or when a high-density material such as bone, is in the way of the acoustic waves. As such, in recent years, magnetic actuation has emerged as a promising stimulus to realise controllable, on-demand, non-invasive and targeted control of robots operating deep inside the human body. Advancements in this field have enabled these robots to navigate to a precise target position on land or in a fluid-filled confined environments. Furthermore, scenarios involving local cargo delivery (e.g., hydrogel structures, drugs, genes, imaging contrast agents, stem cells) have been demonstrated, highlighting the potential of these robots in biomedical contexts. Please refer to **Table 1.1** for a list of these robots reported in literature since 2018.

Table 1.1: Recent developments in untethered magnetic robots for biomedical applications.

Year	Authors	Key functionalities	Environment	Testing method	Proposed application	Reference
2018	Li et al.	3D cell culture on mircorobot	Fluid	In vivo (mice)	Targeted cell delivery	[6]
2018	Lu et. al	Legged soft millirobot	Air, fluid	N/A	Surface drug delivery	[7]
2018	Bozuyuk et al.	Magnetic chitosan microswimmer	Fluid	In vitro	On-demand surface drug delivery	[8]
2018	Hu et al.	Multimodal locomotion	Air, fluid	NA	Surface cargo delivery	[9]
2019	Jeon et al.	3D cell culture on mircorobot	Fluid	In vivo (mice)	Targeted cell delivery	[10]
2019	Yasa et al.	Cell transport and magnetic locomotion	Fluid	In vitro	Surface stem cell delivery	[11]
2019	Onaizah et al.	Magnetic scissors	Air	N/A	Tissue excision	[12]
2020	Dong et al.	Hydrogel, magnetic locomotion	Fluid	In vitro	Surface cargo delivery	[13]
2020	Alapan et al.	Magnetic microrollers locomotion in vessels	Fluid	In vitro	Surface drug delivery	[14]
2020	Lu et al.	Sensorised millirobot	Air	Ex vivo (Bovine stomach)	Temperature and pressure sensing	[15]
2020	Son et al.	Soft capsule endoscope	Air	Ex vivo (Porcine stomach)	Fine-needle biopsy	[16]

2020	Akolpoglu et al	Biohybrid microalgae	Fluid	In vitro	On-demand surface cargo delivery	[17]
2020	Fan et al.	Ferrofluid droplet robot	Air, fluid	N/A	Surface drug delivery	[18]
2021	Ceylan et al.	Patient blood–derived microrobots	Fluid	In vitro	Surface drug delivery	[19]
2021	Zhang et al.	Peristaltic pump, capsule, anchoring in tubular channels	Air, fluid	In vitro	Various – primarily surface cargo delivery	[20]
2021	Ren et al.	Selective locomotion modes for single design	Air, fluid	NA	Enhanced navigation of magnetic robots	[21]
2022	Hong et al.	Magnetic gearbox for multi-applications	Air, water, glycerol	NA	Sample collection/ tissue biopsy	[22]
2022	Wang et al.	Wireless stent robot and locomotion in vessels	Fluid	Ex vivo (porcine coronary artery)	Surface drug delivery	[23]
2022	Akolpoglu et al.	Biohybrid robot and on-demand drug release	Fluid	In vitro	Surface cargo delivery	[24]
2022	Zhang et al.	Magnetic locomotion, heating and power transfer	Air, fluid	Ex vivo (chicken)	Surface heating	[25]

2022	Tang et al.	Phase-change actuator	Air	NA	Angioplasty	[26]
2022	Sun et al.	Magnetic slime robot	Air	NA	Grasping	[27]
2022	Li et al.	Miniature coiled artificial muscle	Air	Ex vivo (porcine)	Magnetic scissors, clamp, driller	[28]
2022	Dogan et al.	Microrobots derived from macrophages	Fluid	In vitro	Cancer immunotherapy	[29]
2022	Lee et al.	Hydrogel microrobots	Fluid	In vitro	Surface drug delivery	[30]
2022	Sun et al.	Fluoroscopy-guided magnetic microswarm	Dry	Ex vivo (porcine biliary duct)	Biofilm eradication in medical implants	[31]
2023	Yan et al.	Dual tool compatible with stent robot	Fluid	Ex vivo (porcine coronary artery)	Detection of occlusion in lumens	[32]
2023	Wang et al.	Sensing through deformation tracking	Air	Ex vivo (porcine and mice)	Sensing of physiological properties	[33]

Despite these advances, the use of miniature magnetic robots in clinical applications is still severely limited because only one form of functionality, namely the shape-morphing ability of the robot for either locomotion or cargo delivery, is typically utilised. Moreover, even when cargo is delivered, it is predominantly limited to superficial tissue layers. As such, these untethered robots are only able to perform one out of the many interventional procedures, involving physical interactions with the tissues, routinely performed by doctors (e.g. venepuncture, suturing and injections etc.) [34]. In order to further push the deployment of these robots to the bedside, it is necessary to develop new medically-relevant functionalities without sacrificing on the mobility of these robots.

The challenges of developing such functionalities on magnetic millirobots are threefold.

Firstly, the size of the robot, which grants the robot part of its extraordinary navigation abilities also works against it – the size of the robot greatly limits the possibility of incorporating components to perform additional tasks. Miniaturising the existing technology found in traditional robots is one such approach but has its limitations. This is primarily because larger robots are typically controlled with an on-board approach whereas most untethered miniature robots are controlled with an off-board approach (i.e. magnetism, acoustic or light) [35], [36], where, as mentioned, some of the supporting infrastructure can be moved and placed outside the robot. As such, designs, technologies and techniques developed for an on-board approach might not be easily transferable.

Secondly, as the distance at which these robots have to operate away from the magnet increases (i.e. deeper inside the human body), it becomes increasingly harder to give additional control inputs to the robots with a magnetic field. As the distance from the actuating magnetic field increases and the size of the robot decreases, the entire robot sees the impinging magnetic field as a homogenous global field. Compounding this is the fact that magnetic fields are unlike light, which can be focused on a particular spot and hence, be used to selectively actuate parts of the robot. This reduced degree of control adds another layer of complexity when designing and trying to incorporate additional functionalities on the robots.

Finally, the use of any hard and rigid materials is typically avoided. Currently, there exists an assumption that such robots have to be fully soft for enhanced safety, or for continuum motion to be achieved. However, this imposes a key, and sometimes unnecessary, constraint on the design of these robots – rigid materials do exhibit certain desirable material properties, such as a high electrical conductivity or Young’s modulus, which are still orders of magnitude higher as compared to the best-performing soft materials with such properties. In such cases, incorporating hard and rigid materials could result in a significant increase in performance, while any disadvantages arising from the use of such materials might possibly be circumvented through smart design.

In view of these challenges, this thesis aims to further extend and explore potential applications of magnetically controlled untethered miniature robots in biomedical scenarios. Specifically, we aim to achieve this by developing new methods to enable new forms of physical interactions between the robot and tissue, which have:

1) not been demonstrated in any magnetically controlled untethered miniature robots to date, in order to accomplish certain medically relevant tasks.
2) been demonstrated in literature to date but suffer from practical issues, such as a short working distance.

The state-of-the-art will be summarised in the relevant sections.

1.2 Contributions of this thesis dissertation

This dissertation aims to overcome the lack of diversity in functionalities by proposing several mechanisms which can be readily adopted on existing untethered miniature magnetic robots, actively triggered on demand and independently controlled, to enable advanced physical interactions between the robot and the tissues. Such capabilities pave the way for the development of next-generation magnetic miniature soft robots capable of addressing real-world clinical problems.

To achieve this, a two-pronged strategy is adopted. Firstly, the “fully soft” assumption to the design of untethered miniature robots is challenged. Specifically, we aim to demonstrate, for the first time, a synergistic approach to the design of untethered miniature robots which incorporates the strengths of both soft and hard robotics. Through it, we show how the performance of untethered miniature robots can be significantly enhanced without compromising on their existing capabilities (i.e. locomotion). Secondly, high-frequency magnetic fields are utilised, to expand the number of control, and hence design parameters. Although the profile and magnitude of magnetic fields have been extensively exploited as a control parameter for shape deformation, the effects of changing the frequency of the magnetic fields have been less explored. At such frequencies, specifically in the kHz regime, magnetic fields still remain safe for human exposure whilst being too high for actuation, thereby avoiding any interference with the robot’s locomotion. As such, by relaxing these constraints, coupled with novel mechanical designs and implementation, advanced functionalities can be achieved to further enhance the capabilities of these robots.

Three new functionalities for these robots were developed based on this strategy. A summary of the new functionalities developed and how the chapters are linked is provided in **Figure 1.1**.

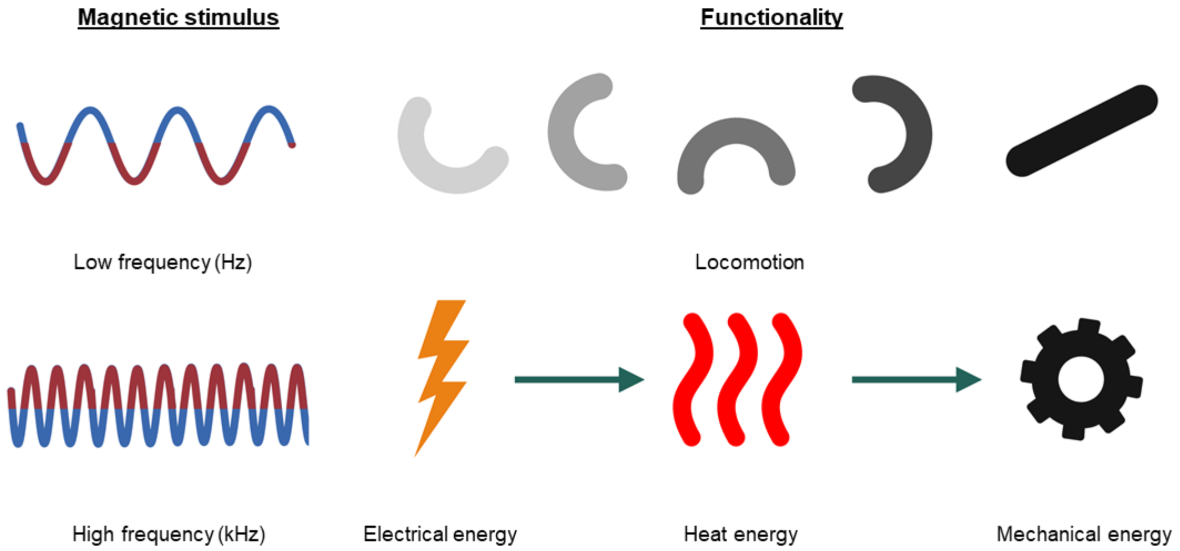

Figure 1.1: Overview of functionalities developed in this work. Application of a low-frequency magnetic field allows for locomotion of the robot, while application of a high-frequency magnetic field enables new functionalities beyond locomotion. The relationship between the functionalities developed in each chapter are demonstrated with the arrows. In Chapter 2, the induced electrical energy was used to heat up a trigger to release mechanical energy pre-stored in a spring. In Chapter 3, the heat generated by the induced electrical energy was optimised and directly utilised. In Chapter 4, the induced electrical energy was directly harvested and utilised.

1.3 Thesis outline

In Chapter 2, we propose a wireless spring-preloaded barbed needle release mechanism, which can provide up to 1.6 N of force to drive a barbed needle into soft tissues to allow robust on-demand anchoring on three-dimensional (3D) surfaces. The mechanism is wirelessly triggered using radiofrequency (RF) remote heating and can be easily integrated into existing untethered soft robotic platforms without sacrificing their mobility. Design guidelines aimed at maximising anchoring over the range of the most biological tissues (kPa range) and extending the operating depth of the device inside the body (up to 75%) are also presented. Enabled by these advances, we achieve robust anchoring on a variety of ex vivo tissues and demonstrate the usage of such a device when integrated with existing soft robotic platforms and medical imaging. Moreover, by simply changing the needle, we demonstrate additional functionalities such as controlled detachment and sub-surface drug delivery into 3D cancer spheroids.

In Chapter 3, we propose a pangolin-inspired bi-layered soft robot design which gives these robots the ability to locally generate heat. Such a design is necessary because the soft body limits the integration of non-magnetic external stimuli sources on the robot, thereby restricting the functionalities of such robots. One such functionality is localised heat generation, which requires solid metallic materials for increased efficiency. Yet, using these materials compromises the compliance and safety of using soft robots. The proposed pangolin-inspired bi-layered soft robot design allows us to simultaneously overcome these competing requirements. We show that the reported design achieves heating > 70 °C at large distances > 5 cm within a short period of time $<$ 30 s, allowing users to realise on-demand localised heating in tandem with shape-morphing capabilities. We demonstrate advanced robotic functionalities, such as selective cargo release, in situ demagnetisation, hyperthermia and mitigation of bleeding, on tissue phantoms and ex vivo tissues.

In Chapter 4, we introduced a design to allow these robots to wirelessly harvest electricity from the RF field. Electricity is one of the most widely used and versatile form of energy. Notwithstanding, few untethered magnetic miniature soft robots possess such a capability because the soft body and size limits the possibility of having on-board power supply. Inductive power transfer is an attractive method to transfer large amounts of power safely and wirelessly. However, solid materials with high electrical conductivities are required for increased efficiencies, yet they are avoided as solid materials decrease the deformability of these robots. To address this, we first optimised the geometry of a single metallic loop for non-resonant power transfer and shape-morphing. Next, we introduce a bi-layered scalable robot design which allows the robot to generate electricity without compromising on its deformability. Despite a small footprint $< 2\ \text{cm}^2$, the robot is able to harvest power > 250 mW at large distances > 5 cm. Enabled by these advances, a camera was powered with a communications module. This allowed us to capture and transmit an image wirelessly to a receiver 10 cm away via Bluetooth.

In Chapter 5, we summarise key results of this thesis and suggest future research directions towards the development of next-generation of untethered robots capable of addressing real-world clinical problems and beyond.

Chapter 2: On-demand anchoring of wireless soft miniature robots on soft surfaces

2.1 Background

Wireless miniature mobile robots capable of navigating inside hard-to-reach sites of our body have great potential in minimally invasive medical applications [1], [37], [38]. In particular, magnetically actuated wireless miniature soft robots are highly promising, as external magnetic fields are wireless, dexterous, precise and can safely penetrate deep inside the human body [36], [39], [40]. However, the requirement of a long-lasting magnetic field input could severely limit the use of miniature magnetic medical robots in certain clinical applications, especially those requiring extended operation durations inside the body. Since once the magnetic field input is removed, the robots would lose all actuation capabilities and they would easily move away from their target position due to the dynamic motion of the body tissues and fluids and other disturbances.

Although recent advances in the development of milli- and microscale functional materials, manufacturing and assembly techniques [20], [40]–[42] have enabled integrated anchoring mechanisms for wireless medical devices, they are mostly limited to confined tubular structures [20]. Moreover, existing strategies for surface attachment that exploit mechanical interlocking [43]–[45], van der Waals force [46], [47], capillary force [48], suction force [49], or a combination of these forces [50], [51] do not perform well on biological tissues for various reasons. First, internal tissue surfaces are highly wet, textured, rough and covered with various biological complex fluids, such as a constantly regenerating mucus layer [52], [53]. These properties reduce the surface contact area and hence the maximum adhesion. Even if strong adhesion is achieved in special conditions, it would be only temporary, since the mucus layer is gradually replaced over time [54]. Second, although some of these methods can attach well to biological surfaces, they require a high preload and have limited attachment testing on dynamic loads [55], [56]. Such a requirement makes them incompatible with miniature soft robots with limited force outputs (next section). With these issues, for reliable one-time long-term anchoring, the mechanism should directly engage with the underlying tissue layer (**Table 2.1**). Chemical methods are ruled out because there are more issues to consider as compared to physical attachment methods [57]. For instance, mucoadhesion, a common chemical method of attachment, is heavily dependent on both internal (e.g., pH, concentration of drugs loaded, hydrophilicity and molecular weight) and external factors (e.g., specific formulations have to be designed for each surface, swelling because of working environment) [58]–[60]. These factors are hard to predict and monitor in real applications, and variance in any of these factors may prevent robust anchoring.

Table 2.1: Comparison of the forces required for tissue penetration across literature. Note that these values were obtained indirectly (i.e. based on the forces provided by the respective devices) and may not necessarily reflect the actual forces required for tissue penetration.

Mechanism	**Needle specifications**	**Maximum penetration depth (mm)**	**Penetration force (N)**	**Tissue type**	**Reference**
Spring-loaded	Single needle – cone angle 19.4°	15	~ 1	Stomach (porcine)	[61]
Spring-loaded	96 conical microneedles – cone angle 11.3°	1	~ 0.1	Small intestine (porcine)	[62]
MRI-powered Gauss gun	18, 20, 26 G needles	15	~ 1	Agarose gel	[63]
Magnetic gradient	24 G needle	10	0.4-0.6	Stomach (porcine)	[16]
Magnetic hammer	Single needle – cone angle 11.3°	NA	Pulsing force ~ 0.01	Brain (goat)	[64]
This work	Barbed single needle – cone angle 10°	1	~ 1	Bladder (porcine)	[65]

2.1.1 Theoretical force provided by a magnetic soft robot

With an experimentally tested remanence of 85 emu g^{-1} and assuming a robot with the following dimensions: 3 mm × 1 mm × 0.2 mm,

$$V_{robot} = 3 \times 1 \times 0.2 \times 10^{-9}$$

$$= 0.6 \times 10^{-9}\ \mathrm{m}^3.$$

$$V_{Ecoflex} + V_{NdFeB} = 0.6 \times 10^{-9}\ \mathrm{m}^3.$$

$$\left(\frac{m}{\rho}\right)_{Ecoflex} + \left(\frac{m}{\rho}\right)_{NdFeB} = 0.6 \times 10^{-9}\ \mathrm{m}^3\ ,$$

where m is the mass of the material, V is the volume of the material and ρ is the density of the material.

Assuming 1:3 mass ratio of Ecoflex to NdFeB,

$$m_{NdFeB}\left[\left(\frac{1}{3\rho}\right)_{Ecoflex} + \left(\frac{1}{\rho}\right)_{NdFeB}\right] = 0.6 \times 10^{-9}\ \mathrm{kg}.$$

Since $\rho_{Ecoflex} = 1070\ \mathrm{kg\ m}^{-3}; \rho_{NdFeB} = 7610\ \mathrm{kg\ m}^{-3}$,

$$m_{NdFeB} = 1.3546 \times 10^{-6}\ \mathrm{kg}.$$

$$Magnetic\ moment\ m_{mag} = 85(1.3546 \times 10^{-6}) \times 10^3$$

$$= 1.1514 \times 10^{-1}\ \mathrm{emu}$$

$$= 1.1514 \times 10^{-4}\ \mathrm{A\ m}^2.$$

Assuming an external field of 50 mT applied perpendicularly to magnetisation profile of robot (uni-direction),

$$\tau = 50 \times 10^{-3} \times 1.1514 \times 10^{-4} \times \sin 90\ \mathrm{N\ m}$$

$$= 5.757 \times 10^{-6}\ \mathrm{N\ m},$$

where τ is the torque.

Assuming a rigid body,

$$\tau = F \times d.$$

$$F_{max} = \frac{\tau}{d} = \frac{5.757 \times 10^{-6}}{3 \times 10^{-3}} = 1.919 \times 10^{-3} = 2\ \text{mN},$$

where F_{max} is the maximum force exerted by the material and d is the moment arm. d is taken to be the length of the robot (i.e. 3 mm).

2.2 Proposed approach

Here, we propose a mechanism that can be precisely controlled by an external RF-field to achieve on-demand needle release (**Figure 2.1A**). Up to 1.6 N of force can be provided to drive a barbed needle into soft tissues to allow robust on-demand anchoring on 3D surfaces. The small size of the proposed mechanism (2.7 mm diameter and 3.2 mm compressed length) allows it to not only access hard-to-reach regions inside the human body but also allows it to be readily integrated on soft millirobots (**Figure 2.1B**). This allows the soft millirobots to retain the soft-bodied locomotion strategies previously developed for precise positioning and orientation. Design strategies to optimise the performance of the anchoring and triggering mechanism based on simulations are also presented. We demonstrate potential applications of the anchoring mechanism on a variety of ex-vivo tissues. Control over the duration of anchoring and sub-surface drug delivery are demonstrated with biodegradable and hollow needles, respectively, to showcase the versatility of the proposed mechanism.

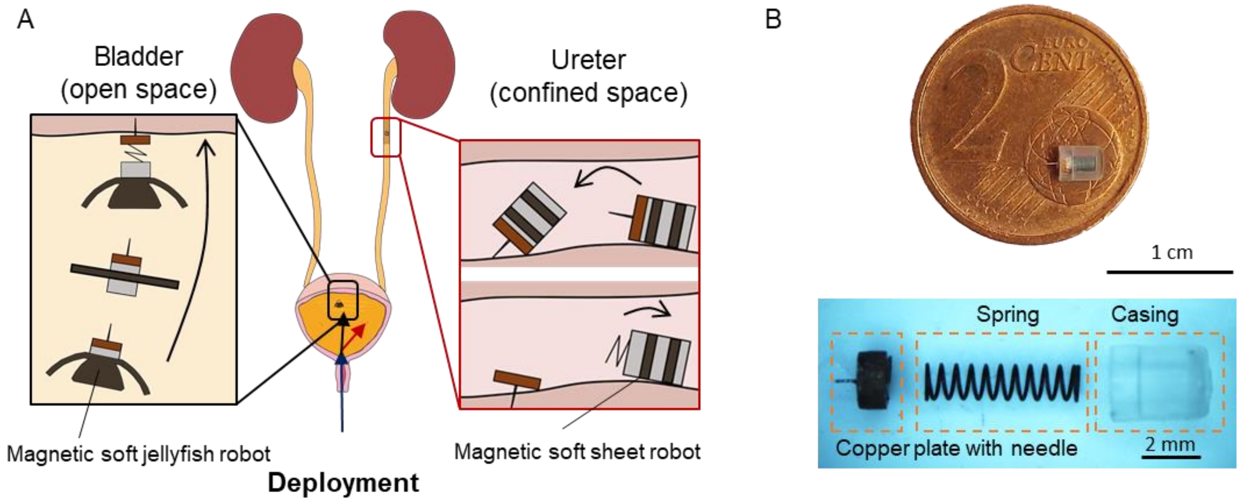

Figure 2.1: Proposed RF-triggered spring-loaded surface-anchoring mechanism. (A) Conceptual illustration of the anchoring mechanism integrated with existing soft magnetic robots to achieve anchoring in open and enclosed environments. (B) Fabricated prototype.

2.3 Design and fabrication

Springs (CBM010B04E, CBM014A09E, CBM014B07E, CBM014B02E and CBM014B05E, Lee Spring) and needles (S-J1015, Seirin) were used as purchased. The 2 mm-diameter copper rings for the heating element were laser cut from a 1 mm-thick copper plate. A 0.11 mm opening was also made with the laser at the centre of the ring to mount the needles. The needles were then marked at a distance of 1 mm away from the needle tip with a marker. Next, the needles were threaded through the copper plate. Once the 1 mm mark appeared on the other side of the copper plate, cyanoacrylate glue (401, Loctite) was applied to fix it in position on both sides of the copper plate. After the glue had set, the needle was snipped off with a pair of wire cutters. As it was impossible to flush the cutting edge of the wire cutters to the surface of the copper plate, a small length of the needle remained on the copper plate after snipping. The extra needle was folded inward and cyanoacrylate glue was used to secure it to the surface of the copper plate (**Figure 2.2**).

If required, barbs were added at this stage. The barbs were fabricated using two-photon polymerisation with a negative-tone photoresist (IP-S, Nanoscribe GmbH). They were positioned such that they were 0.2 mm away from the needle tip. All procedures involving any measurements were performed by hand under a stereomicroscope using a stage micrometer as a guide (R1L3S1P, Thorlabs). The casing and a holding jig were printed with Clear Resin on a stereolithography (SLA) printer (Form 3, Formlabs). Next, cyanoacrylate glue (431, Loctite) was applied to the side of the copper plate. After curing on a hot plate at 40 °C for 2 min, the copper plate with the needle

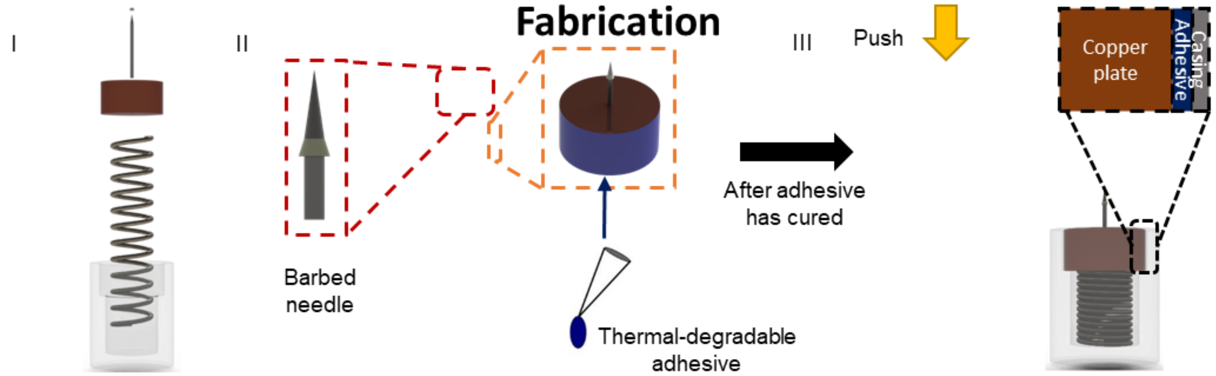

Figure 2.2: Fabrication procedure. (I) The components (barb, needle, copper plate, spring and casing) are brought together. (II) Cyanoacrylate adhesive is applied to the sides of the copper plate and the barb is mounted on the needle and secured with adhesive. (III) The copper plate is then pushed into the casing after the adhesive has cured to create an interference fit.

was assembled with the casing and spring. One end of the spring was secured to the casing with cyanoacrylate glue. On the other end of the spring, the copper plate was first placed on top with the needle pointing outward and then pushed into the structure.

The soft millirobots were fabricated with a previously reported method [66]. Briefly, Scotch Tape (840, 3M) was first placed along the sides of an acrylic sheet. The number of layers placed determined the thickness of the robot. Neodymium-iron-boron (NdFeB) magnetic microparticles (MQP-15–7, Magnequench) were mixed with platinum-catalysed silicone (Ecoflex 00-10, Smooth-On Inc.) in a 1:1 mass ratio, degassed for 5 min, poured on the acrylic sheet and evened out with a razor blade. The sample was then left to cure on a hot plate at 65 °C for 1 h. After the sample had cured, it was laser cut (ProtoLaser U3, LPKF Laser & Electronics AG) to the desired dimensions. The structures were then detached from the substrate with tweezers and wrapped around a non-magnetic sphere (diameter of 5 mm) or rod (diameter of 3.2 mm) for the jellyfish and sheet robot, respectively. The robots were then magnetised with a 1.8 T homogeneous magnetic field in a vibrating sample magnetometer (EZ7, Microsense) for 5 s. Water-soluble glue (822095, Pritt) was applied during this process to ensure that the robots tightly conformed to the magnetisation structures. The non-magnetic sphere and rod were printed on a SLA printer with Clear Resin. Next, the robots were detached from the structures and rinsed with deionised (DI) water until no more glue was observed on the surface. The pre-assembled firing mechanisms were then attached to the robots with cyanoacrylate glue. Whenever necessary, a stereomicroscope (ZEISS Stemi 508, Carl Zeiss Microscopy GmbH) was used to guide the process.

2.4 Working principle

The proposed mechanism is a spring-loaded mechanism encapsulated in a casing and is composed of four components: a barbed needle mounted on a copper plate for insertion and anchoring, a pre-loaded spring to provide the required force output, a casing to enclose the structure and a thermal-degradable adhesive which holds the copper plate in the casing and acts as a trigger. As we intended to integrate the mechanism with magnetic soft millirobots, copper was selected as the heating element because it was non-magnetic and would not interfere with magnetic actuation of the robots. Stainless steel needles with a shaft diameter of 100 µm were used and barbs were added to enhance the anchoring force. An additional advantage of using springs was the rapid release of energy along the axis of compression, which could accelerate the needle to very high velocities during release. Based on high-speed videos, this velocity is estimated to be at least 50 mm s^{-1}. As it has been previously reported that the penetration force in ex-vivo porcine heart tissues is inversely proportional to the impact velocity [67], a needle with a speed of 50 mm s^{-1} requires approximately 50% less puncture force than one travelling at 5 mm s^{-1}. This would further reduce the amount of puncture force required by the robot for tissue penetration.

The inner diameter of the casing encapsulating the spring was designed to be 0.1 mm larger than the diameter of the copper plate. For the copper plate and casing used in this work, the diameters were 2.0 mm and 2.1 mm, respectively. Due to this difference in size, the copper plate would initially be unable to stop the motion of the spring. However, by applying a thin layer of cyanoacrylate adhesive to the sides of the copper plate, the diameter of the copper plate was increased such that it was slightly larger than the diameter of the casing. After the glue had completely cured, the plate was then press fitted on the casing, encapsulating the spring within the casing.

To trigger the mechanism (**Figure 2.3A**), an external 338 kHz RF field was applied. From Faraday's and Lenz's law, the RF field induced an eddy current inside the copper plate such that it produced a magnetic field which opposed the direction of the applied field [68]. The eddy current heated the copper plate via Joule heating and heated up the surrounding layer of cured adhesive via thermal conduction. When the temperature reached 60 °C, the strength of the cured adhesive was reduced by 40% compared to the strength at room temperature and the adhesive layer was no longer able to hold back the compressed spring [69]. At this point, the spring was free to extend and pushed the copper plate together with the needle towards the surface (**Figure 2.3B**). We verified the temperature-triggered mechanism by taking infrared images of the triggering process (**Figure 2.3C**).

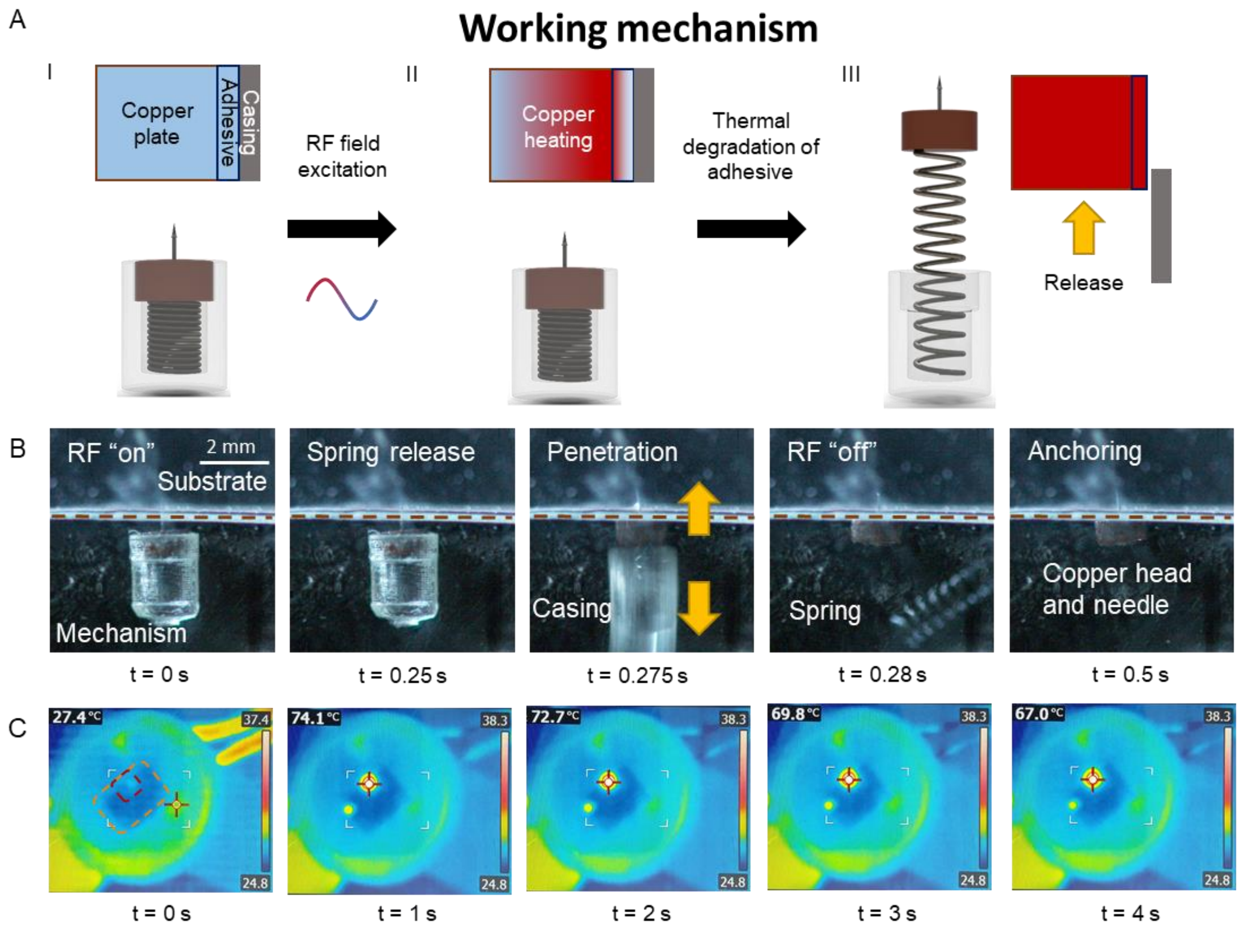

Figure 2.3: Working principle of the proposed mechanism. (A) Actuation sequence of the mechanism. Insets illustrate the temperature changes inside the copper plate as the mechanism is triggered. Red and blue represent higher and lower temperatures, respectively. (B) High-speed video image snapshots of the firing process in air. Brown line indicates the boundary between the substrate and the mechanism. The images are blurred primarily because some parts are moving out of plane and the firing process takes place too quickly for the focus to be adjusted automatically or manually. Arrows indicate the direction of movement of the various parts as the mechanism is fired. (C) Infrared camera images of the firing process in air. In the first infrared image, the area bordered in orange indicates the boundaries of the substrate and the area bordered in red indicates the approximate location of the mechanism. Cross from t = 1 s to t = 4 s indicates the location of the hottest region, which corresponds to where the copper plate is located.

2.5 Device characterisation

2.5.1 Anchoring on artificial biological substrates

The performance of the anchoring mechanism was assessed based on two parameters: success rate and pull-out force. A successful event was defined as the case where the needle remained attached to the surface after remote triggering. The pull-out force was the peak force recorded as the needle was removed from the surface. The prototypes were submerged in DI water and were not fixed to the substrate in all the experiments (**Figure 2.4**). To find the optimum design of the anchoring mechanism, we categorised the performance based on two design groups: barb design and spring selection. In the former, the effects of adding a barb on the performance on different surfaces were evaluated. In the latter, since the spring was one of the critical components of the mechanism, the effect of using different springs was examined. Polydimethylsiloxane (PDMS; Sylgard 184, Dow Corning) at base to curing agent mass ratios of 10:1, 20:1 and 30:1 were selected as the soft surfaces for the characterisation tests because the Young's modulus of these surfaces fell within the range of the most biological tissues [70] and the Young's modulus was the dominant mechanical property during the pre-puncture stage [71].

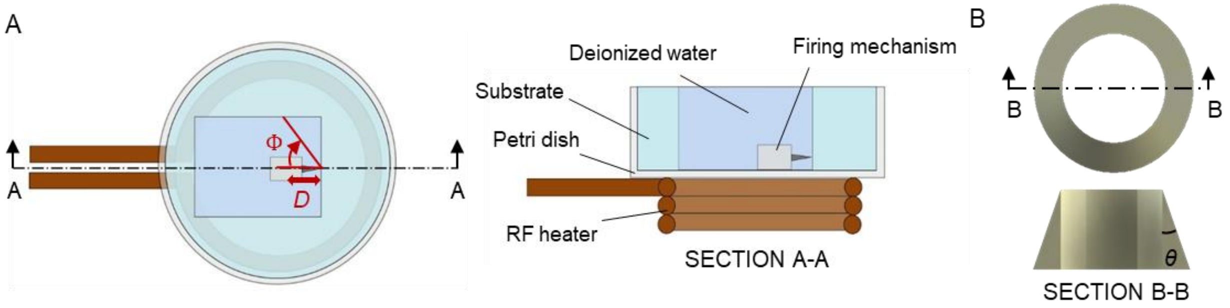

Figure 2.4: Anchoring mechanism characterisation. (A) Schematic of experimental setup. (B) Schematic of the barb design.

After 5 grams of PDMS of appropriate mass ratios were prepared, they were poured into a 55 mm-diameter Petri dish and left in an oven to cure at 90 °C for 2 h. An area measuring 3 cm × 3 cm was then removed from the centre and filled with DI water. Next, the firing mechanism was submerged and placed at the appropriate location. The entire Petri dish was then placed at a distance of 3 mm above the RF heater probe, with the firing mechanism visually positioned to be at the centre of the probe. The RF heater was set at 751.8 A at a frequency of 338 kHz. All of the characterisation tests were recorded with a high-speed camera (Miro M310, Phantom) at 2600 frames per second (fps). The penetration depth was determined by post-analysis of the high-speed videos on ImageJ. The length of the needle not inside the surface was subtracted from the initial length of the needle (1 mm in this work) to reduce problems associated with refraction. To measure the pull-out force, a pair of tweezers was clamped to the end of an Instron machine (5942, Instron) with the 5 N load cell while the surface was stuck to the other. Tweezers were used to reduce the contact area to make gripping of the copper plate possible. The pull-out force was defined as the highest force recorded.

First, we investigated how the geometry of the needle barb could affect the anchoring performance. Due to the asymmetry of the barbs in the axial direction, the needle was also able to utilise mechanical locking with the surface, in addition to the friction between the embedded needle and the surface, for anchoring. A barbed needle resulted in a lower penetration depth, since more energy was required to drive the needle into the surface to the same depth as a barbless needle (**Figure 2.5A**). This decreased the length of the needle embedded in the substrate after anchoring and hence, the frictional force. However, this reduction in anchoring force was less dominant than the increase brought by the mechanical locking between the barbs and the surface. This is reflected in the form of an increased pull-out force (up to 38%) and success rate (**Figure 2.5B**).

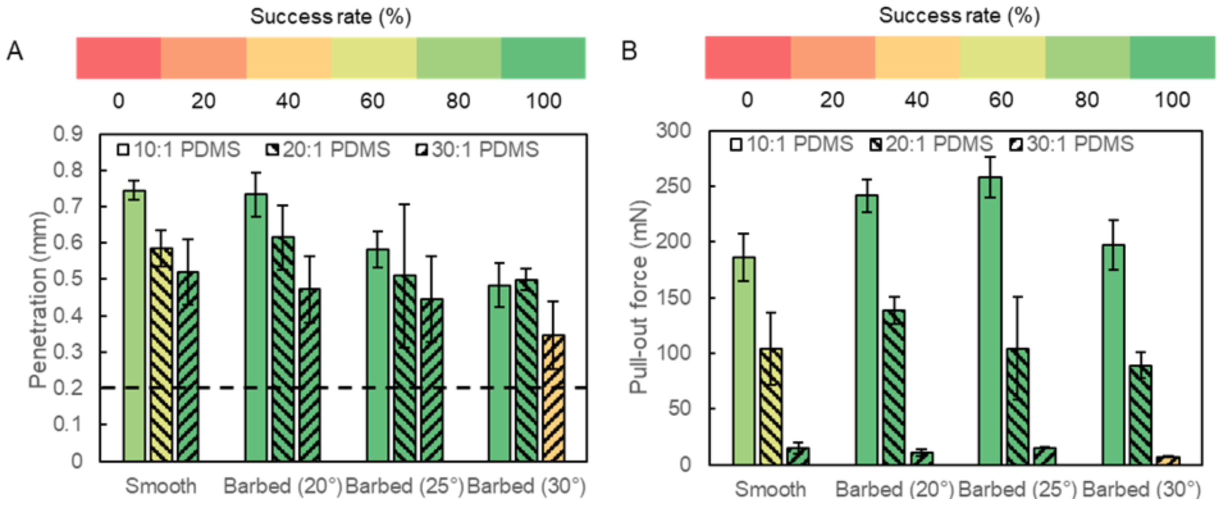

Figure 2.5: Characterisation of anchoring on artificial biological substrates. (A) Penetration depth with respect to the different substrates used in this work (n = 5). Dotted line denotes the position of the barb. Error bars represent the standard deviation. (B) Pull-out force of different barb designs with respect to the different substrates (n = 5). Error bars represent the standard deviation.

Furthermore, as the stiffness of the surface decreased, it was observed that the cone angle at which the maximum pull-out force was recorded also decreased. At a given cone angle for the barbs, a surface with a lower stiffness would be able to deflect more, requiring the needle to travel deeper into the surface before the stress induced at the needle tip exceeded the critical stress required for puncture. Note that the critical stress required for puncture were similar throughout all the substrate samples because of their similar fracture toughness (**Figure 2.6**). The increased deformation of a softer surface explains why a shorter length of the needle was left embedded in the surface. This shorter penetration length resulted in a lower pull-out force as the stiffness of the surface decreased. Hence, a smaller cone angle should be used on a surface that is less stiff in order to achieve the largest possible pull-out force.

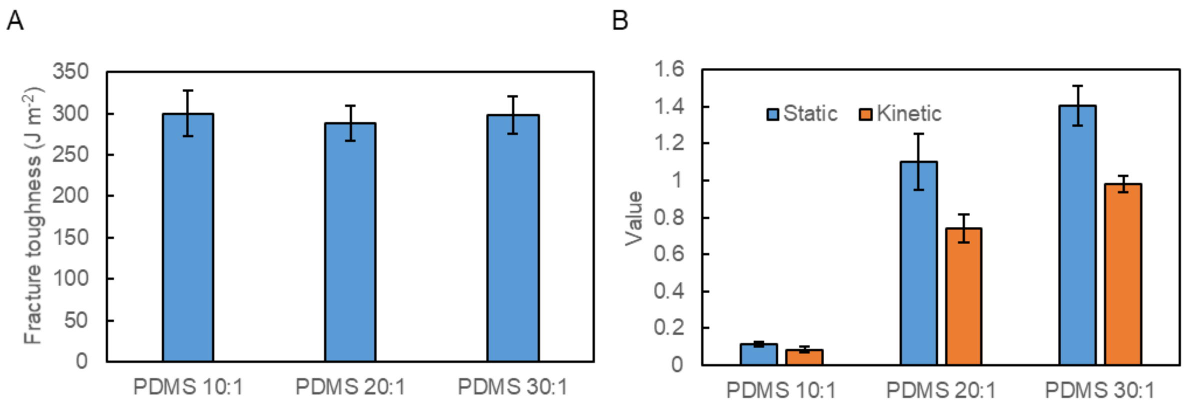

Figure 2.6: Material properties of tested substrates. (A) Fracture toughness (n = 3). Error bars represent the standard deviation. (B) Coefficient of static and kinetic friction (n = 3). Error bars represent the standard deviation.

Next, to investigate the effect of changing the spring parameters on the performance, we conducted two sets of experiments on a 20:1 PDMS surface using a barb with a cone angle of 20°. Springs, which were suitably small (< 5 mm in both diameter and compressed length) but could still provide almost 1 N of force, were used in these tests, to facilitate integration with miniature magnetic soft robots. We first selected a set of springs by varying the maximum amount of the force while keeping the extension length constant (**Figure 2.7A**). Next, we changed the maximum extension length of the springs (**Figure 2.7B**) while keeping the maximum force constant. Both results indicated that there was an optimal value in which the largest pull-out force could be achieved. By combining and re-expressing the figures with respect to the spring constants, we could see that the spring with a medium spring constant 0.226 N mm^{-1} out of the five tested springs (with spring constants ranging from 0.087 to 0.383 N mm^{-1}) gave the highest anchoring success rate and the largest pull-out force (**Figure 2.7C, D**).

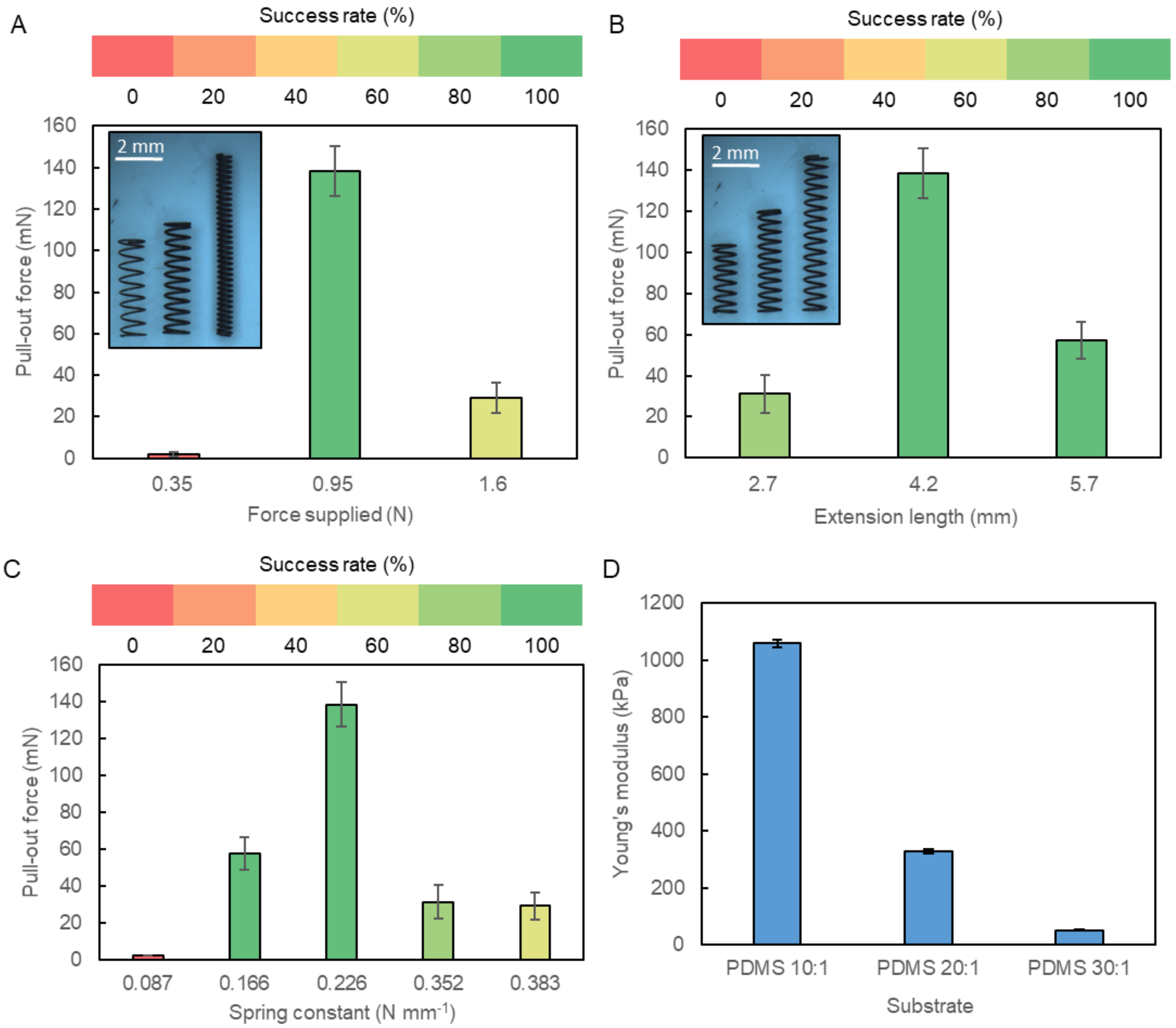

Figure 2.7: Characterisation of anchoring on artificial substrates. (A) Pull-out force with respect to the force supplied by the spring (n = 5). Error bars represent the standard deviation. (B) Pull-out force with respect to the extension length of the spring (n = 5). Error bars represent the standard deviation. (C) Measured pull-out forces against spring constants (n = 5). Error bars represent the standard deviation. (D) Young's modulus of tested substrates (n = 3). Error bars represent the standard deviation.

In addition, a mathematical model of the anchoring mechanism was built to guide future designs. Based on high-speed images of the trigger event (**Figure 2.8A**), the puncturing process was divided into six phases: initial, deflection, puncture, needle insertion, recoil and final phase (**Figure 2.8B**). We modelled the mechanism as a spring-mass system, with the soft surface and spring being modelled as serially connected springs (**Figure 2.8C**). As the time taken for anchoring is less than a second (**Figure 2.3B**), the response of the surface is dominantly elastic and can be characterised by a linear stress-strain response (i.e., spring) [72]. In the initial phase (phase I), the mechanism is oriented towards the surface and there are no net forces acting on the soft surface or the needle. We set the origin to be at the soft surface and define x_1 as the maximum surface deflection. x_1 need not always be at the needle tip as seen in the illustrations of the later stages (phases IV and V). In the deflection phase (phase II), the mechanism is triggered and the spring drives the needle into the surface by x_1. There is no cutting or penetration of the surface in this phase. When x_1 reaches a value such that the corresponding stress intensity factor that accompanies the stress field induced at the needle tip exceeds the fracture toughness of the surface, the needle penetrates the surface (phase III). The x displacement at this point is recorded as x_p. Frictional force will start to act from this phase onwards. Since friction acts along the length of the needle, we assume that the pressure acting along the length of the needle is constant and is proportional to the depth of insertion $x_1 - x_p$. This process continues until the copper plate driving the needle impacts the surface or until the needle stops if the needle is sufficiently long. At this point (phase IV), deflection of the surface is maximum and the velocity of m_1, which corresponds to the mass of the copper plate, is zero. After this point, the spring loses contact with m_1 and the surface starts releasing the stored elastic energy. This accelerates m_1 in the opposite direction (phase V) until all the energy is released (phase VI). In all phases, since the casing is not fixed and is free to move, it accelerates in the opposite direction.

By examining the equations of motion of each phase (**Eq. 2.1**–**2.4**), a system of ordinary differential equations describing the motion of the head and the casing during the process was obtained. Equations corresponding to the deflection phase (**Eq. 2.1**) were then numerically solved in MATLAB using the ode45 solver. The stiffness of the soft surfaces were computed from the experimentally determined Young's modulus based on a previously proposed method [73]. These surfaces were selected to cover the stiffness of living tissues in the kPa range, which encompasses most organs inside the human body [70]. For the spring constants, we directly used the values provided by the manufacturer for the springs. To increase the accuracy of the model, parameters used in the simulations were experimentally determined. All other simulation parameters are provided in **Table 2.2**. In the simulations, we only considered the case where a barbless needle, placed right next to the surface, enters it at 90°. When the angle of insertion or distance from the surface changes, this results in a reduction in the force supplied to deform the substrate. Similarly, the effect of the barb can be reflected in this model by introducing a penalty term. Specifically, addition of a barb will increase the apparent bevel angle of the needle and reduce the force applied [73]. As these affect all configurations equally and are not specific to a particular configuration, the same trends will hold and we do not consider their effects in the model.

Table 2.2: Parameters for MATLAB simulations.

Parameter	**Value (unit)**
m_1	20 mg
m_2	30 mg
L_{sp}	6 mm
x_1 at t=0	0 mm
$\dot{x}_1$ at t=0	0 m s^{-1}
x_2 at t=0	-1.8 mm
$\dot{x}_2$ at t=0	0 m s^{-1}
$\mu_k\ - casing\ on\ glass$	0.1609
C_d	1.15
ρ_{water}	1000 kg m^{-3}

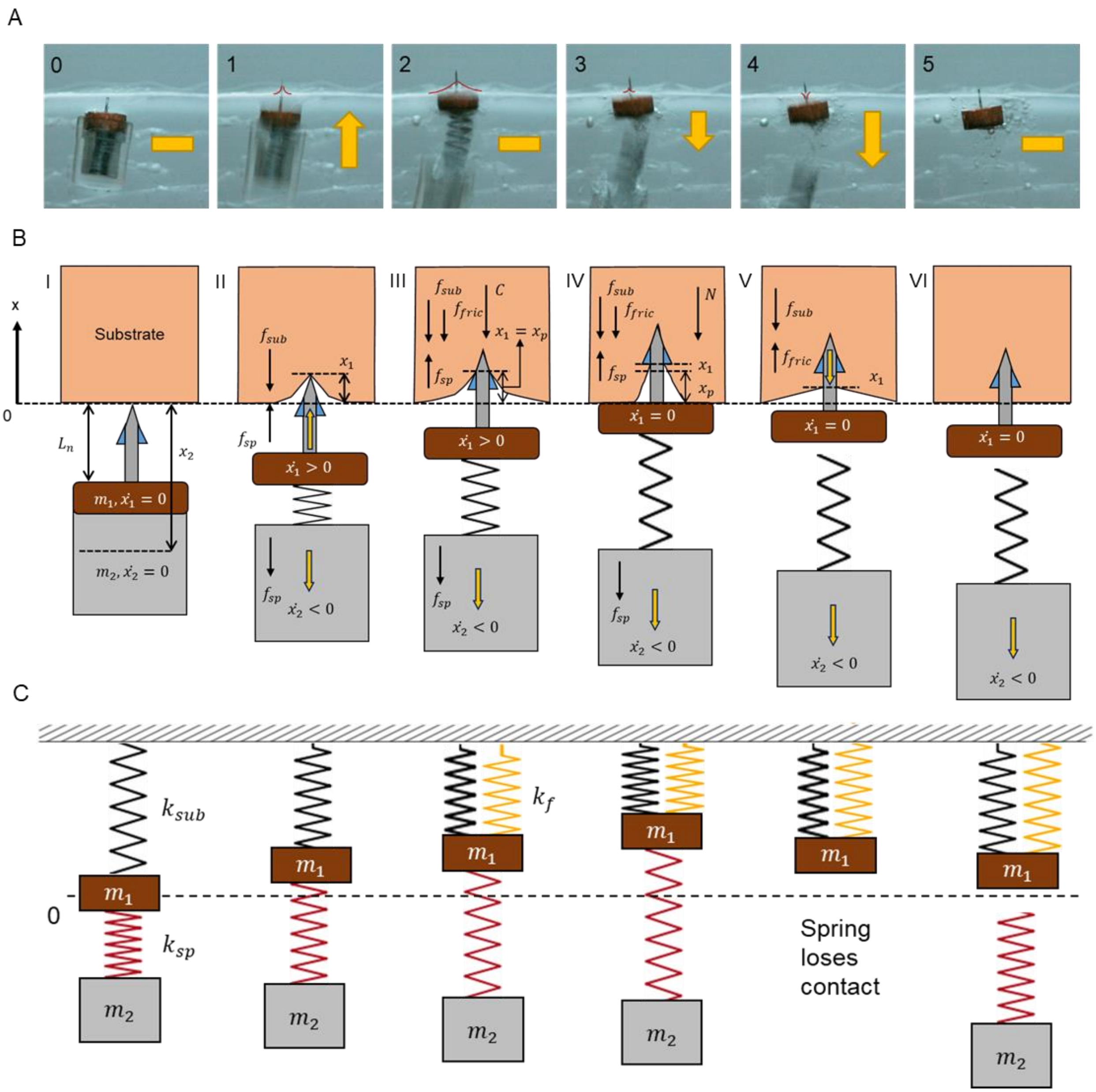

Figure 2.8: System-based model of the anchoring mechanism for optimisation. (A) Actuation sequence of the mechanism into 30:1 PDMS. Yellow arrow indicates direction of motion. Red markings indicate deflection of the substrate. (B) Illustration depicting the six stages of the tissue penetration. (I) Positioning of the mechanism. (II) Initial substrate deflection. (III) Tissue puncture. Friction starts acting from this stage. (IV) Maximum penetration into substrate. Spring loses contact with the head after this stage. (V) Elastic energy release of substrate. (VI) Anchoring of copper plate to substrate. Yellow arrows depict direction of motion. Black arrows indicate the forces acting on the respective bodies. (C) Equivalent spring mass system of the process.

From the analysis, we observed that the velocity of the needle after travelling 1 mm distance into the tissue was almost independent of the Young's modulus of the surface and was largely dependent on the spring constant (**Figure 2.9A**). Given that the puncturing force would be the same, since the fracture toughness of the surfaces was similar and the needle length was sufficiently short (1 mm) such that the difference in kinetic friction did not have an appreciable effect on the speed, it can be inferred that the copper plate mounted on a spring with a larger spring constant would have a larger impact and higher exit velocity. As a result, the needle would move back out of the substrate after penetration. This explains why an optimal value for the spring constant for a particular substrate exists (**Figure 2.7C**). The spring must be able to provide enough force to drive the entire length of the needle into the substrate and yet, dissipate enough energy during the process so that the remaining energy would be smaller than the energy required to pull out the needle.

Although the spring constant is highly dependent on the fracture toughness of the surface, a spring with a larger spring constant should be used as the fracture toughness of the surface increases or if a longer needle is used, since more energy will be used to overcome friction during the insertion phase. Should the exact fracture toughness be unknown, as in the case of most biological samples, we recommend that a more conservative value (i.e., spring with a lower spring constant) first be used. From the results presented in **Figure 2.7C**, we observed that using springs with overly high constants (0.352, 0.383 N m^{-1}) resulted in lower success rates and pull-out forces in comparison to springs with more conservative spring constants (0.166, 0.226 N m^{-1}).

Two other conclusions can be made about the system from the analysis. First, although distributing more mass to the casing is favourable in achieving higher penetration, this ratio cannot be increased infinitely and must be balanced against the RF heating efficiencies. We observed that the copper plate and needle with a combined mass of m_1, would be able to move deeper into the surface as more mass was distributed to the casing, m_2, which increased the likelihood of penetration and anchoring. Moreover, as the mass ratio $\frac{m_1}{m_2}$ decreased, the velocity of m_1 also increased (**Figure 2.9B**). However, as the mass ratio drops, the thickness of the copper plate will decrease given a fixed diameter. Correspondingly, this will reduce the heating efficiency and hence the triggering performance of the mechanism. As an example, when the mass ratio is 0.1, the thickness of the copper plate will become 70 µm given the current geometry. This is lower than the skin depth of the copper, which is calculated to be 117 µm at 338 kHz [74]. At thicknesses below the skin depth, RF heating efficiency will be compromised and the required temperatures might not be achievable or might require extended heating durations. Please refer to the next section for an analysis on RF heating of the system. Therefore, a mass ratio of 1 was used in this work, as it was the lowest mass ratio that could be used without compromising the heating efficiency of the mechanism.

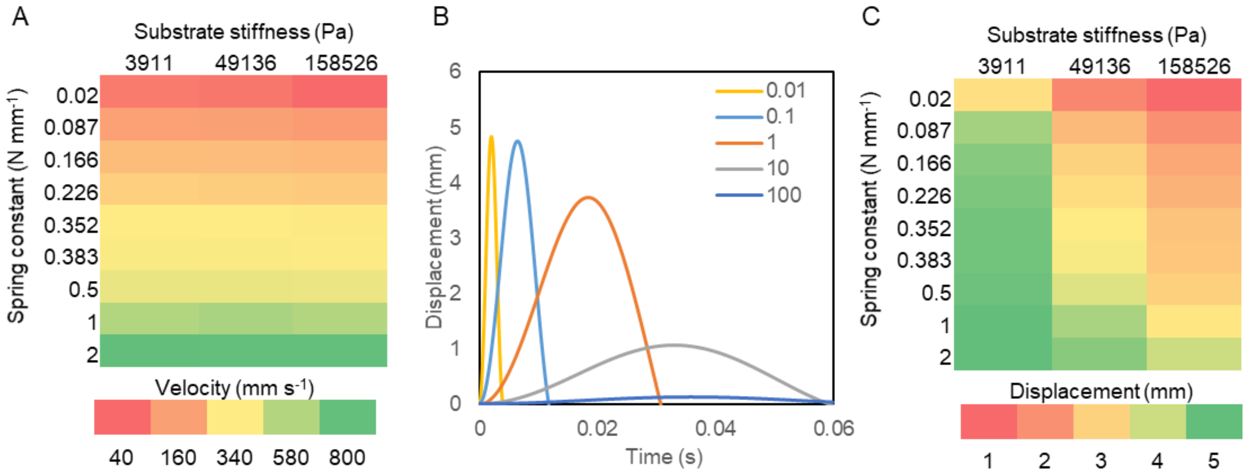

Figure 2.9: Results from mechanical modelling. (A) Velocity at 1 mm with respect to substrate stiffness and spring constant at a mass ratio of 1. (B) Displacement-time graph of the mass m_1 at different mass ratios travelling into the substrate during phase I. (C) Maximum displacement with respect to substrate stiffness and spring constant at a mass ratio of 1.

Second, a longer needle is always superior to a shorter needle. From the simulations, we observed that a surface with a lower Young's modulus was able to deform more (**Figure 2.9C**). Therefore, at a given load, the contact area between the needle tip and the surface will be larger for a surface with a lower Young's modulus. This in turn lowers the stress concentration at the needle tip and as such, the needle will have to translate deeper into the tissue in order to achieve puncture. Compared to shorter needles, longer needles can achieve a higher stress concentration, as they are able to translate deeper into the substrates and allow for puncture even on softer substrates. Moreover, a longer needle increases the duration of the needle insertion phase. A longer insertion phase allows for more kinetic energy to be dissipated by friction as the needle travels through the surface after puncture, which in turn reduces the impact and exit velocity after the copper plate impacts the surface. This allows a longer length of the needle to remain embedded in the surface, translating to a larger pull-out force. As such, if over-puncturing is not a concern in the design, a spring with the highest spring constant within the design limits should be used in tandem with a long needle, with the upper limit defined by the critical buckling load of the needle.

2.5.2 Equations of motion for the various stages

Between Stage I and II (**Figure 2.8B**):

I: Initial state – full compression of spring, no deflection of substrate.

II: Initial deformation – no cutting, pure deflection of substrate.

$$\sum F_x = ma.$$

$$\begin{bmatrix} m_1\ddot{x}_1 \\ m_2\ddot{x}_2 \end{bmatrix} = \begin{bmatrix} -k_{sub}x_1 + k_{sp}[L_{sp} - (x_1 - x_2) - D] \\ -k_{sp}[L_{sp} - (x_1 - x_2) - D] \end{bmatrix}.$$

$$\begin{bmatrix} \ddot{x}_1 \\ \ddot{x}_2 \end{bmatrix} = \begin{bmatrix} -\frac{k_{sub}+k_{sp}}{m_1} & \frac{k_{sp}}{m_1} \\ \frac{k_{sp}}{m_2} & -\frac{k_{sp}}{m_2} \end{bmatrix} \begin{bmatrix} x_1 \\ x_2 \end{bmatrix} + \begin{bmatrix} \frac{k_{sp}}{m_1}(L_{sp} - D) \\ -\frac{k_{sp}}{m_2}(L_{sp} - D) \end{bmatrix}, \tag{2.1}$$

where L_{sp} is the uncompressed length of spring, a is the acceleration of the needle tip and copper plate, m is the combined mass of the needle tip and copper plate and D is the distance between the needle tip and the substrate.

Between II and III (**Figure 2.8B**):

II: Initial deformation – no cutting, pure deflection of substrate.

III: Needle insertion – after cutting (energy dissipation), linear friction, substrate exerts constant pressure P on the needle, needle length L.

$$\sum F_x = ma.$$

$$\begin{bmatrix} m_1\ddot{x}_1 \\ m_2\ddot{x}_2 \end{bmatrix} = \begin{bmatrix} -k_{sub}x_1 + k_{sp}[L_{sp} - (x_1 - x_2) - D] - \mu_k N \\ -k_{sp}[L_{sp} - (x_1 - x_2) - D] \end{bmatrix}.$$

$$\begin{bmatrix} m_1\ddot{x}_1 \\ m_2\ddot{x}_2 \end{bmatrix} = \begin{bmatrix} -k_{sub}x_1 + k_{sp}[L_{sp} - (x_1 - x_2) - D] - \mu_k P\pi d(x_1 - x_p) \\ -k_{sp}[L_{sp} - (x_1 - x_2) - D] \end{bmatrix}.$$

$$\begin{bmatrix}\ddot{x_1}\\ \ddot{x_2}\end{bmatrix}=\begin{bmatrix}-\frac{k_{sub}+k_{sp}+\mu_k P\pi d}{m_1} & \frac{k_{sp}}{m_1}\\ \frac{k_{sp}}{m_2} & -\frac{k_{sp}}{m_2}\end{bmatrix}\begin{bmatrix}x_1\\ x_2\end{bmatrix}+\begin{bmatrix}\frac{k_{sp}}{m_1}(L_{sp}-D)+\frac{\mu_k P\pi d x_p}{m_1}\\ -\frac{k_{sp}}{m_2}(L_{sp}-D)\end{bmatrix}, \tag{2.2}$$

where $x_{1\,puncture}$ is the displacement of the needle at puncture, μ_k is the coefficient of kinetic friction and N is the normal contact force along the length of the needle.

At IV (**Figure 2.8B**):

IV: Maximum deflection – no net force on m_1, copper plate touches substrate.

$$\sum F_x = 0.$$

$$\begin{bmatrix}0\\ m_2\ddot{x_2}\end{bmatrix}=\begin{bmatrix}-k_{sub}x_1+k_{sp}\left[L_{sp}-(x_1-x_2)-D\right]-\mu_k N-N_{copper}\\ -k_{sp}[L_{sp}-(x_1-x_2)-D]\end{bmatrix}, \tag{2.3}$$

where N_{copper} is the normal contact force on the copper plate.

After IV (**Figure 2.8B**):

IV: Release of energy from substrate – no cutting, pure deflection of substrate, spring loses contact with m_1.

$$\sum F_x = ma.$$

$$m_1\ddot{x_1}=-k_{sub}x_1+\mu_k N. \tag{2.4}$$

2.5.3 Triggering mechanism

As the position of the mechanism could be accurately controlled by integrating it with wireless magnetic soft robots, the effects of distance and orientation on the anchoring and heating performance of the mechanism were investigated. First, the effects of parameters which could be controlled externally by a robot such as changing the distance away from the surface, D, and orientation, Φ, were investigated. It was observed that as the distance between the needle tip and the surface increased, the recorded pull-out force decreased (**Figure 2.10A**). 80% of the tested barbed needles, which were able to achieve the highest pull-out force previously, did not successfully penetrate the surface when the distance between the surface and the needle tip (i.e., D) was increased to 1 mm. The total extension of the spring used in this test was 4.2 mm. Similarly, at increasing Φ (**Figure 2.10B**), a drop in the performance of the mechanism was recorded. The decrease in performance can be explained by the decrease in the applied force. In the former, as the distance between the needle tip and the surface increased, the force which was applied by the spring to deform the surface decreased as the spring had extended more. In the latter, as some of the resultant force was directed to translate the needle parallel to the surface, less force was available to drive the needle into the surface. As such, in order to achieve higher pull-out force and thus better anchoring, it is better to place the mechanism closer and/or perpendicular to the surface.

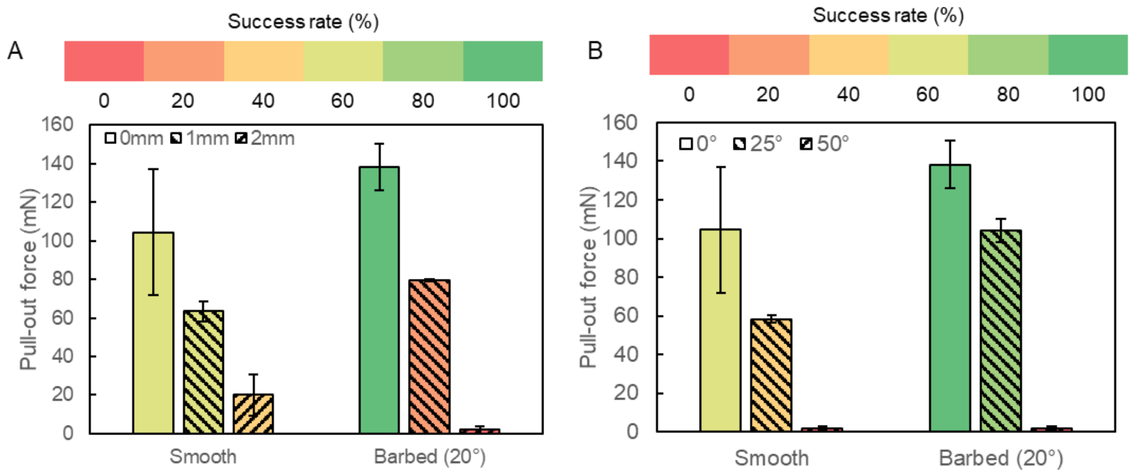

Figure 2.10: Mechanism characterisation and modelling. (A) Pull-out force with respect to the distance of needle from the substrate (n = 5). Error bars represent the standard deviation. (B) Pull-out force with respect to the angle of approach to the substrate (n = 5). Error bars represent the standard deviation.

Next, the effects of distance and orientation on the maximum heating achieved by the copper plate were investigated (**Figure 2.11A**). As the distance between the copper plate and the RF heater, d, increased, the amount of generated heat decreased, indicated by the lower recorded temperature after 25 s of RF exposure. This was due to a rapid decay of the alternating magnetic field which induced less currents and hence, decreased the rate of heating of the copper plate. As a result of this reduced rate of heating, the temperature rise became independent of the thickness of the copper plate. For instance, based on the simulations, although there was a substantial difference in temperature of over 70 ℃ between the 0.9 mm-thick plate and the 0.3 mm-thick plate at a distance of 0.01 m, the temperature difference was less than 1 ℃ at a distance of 0.03 m (**Figure 2.11B**). We validated the simulations by comparing the results obtained from the experiments with those obtained from the simulations (**Figure 2.11D**). As such, to reach the required temperatures at larger distances, the RF field needs to be applied for longer durations or at higher frequencies and amplitudes.

Without increasing the input current, frequency, or duration of RF exposure, the heating rate could be increased by changing the orientation of the heater with respect to the triggering mechanism. In this regard, the major axis of the heating plate was aligned such that it was parallel to that of the RF coils (ϕ = 90°). In doing so, the working distance could be increased by 75% to 3.5 cm (**Figure 2.11C, E**). This would be sufficient for use in organs directly under the abdominal skin, which has an average thickness of 2.6 cm to 3.1 cm [75], such as the bladder. This can be further increased as the diameter (i.e., volume) of the heating plate is increased (**Figure 2.12A**), although it has to be balanced against limits imposed by the intended operating environment. For instance, a 0.1 mm-thick heating plate with a diameter of 4.5 mm, which could be deployed in the bladder [76], was able to reach a temperature of 60 ℃ at a distance of 5 cm in our experiments. Due to the constraints imposed by the experimental setup, all the experiments in this work were conducted such that the copper plate was perpendicular to the RF coils (ϕ = 0°), which limited the maximum achievable heating. As such, it was necessary to place the device at a very close distance from the RF coils. However, if the magnetic coils used for actuation are also able to give a high-frequency oscillating field for remote heating, then a working distance of 3.5 cm can be achieved with the current setup.

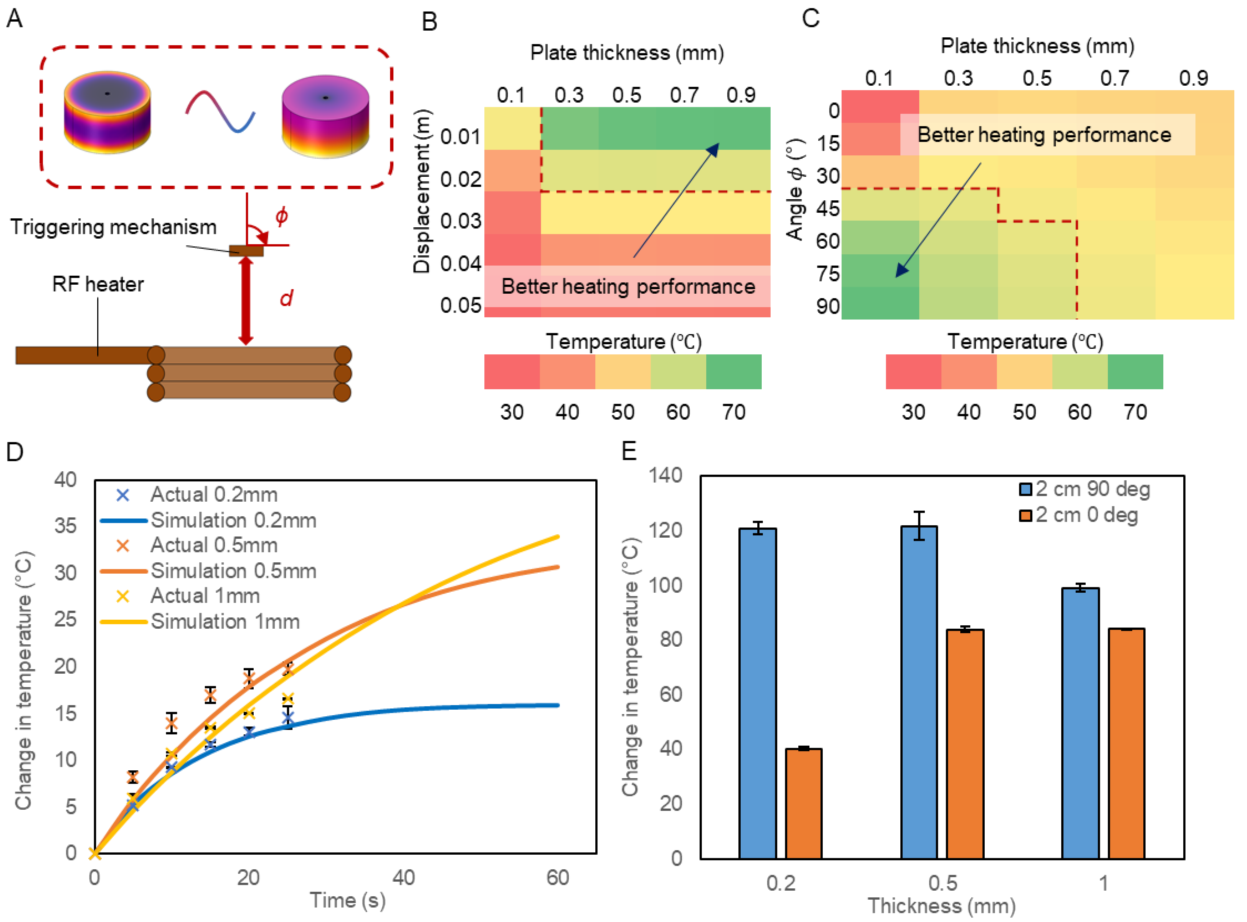

Figure 2.11: Triggering mechanism characterisation and modelling. (A) Schematic of experimental setup for heating experiments. (B) Predicted temperature of the copper plate after 25 s with respect to plates of varying thicknesses and distances at a constant angle $\phi = 0°$. Red dotted line indicates that the temperature has exceeded 60 °C. (C) Predicted temperature of the copper plate after 25 s with respect to plates of varying thicknesses and angles at a constant distance of $d = 0.02$ m. Red dotted line indicates that the temperature has exceeded 60 °C. (D) Temperature rise of copper plate of varying thicknesses (w = 0.2 mm, 0.5 mm, 1.0 mm) predicted from finite element simulation plotted against experimental values at $d = 0.03$ m, $\phi = 0°$ (n = 3). Error bars represent the standard deviation. (E) Difference in temperature due to a change in angle at $d = 0.02$ m (n = 3). Error bars represent the standard deviation.

To further extend the range of the device, insulating layers can be added to the heating plate to minimise the heat dissipated to the surrounding environment. For instance, when a thin insulating polyimide layer of 50 µm was added to the outer surface of the copper plate (i.e. side exposed to DI water), the temperature rise on the surface was reduced by over 20 ℃ (**Figure 2.12B**), indicating that more of the generated heat was directed to the side with the adhesive. This not only allows the device to operate at a longer distance, but also protects the tissues from being heated by the copper plate during triggering. From the simulations, we also find that increasing the input current amplitude is a more effective strategy as compared to increasing the frequency of the RF field (**Figure 2.12C, D**).

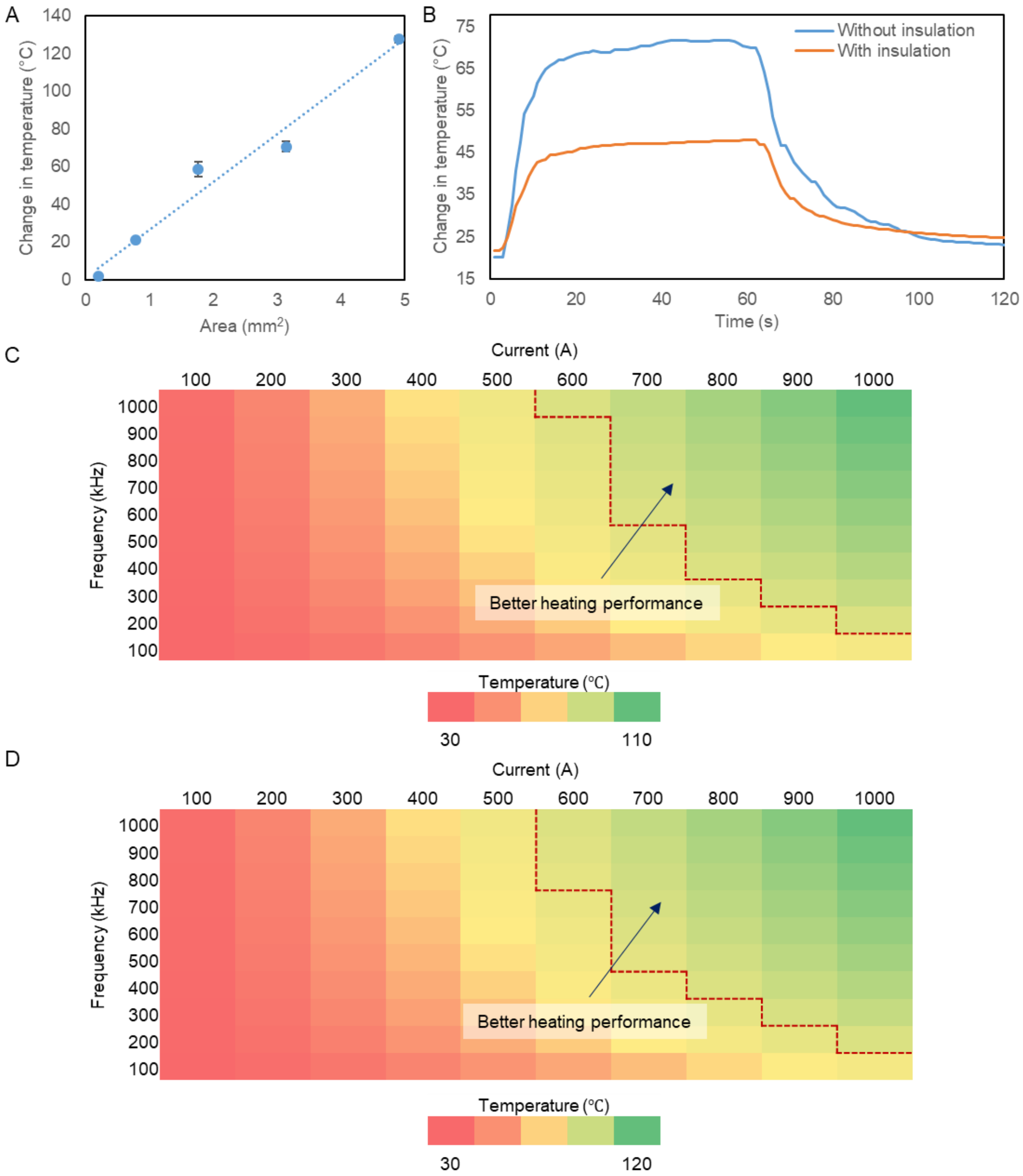

Figure 2.12: Heating characterisation and modelling. (A) Temperature of the copper plate after 25 s of RF exposure at a distance of 0.02 m (n = 3). Error bars represent the standard deviation. (B) Temperature against time graph of the outer surface of the copper plate with and without insulation. Device is submerged in DI water. (C) Predicted temperature of the copper plate after 25 s at a constant angle $\phi = 0°$ and distance of 0.03 m. Red dotted line indicates that the temperature has exceeded 60 ℃. (D) Predicted temperature of the copper plate after 25 s at a constant angle $\phi = 90°$ and distance of 0.03 m. Red dotted line indicates that the temperature has exceeded 60 ℃.

2.6 Proof-of-concept demonstrations towards medical applications

As proof-of-concept demonstrations, we tested the anchoring capabilities of our mechanism-integrated soft millirobots in various simulated ex-vivo environments. To verify if the needle had indeed achieved successful penetration of the tissue, we deployed the mechanism on an ex-vivo porcine bladder and took micro-computed tomography (micro-CT) images (**Figure 2.13A**). Given that there are constant dynamic motions and a variety of fluids inside the human body, we then tested the robustness of the triggering mechanism. In this regard, we submerged the mechanism in simulated body fluids and environments, and observed if they could be accidentally triggered. **Figure 2.13B** shows that the device was stable over a period of 24 h over a variety of simulated

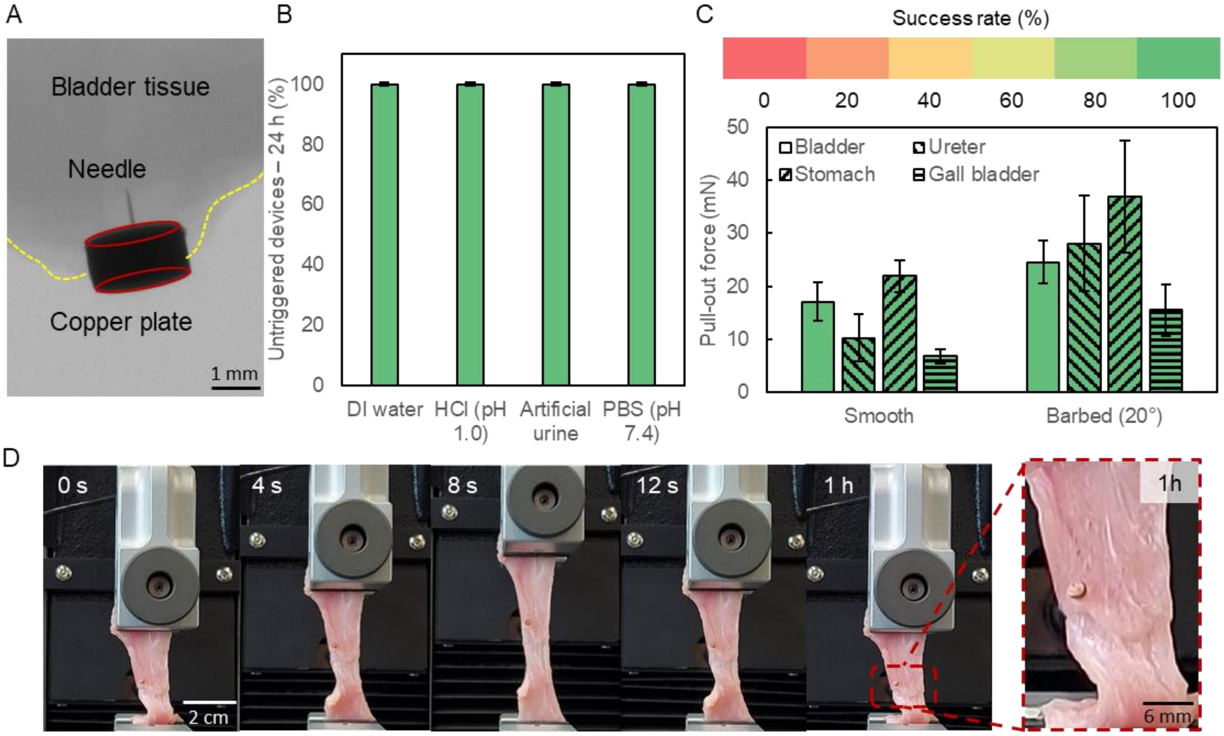

Figure 2.13: Demonstration of the proposed anchoring mechanism on ex vivo tissues. (A) Micro-CT image showing anchoring of the device on ex-vivo bladder tissue. The yellow and red lines represent the boundary of the bladder tissue and the orientation of the copper plate, respectively. (B) Robustness of the mechanism in various simulated body fluids (n = 5). Error bars represent the standard deviation. (C) Pull-out force of the needle on biological tissues (n = 5). Error bars represent the standard deviation. (D) Experiment to simulate dilation and relaxation of the bladder.

body fluids, highlighting the robustness and insensitivity of the triggering mechanism to biological fluids. **Figure 2.13C** shows the pull-out force required in organs found in the urinary and gastrointestinal tract.

Even though there was a drop in the pull-out force as opposed to the surfaces used in the characterisation tests, the effect of the barb in enhancing the anchoring force was still evident. The decrease in anchoring force can be primarily attributed to the increase in the fracture toughness of biological tissues (e.g., muscles, cartilages, connective tissues) [77], which is measured to be in the order of 1 kJ m^{-2} [78]–[81] as compared to 0.3 kJ m^{-2} for PDMS (**Figure 2.7D**). The recorded force was also comparable to those recorded by the barbed needles in literature (**Table 2.3**). We then applied cyclic extensional strains to an ex-vivo bladder tissue after successful anchoring of the mechanism onto it. Even after the bladder tissue was subjected to a strain of 100% for 100 cycles over an hour, we observed that the needle remained firmly attached to the surface of the bladder, indicating the robustness of the anchoring (**Figure 2.13D**).

Table 2.3: Comparison of the pull-out forces. Barbed needles in biological tissues across designs reported in literature.

Design	Height (mm)	Diameter (µm)	Penetration force (N)	Pull-out force (N)	Reference
Honeybee	2	200	0.125 (rabbit skin)	0.073 (rabbit skin)	[82]
Backwards barbs	4	400	0.416 (chicken muscle)	0.176 (chicken)	[83]
Porcupine	5	200	0.03 (muscle)	0.031 (pig skin)	[84]
Swelling tip	0.7	280	0.092 (pig skin)	0.012 (pig skin)	[44]
This work	1	100	0.95 (regardless of substrate)	0.036 (pig stomach) 0.025 (pig bladder)	-

Next, we integrated the mechanism with a jellyfish-inspired soft millirobot to allow for accurate navigation inside open fluid-filled environments such as the bladder. The jellyfish robot was able to carry the anchoring mechanism, trigger it while it was still swimming and perch itself onto an overhanging bladder tissue (**Figure 2.14A**). On the other hand, for procedures in confined spaces inside the body, such as the ureter and urethra, we incorporated the mechanism with a conventional sheet-shaped soft millirobot. The mechanism was also compatible with existing medical imaging techniques, such as ultrasound (**Figure 2.14B**). These demonstrations highlight the potential of integrating the proposed anchoring mechanism on various wireless soft millirobots. In all of these demonstrations, the RF field was turned on for less than 1 min to trigger the anchoring mechanism. To ensure that there was minimal heating of the tissue, we exposed bladder tissues to the same field for 1 min and observed that there was a negligible increase (< 0.2 ℃) in temperature. We also anticipate minimal nerve and muscle stimulation, which occurs at frequencies below 10 kHz [85]. The applied 338 kHz field is also close to those provided by electrosurgical units in use by hospitals today (500 kHz – 3 MHz) [86].

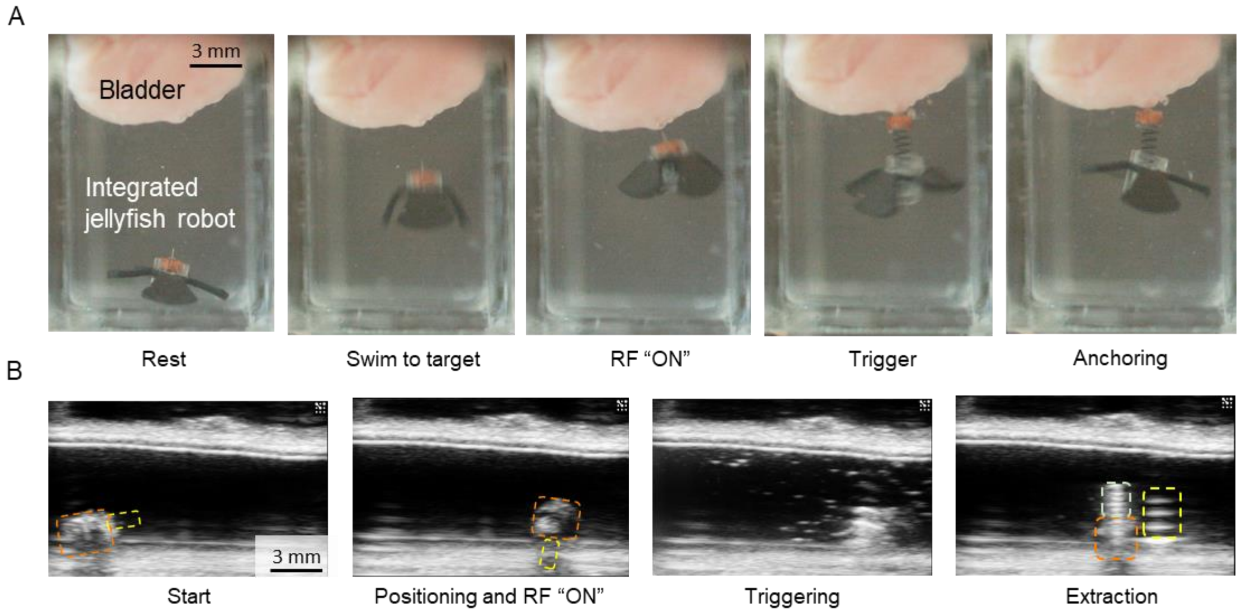

Figure 2.14: Integration of the proposed anchoring mechanism with existing soft magnetic robots. (A) Mechanism integrated with a jellyfish robot for anchoring in fluid-filled 3D spaces. (B) Ultrasound images of the mechanism integrated with a sheet-shaped soft robot for anchoring in confined spaces. Orange, yellow and light green outlines represent the casing, needle mounted on copper plate and spring, respectively.

Lastly, we demonstrate how additional functionalities, such as controlled detachment and sub-surface drug delivery, can be incorporated simply by changing the needle type. In the former, we fabricated needles of different diameters with a bioresorbable magnesium-based alloy (Resoloy, MEKO) and anchored them on a 10:1 PDMS substrate. The needles and substrates were then placed in an incubator set at 37 °C to simulate the temperature of the human body. Over time, the magnesium alloy hydrolysed and degraded, allowing the copper plate, which was initially attached to the needle, to detach from the anchored PDMS surface. By controlling the diameter of the needles, the detachment time could be altered from 1 day to almost 2 weeks (**Figure 2.15A, B**). Degradation primarily occurred along the needle that was not embedded in the surface and exposed to water (**Figure 2.15C**). Such a function might allow for passive retrieval of the anchored components – for long-term in-situ sensing or sample collection – at a specific time. For example, since the diameter of the copper plate used in this work is 2 mm, the copper plate and the other components can be passively expelled from the body if the device is deployed in the bladder. We do not anticipate any problems during this process as kidney stones with diameters less than 5 mm can already be spontaneously expelled by the body [76].

In the latter, we used hypodermic needles loaded with model drugs to demonstrate sub-surface drug delivery. Drug delivery to most tumour sites through the vascular system is highly ineffective due to factors such as a high interstitial tumour pressure or a leaky blood vessel [87]. As such, delivering drugs directly to the tumour site could potentially enhance therapeutic effects while lowering the required dose. Here, we demonstrate initial steps towards a functional device for in-situ drug delivery. By switching the solid needle with a hollow needle and preloading a model cancer drug, doxorubicin (DOX), into the needle, we were able to deliver DOX directly inside a tumour spheroid through diffusion (**Figure 2.15D**). To fabricate the needle, cotton wool was inserted by hand into hypodermic needles (23 G, Terumo Agani) and the sharp edge filed down to ensure that the cavity could be fully inserted into the spheroids during puncture. The hollow needles were incubated in 1 mg mL^{-1} doxorubicin hydrochloride (Sigma-Aldrich) solution overnight for drug loading before use.

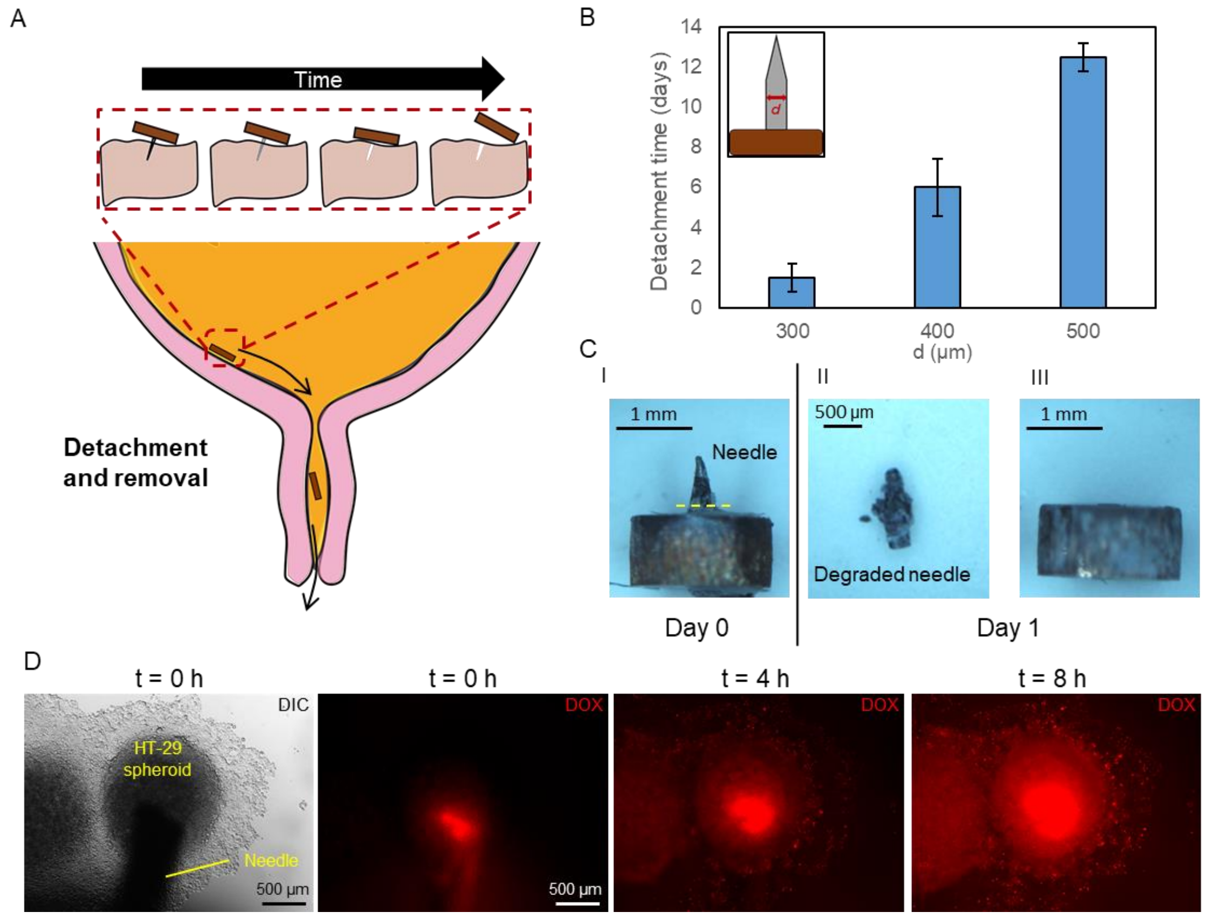

Figure 2.15: Multifunctional needle towards medical applications. (A) Conceptual illustration of controllable detachment and passive removal after anchoring. (B) Time to detachment of copper plate from the substrate using biodegradable needles of different diameters (n = 2). Error bars represent the standard deviation. (C) 300 µm-diameter biodegradable needle before and after degradation. (I) Image taken on day 0 before it was anchored on a 10:1 PDMS substrate. Yellow line indicates the degradation site. (II) Image taken on day 1, after the structure had been submerged in DI water in an incubator at 37 ℃. Close up photo of the needle. The needle (left) was removed from the PDMS substrate for imaging. (III) Detached copper plate. (D) Doxorubicin (DOX) delivery to HT-29 spheroids. The needle was punched into the HT-29 spheroids and time lapse images were recorded. The fluorescence signal of DOX distributed in the spheroid in time, demonstrating the drug release capability of the needles.

2.7 Preliminary biocompatibility tests

To demonstrate the biocompatibility of long-term anchoring on tissue surfaces, we cultured the needles with a human fibroblast cell line. We seeded the fibroblast cells on top of the needles and observed their viability after 72 h of culture. The fibroblasts demonstrated clear viability in the culture environment and at the interface of the needle while having spindle-shaped, healthy morphology (**Figure 2.16A**). The confocal microscopy analysis also revealed 3D migration of fibroblasts towards the needle surface after 72 h, demonstrating the biocompatibility of the needle interface (**Figure 2.16 B, C**). To demonstrate that the needles and the by-products released during degradation were non-toxic (**Figure 2.16D**), the base material of the needle was ground into powder and cultured with the fibroblasts at different concentrations. The cell viability analysis showed that the by-products of degradation (up to the concentration of µg mL^{-1}) did not cause any adverse effect on the cells after 72 h, demonstrating the versatility and compatibility of the material (**Figure 2.16E**).

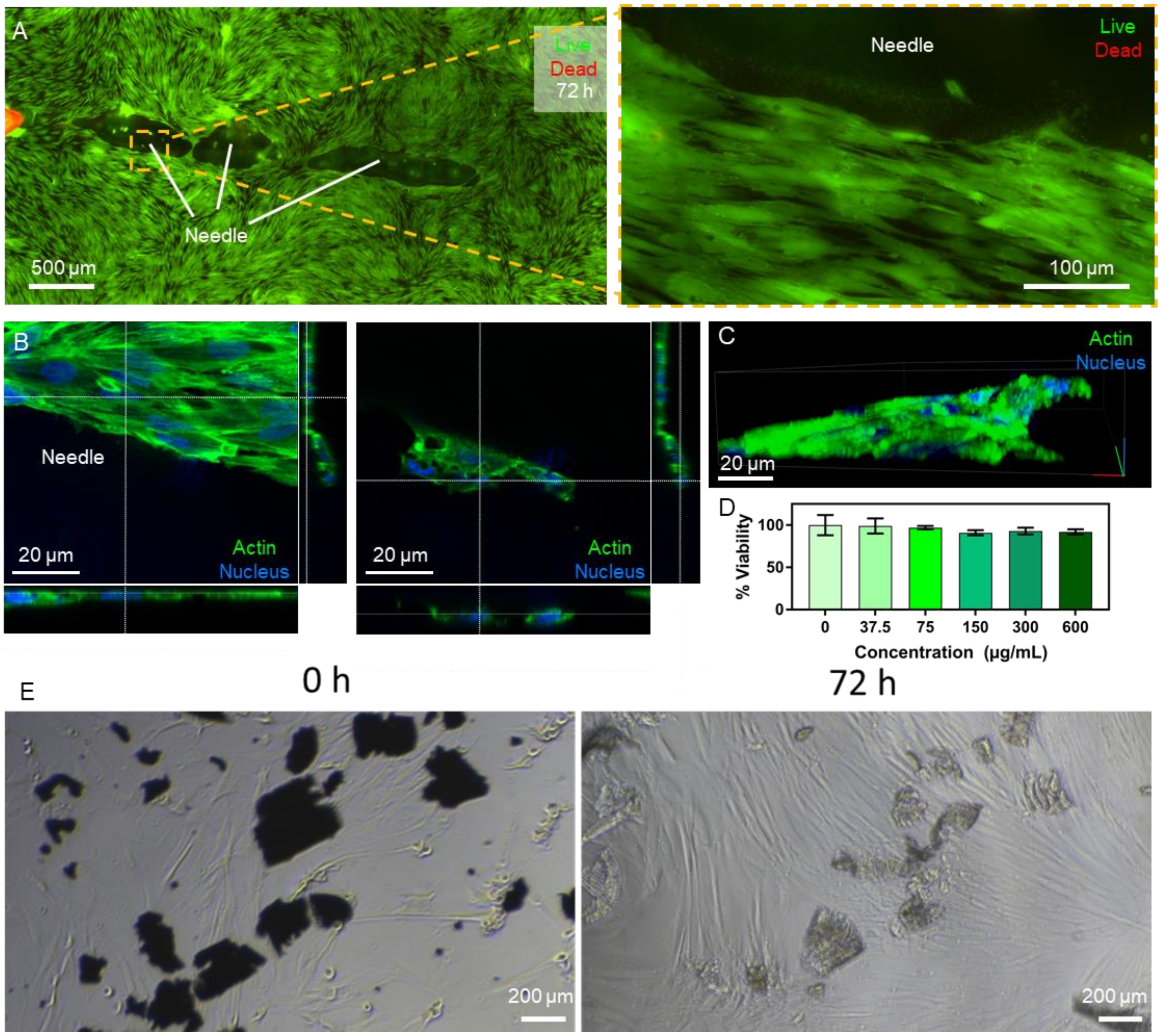

Figure 2.16: Results from the initial biocompatibility tests. (A) Live-dead staining of fibroblast cells cultured with the biodegradable needle. The cells were fully viable after 72 h of culture and displayed healthy morphology even at the interface of the needle. (B) Confocal microscopy analysis of the cells at the interface of the needle. The left and right images show the different z-levels of the same image, the latter being higher level. The right image shows grown cells towards +z direction of the needle. (C) 3D constructed confocal microscopy image showing the cell growth on +z direction of the needle. (D) Cell viability as a function of the needle powder concentration after 72 h of treatment, based on adenosine triphosphate (ATP) production. The cells showed more than 90% viability even at relatively high concentrations. Error bars represent the standard deviation. (E) Degradation of the needle (powdered) after 72 h. The images were taken from random areas of the wells. The shape and the colour of the powder particles have dramatically changed due to degradation.

2.8 Summary

Alex et al. demonstrated a spring-loaded mechanism that could provide the necessary force to deliver a barbed needle into the soft tissue surface [61]. However, there was no active control over the release time and the position and orientation of the device once it was swallowed. Moreover, the needle release mechanism was passively triggered by changes in the environment, making it highly dependent on and specific to the local environmental conditions. In this work, we demonstrate a mechanism which can be wirelessly triggered to generate the high normal forces required to drive a needle into a specific location on a soft surface for on-demand anchoring. By placing a barb on the needle, the pull-out force was increased by up to 38%, enhancing the long-term anchoring capability of the mechanism. Guidelines to optimise the triggering and anchoring performance of the proposed mechanism were established. Most importantly, the mechanism was small and light enough to be mounted on existing soft magnetic millirobots. The locomotion and anchoring capabilities of these integrated robots on ex vivo tissues were then demonstrated. Initial steps towards functional medical devices demonstrating controlled detachment and drug delivery were achieved by using bioresorbable needles of different diameters and hypodermic needles, respectively. Overall, these functionalities highlight the possibility of using such untethered robots in medical applications.

For successful translation, future studies should concentrate on three aspects. Firstly, the safety of an exposure to RF fields should be assessed with in-vivo experiments. Although ICNIRP provides general guidelines, these restrictions can be exceeded in application-specific instances (e.g. MRI) and are commensurate with the risk and benefit to the patient. However, in cases where such an exposure is not advisable, focused ultrasound can be used to heat up the triggering mechanism instead (51). Secondly, we note that all the materials used in the fabrication of the mechanism have biocompatible equivalents, which are being used in devices designed for long-term use inside the human body (**Table 2.4**). Nonetheless, histological studies to verify the safety of the heated plate impacting the tissue surface and the immune response of the tissue to the long-term anchoring of a foreign device should be conducted before in-vivo experiments are performed to minimise pain to the animals. Lastly, future studies should investigate the possibility of incorporating additional functions. For instance, in the drug delivery demonstration, hollow needles can be fabricated using other biodegradable materials with specific degradation mechanisms. An example of such a material is silk fibrin, which can be degraded enzymatically by protease (**Figure 2.17**). Having this design flexibility will provide more options for specific target medical applications. Addressing these issues would further enhance the capabilities of this mechanism and can potentially enable a range of minimally invasive long-term medical procedures, which are currently unavailable.

Table 2.4: Materials used for the mechanism in this work and their biocompatible equivalents.

Part	Current material	Biocompatible equivalent	Remarks
Casing	Clear Resin (Formlabs)	BioMed Clear Resin (Formlabs)	USP Class VI certified
Spring	Elgiloy	-	Used in implants, orthodontic wires, medical instruments, orthopaedic fixtures
Copper plate	Copper	-	Used in intrauterine devices
Needle	Stainless steel	Mg-based alloy/ Silk	Stainless steel is used in implants. The Mg-based alloy/ silk is biocompatible and biodegradable.
Barbs	IP-S (Nanoscribe GmbH)	IP-Visio (Nanoscribe GmbH)	ISO 10993-5 / USP 87 non-cytotoxic certified
Cyanoacrylate adhesive	Loctite 401/431 (Loctite)	Dermabond (J&J)	Used for wound closures

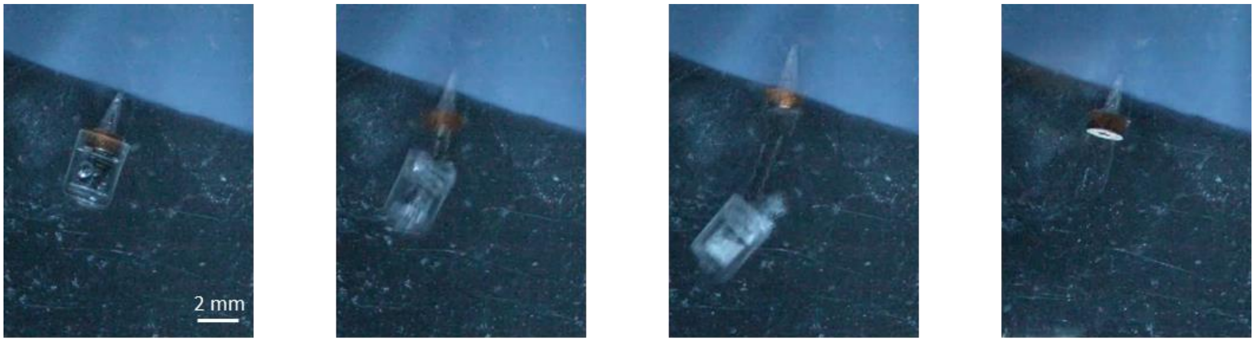

t = 0 s t = 0.01 s t = 0.011 s t = 0.015 s

Figure 2.17: Actuation sequence. Silk needle puncturing an agarose substrate (2% by weight). t refers to the time after actuation and not the duration of RF field applied.

Chapter 3: Pangolin-inspired untethered magnetic robot for on-demand biomedical heating applications

3.1 Background

Untethered miniature robots can harvest energy made available to them remotely, such as light, magnetic or acoustic energy, and convert them to other forms of energy, such as mechanical deformation [37], [88]. Magnetic actuation has emerged as a promising method for robots in biomedical applications due to the magnetic field's ability to penetrate human tissues safely [35], [36]. Furthermore, new developments in this field have enabled these robots to adaptively select their locomotion modes depending on the ambient temperature [89], [90] and achieve anchoring in both tubular [20] and highly unstructured 3D surfaces [65]. Despite these advances, the use of miniature magnetic robots in clinical applications is still limited because mainly one form of interaction, namely the mechanical interaction between the robot and the environment for locomotion or cargo delivery, is typically utilised.

In contrast, other forms of interaction between the robot and the environment are required in many biomedical applications. Heat energy, in particular, is a form of energy that is frequently used in common medical procedures, such as devitalisation, coagulation and cutting, making it a desirable function for untethered robots to possess (**Figure 3.1A**). There exist multiple methods to achieve remote heating, such as thermochemical, acoustics, photothermal and magnetic fields. Thermochemical methods are highly precise as the reagents are typically injected directly to the site and the products can usually be safely and easily excreted by the body [91]–[93]. Even so, the method is invasive and the heat produced cannot be easily localised. The reaction and the subsequent flow of reagents are highly dependent on environmental conditions, which cannot be easily controlled or predicted. Focused ultrasound is a non-invasive method for depositing energy on a target spot and not surrounding tissues [94]–[96]. However, ultrasonic waves are unable to pass through high-density materials, such as bones or if there is air-liquid interface. In the same vein, photothermal methods also offer precise heating but only have a maximum penetration depth of 2 cm under the skin [3]–[5]. This limits their applications to outer regions of the human body unless a light source is brought inside the body. As such, magnetic fields are the best stimuli to realise controllable, on-demand, non-invasive and targeted remote heating deep inside the human body.

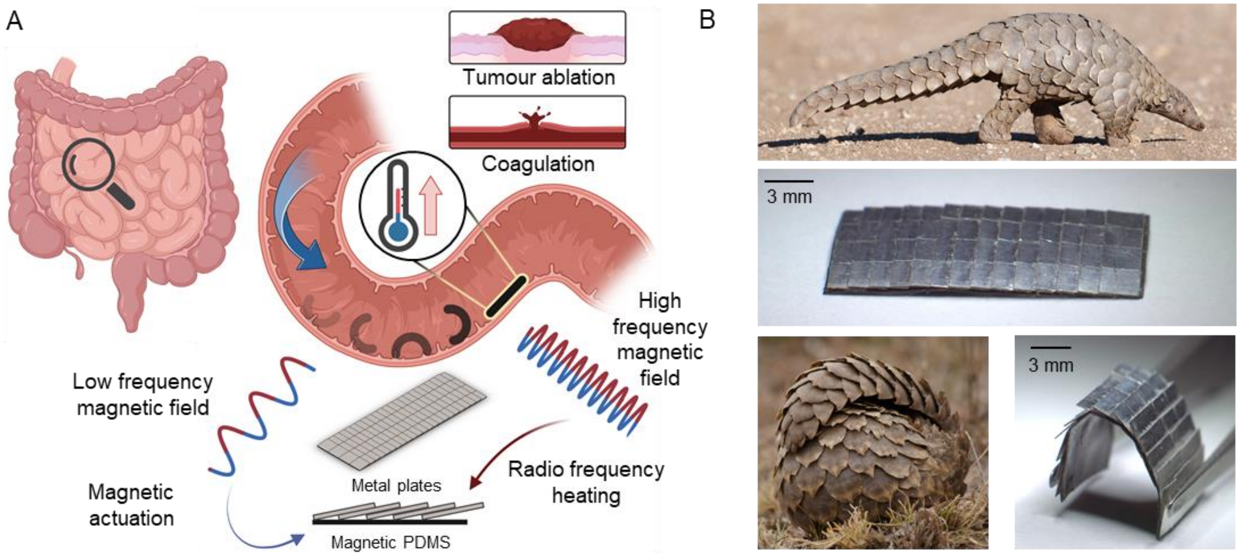

Figure 3.1: Proposed pangolin-inspired RF heating mechanism for untethered magnetic robots. (A) Conceptual illustration of the pangolin-inspired robot operating in the small intestine. The robot is actuated with a low-frequency magnetic field to the target location. Application of a high-frequency magnetic field results in Joule heating of the metal plates. The heat energy can then be used to interact with the environment. Inset on the right shows potential medical conditions in which a miniature untethered magnetic robot with heating capabilities would have utility. Figure created with biorender.com. (B) Armour on pangolins consist of individual overlapping hard keratin scales attached to the body. This design allows for rigid structures to be attached for protection without compromising on locomotion. Scaled robot inspired by this overlapping design is shown on the right. Images of pangolins used under licence from Shutterstock.

Remote heating can be achieved using alternating magnetic fields or RF fields via two mechanisms: Joule heating or hysteresis losses [97]. In the former, when there is a change in the magnetic flux through a closed wire loop, an electromotive force (emf) is induced as described by Faraday’s law. According to Lenz’s law, the induced emf is such that the induced current in the loop produces a magnetic flux which seeks to oppose the change. This current, also known as an eddy current, flows through the conductor and heats the body up through Joule heating in the process. In the latter, magnetic hysteresis results in energy dissipation, which directly heats up the material [68]. This process dissipates significantly less heat as compared to Joule heating, contributing to less than 10% of total heating based on literature [97] and simulations conducted in COMSOL for steel (3.88×10^{7} W m^{-3} and 1.42×10^{-13} W m^{-3} volumetric electric loss density and volumetric magnetic loss density, respectively).

Although exploiting magnetic hysteresis for remote heating has been extensively studied and utilised for robotic [26], [28], [98] and hyperthermia applications [99]–[101], magnetic hysteresis dissipates significantly less heat as compared to Joule heating. In fact, magnetic hysteresis remains a more popular method than Joule heating because the magnetic nanoparticles used simultaneously fulfil other functions of the robot and/or heating is not the primary output of these robots. For instance, the use of magnetic nanoparticles to achieve heating via magnetic hysteresis allows the material of the robot to still remain soft for large changes in volumes [26], [98] or because these nanoparticles have desired chemical or biological characteristics [100], [102]. While there is a third method of achieving remote heating with RF fields through the use of RF resonant circuits [103]–[105], we do not consider these methods because their RF coupling efficiency is less robust and they are unable to produce reliable, controllable remote heating. The coupling efficiency is highly dependent on environmental conditions, such as the ambient temperature, ionic content and concentration and even the physical deformation of the robot itself to name a few [106] – all of which are highly difficult to predict, especially in a highly heterogeneous environment, such as inside the human body [107].

To better illustrate the disparity in RF heating performance between Joule and magnetic hysteresis heating, we fabricated 1 cm × 1 cm square samples with a heating layer thickness of 100 µm, based on the methods previously reported in literature [25], [28], [98]. These samples were then exposed to the same RF fields at a distance of 5 cm. From the results (**Figure 3.2**), it was observed that there was no temperature increase for the methods relying on magnetic hysteresis (i.e., iron (II,III) oxide and magnetic PDMS). Therefore, to generate the required temperature differences, the devices had to be placed in the centre or on the surface of the RF coil, limiting the effective deployment range of these robots in meaningful biomedical applications. Only samples relying on Joule heating (i.e., 100 µm-thick aluminium and eutectic gallium indium (eGaIn) surface) could record a temperature change at 5 cm. In particular, the 100 µm-thick aluminium sample was able to generate the largest temperature change at such distances. As demonstrated in this work, any changes in either the electrical conductivity or geometrical properties would lead to a significant deterioration in the heating performance. For a robot utilising liquid metals for remote heating, the robot's own deformation would also change the electrical conductivity and geometrical properties of the liquid metal layer and affect the heating performance. As such, the use of liquid metals was ruled out in this work, as it would make the heating performance unpredictable and uncontrollable.

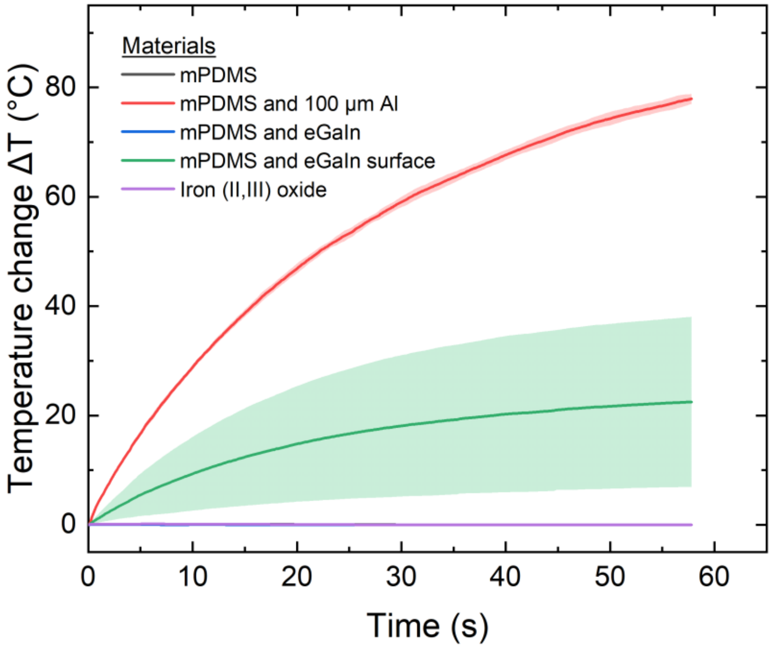

Figure 3.2: Experimental comparison of various methods of heat generation using an RF field at a distance of 5 cm (n = 6). All samples have a heating layer thickness of 100 µm and dimensions of 1 cm × 1 cm. As the samples made from mPDMS, mPDMS and eGaIn, and iron (II, III) oxide do not record any temperature change, the graphs of these samples overlap one another. Error bars represent the standard deviation.

3.2 Proposed approach

As demonstrated, rigid metallic body parts should be used for remote heating to ensure that the electrical conductivity and geometrical properties remain constant and stable for enhanced and reliable remote heating via Joule heating. However, the use of rigid materials inherently restricts and compromises the compliance of such untethered soft robots, taking away a key advantage of having a soft body with diverse shape programming capability. To address this inherent trade-off between effective remote heating at long distances and compliance, we observed how pangolins in nature could still achieve flexible and unencumbered motion despite having keratin scales, which are orders of magnitudes harder and stiffer than the underlying tissue layers, simply by organising the keratin scales into an overlapping structure [108]. Inspired by pangolins, an overlapping scaled design that allows users to concurrently realise on-demand thermal functionalities in tandem with shape-morphing and locomotion capabilities is introduced in this work. Heating of the metallic scales is controlled by an external 338 kHz RF field. The reported design allows for significant Joule heating ($\Delta T > 70$ °C) at large distances (> 5 cm), without compromising on the body compliance of these untethered soft robots (**Figure 3.1B**). Design strategies to optimise the performance of the heating mechanism based on simulations and experiments are also presented. Enabled by our understanding of the system, we displayed advanced robotic functionalities, such as in situ demagnetisation and selective cargo release. Initial designs and results for untethered soft robots that can potentially perform clinically relevant tasks, such as mitigation of bleeding and hyperthermia, are also presented.

3.3 Design and fabrication

To fabricate the device, grooves corresponding to the final design were laser cut into a metal sheet of the desired thickness. The grooves did not cut through the entire depth of the metal sheet to facilitate subsequent fabrication processes. For the overlapping structures, an additional step of engraving the metal at a lower power to indicate the extent of overlap was performed. The degree of overlap is defined as the exposed length over the total length of the scale in this work. The top and bottom surfaces were then cleaned with isopropyl alcohol (IPA). By simply bending the structures along the grooves outlining the outer perimeter, the cut structures were removed as a whole from the bulk metal sheet. Next, individual metal arrays corresponding to the rows in the design were separated from each other by bending and assembled on a piece of tape by hand to achieve the final design. The structure on the piece of tape were then bonded to the magnetic polymer (mPDMS) with pure 10:1 PDMS (**Figure 3.3**). The magnetic polymer was pre-programmed with the desired magnetisation profile prior to bonding with the structure. The resultant composite structure was then left on a hot plate at 90 °C for 2 h to allow the PDMS to cure. After curing, the tape was removed and the final robot was obtained after the scales in each row and column were separated into separate and distinct scales by bending with tweezers.

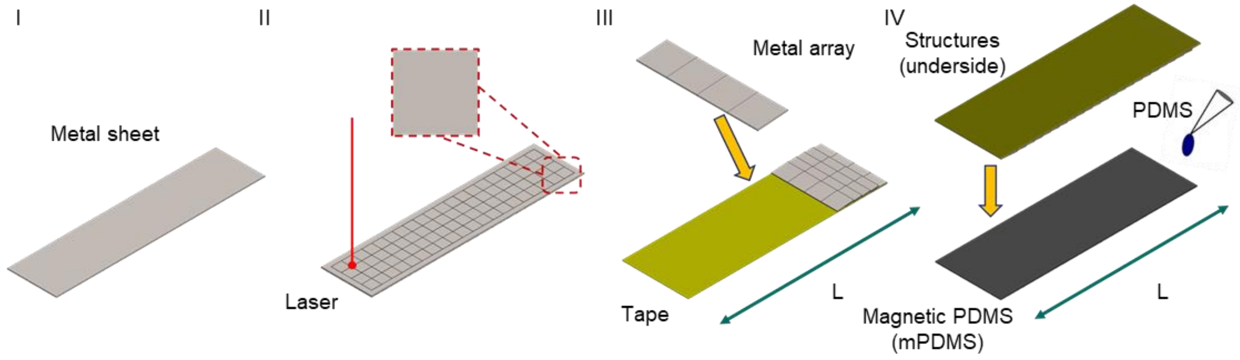

Figure 3.3: Fabrication procedure. (I) The metal of correct thickness and material is selected. (II) The sheet is laser cut to form the scaled patterns. (III) The metal arrays are assembled on a tape. (IV) The assembled structures on the tape are bonded to the magnetic PDMS with PDMS before the tape is removed.

To fabricate the wireless magnetic soft millirobot, polyethylene terephthalate (PET) tape (50650, Tesa) was placed along the sides of a 3 mm acrylic sheet to act as spacers. Next, NdFeB magnetic microparticles (MQP−15–7, Magnequench) were mixed with 10:1 PDMS in a 3:1 weight ratio, stirred for 5 min, degassed for 20 min and poured on the acrylic sheet. Excess mixture was removed with a doctor blade. To cure the mixture, the sample was left on a hot plate at 90 °C for 2 h before it was laser cut (ProtoLaser U3, LPKF Laser & Electronics AG) to the specified dimensions. The final structures were removed from the substrate and wrapped around a 6.4 mm diameter rod. Next, the structures were magnetised in a vibrating sample magnetometer (EZ7, Microsense) with a 1.8 T homogeneous magnetic field for 5 s. To ensure that the robots conformed well to the profile of the rod, a thin layer of water-soluble glue (822095, Pritt) was applied between the robot and the rod. After magnetisation, the robots were detached from the rod by soaking it in DI water. Excess glue on the surface was removed by further rinsing the robot with DI water. The metal scales, which have been prepared separately, were bonded to the robots with 10:1 PDMS. The robots, with the scales, were then left to cure on a hot plate at 90 °C for 2 h. A stereomicroscope (ZEISS Stemi 508, Carl Zeiss Microscopy GmbH) was used to guide the process wherever necessary.

3.4 Device characterisation

3.4.1 Heating characterisation

Unless otherwise stated, square samples with a side of 1 cm were used for the characterisation experiments. These samples were laser cut from a larger foil with the appropriate thickness. The samples were cleaned with IPA after laser cutting and bonded to a 12 mm × 12 mm microscope cover glass slide (0101000, Paul Marienfeld GmbH) with a 50 µm layer of silicone adhesive (Sil-Poxy, Smooth-On Inc.) and left on a hot plate to cure at 90 °C for 5 min. A 50 µm Kapton layer (KAP22-075, Thorlabs) with identical dimensions to the sample was attached to the top surface of the sample to eliminate any discrepancies arising from different emissivities when imaged with the IR camera. The RF heater was turned on for 60 s at 621.6 A. During the characterisation experiments, all the samples were placed 5 cm away from the edge of the RF coil. The samples were insulated at the bottom to prevent heat loss by conduction. The RF heater was turned on for 60 s and the resultant temperature rise was tracked with an infrared camera (ETS320, Teledyne FLIR) placed 7 cm above the samples. Three samples were tested twice each. The data from the infrared camera was saved on a computer using the software FLIR Thermal Studio. After the experiments, the data was exported from FLIR Thermal Studio. The average and standard deviation values across different runs were computed using MATLAB R2019A and visualised with Origin 2019b.

The objective of the optimisation was to maximise Joule heating per scale while minimising the load carried by the soft robot, since the added weight of the metal scales for heating adversely affects actuation. **Eq. 3.1** was defined to describe the underlying physics, direct the characterisation experiments and hence the overall design strategy of these scales:

$$P_{in} = \rho V c_p \frac{\partial T}{\partial t} + H_L, \tag{3.1}$$

where P_{in} is the input power, ρ is the density of the material, V is the volume of the material, c_p is the specific heat capacity at constant pressure of the material, $\frac{\partial T}{\partial t}$ is the rate of change of temperature and H_L is the heat losses.

Further details about **Eq. 3.1** and the assumptions used in its construction are provided in the next section. The heating performance is defined as the rise time ($\frac{\partial T}{\partial t}$) and the maximum temperature change in this work. From **Eq. 3.1**, we observed that the heating performance was dependent on the competing effects between heat generation, P_{in}, and heat loss, H_L. To maximise heating per scale, P_{in} has to be maximised while minimising H_L at the same time.

Based on an analytical analysis of **Eq. 3.1**, we observed that the electrical conductivity (σ) and geometrical properties, such as the length (L) and thickness (w), would be the dominant factors affecting the heating performance. Variations in σ, L and w directly affect the input power, P_{in} – the induced current density through the material and also the magnetic flux passing through the scale changes when these parameters change. Moreover, variations in L and w directly affect the heating performance as they simultaneously affect the heat losses, H_L, and the rate of change of temperature, $\frac{\partial T}{\partial t}$ – by changing the exposed surface area and the heating load, respectively. As such, the characterisation experiments and simulations focused on studying the effects of these factors on the heating performance (**Figure 3.4A, B**). Although RF heating on thin plates have been studied previously, the effects of this interplay between geometric and physical properties on heating efficiencies have not been studied extensively [109]–[112]. This serves as additional motivation for this section.

To maximise P_{in}, we first looked at the electrical conductivity. As the input power was directly proportional to the electrical conductivity from **Eq. 3.1**, a higher electrical conductivity should result in a higher temperature as the magnitude of the induced current density would be larger (**Figure 3.4C, D**). However, as the thickness of the plate is finite, the electrical conductivity cannot be increased indefinitely and there exists an optimal value (**Figure 3.4E**). This optimal electrical conductivity decreases as the thickness of the samples increases. As the thickness of the scale increased from 50 µm to 250 µm, the optimal electrical conductivity for heating decreased from 1×10^7 S m^{-1} to 2×10^6 S m^{-1}, respectively. For scales with a thickness of 100 µm, the optimal electrical conductivity was approximately 5×10^6 S m^{-1}, which was close to the electrical conductivity of tin. The simulations corresponded well with the experiments conducted with 100 µm-thick scales, where tin ($\sigma = 8 \times 10^6$ S m^{-1}) produced the best heating performance (**Figure 3.4F**). This maximum exists because the increase in the induced current density also leads to an increase in the magnetic field generated by per unit thickness of the scale to oppose the change in magnetic fields applied by the RF fields. Consequently, the magnetic flux from the RF coils penetrates less into the material (z-axis) for a scale with a larger electrical conductivity. Any additional material present above that thickness would only serve as a thermal load and not contribute to heating, resulting in the drop in the heating performance observed in **Figure 3.4E**.

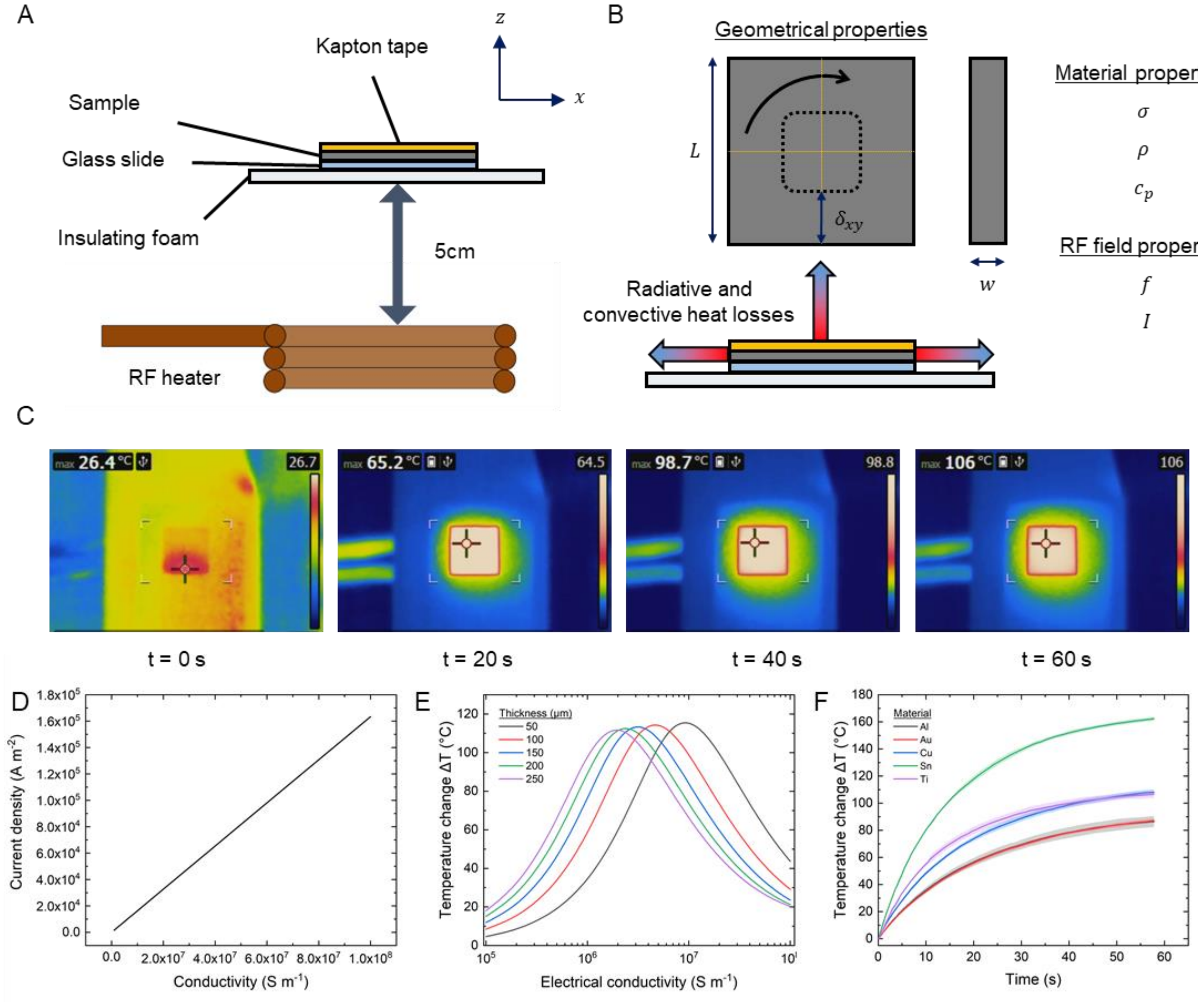

Figure 3.4: Characterisation of heating performance. (A) Schematic of experimental setup. (B) Identified parameters affecting Joule heating performance. (C) Infrared camera images tracking the temperature change of a 100 µm-thick aluminium scale over 60 s. (D) Simulated current density against electrical conductivity. (E) Simulated temperature at t = 60 s of the metal scales with varying electrical conductivities and thicknesses. (F) Temperature change of 100 µm-thick scales made from different materials over time (n = 6). Error bars represent the standard deviation.

This effect was observed in simulations where we tracked the changes in magnetic flux density through the centre of the material. Specifically, we observed that the magnetic field penetrated deeper into materials with lower electrical conductivities. For a 50 µm-thick 1 cm^2 square sample with electrical conductivities of 1×10^6 S m^{-1} and 1×10^8 S m^{-1}, the magnetic flux density at the centre of the material (i.e. 25 µm) into the material was 1.62 mT and 0 mT, respectively (**Figure 3.5A**). The same trends were observed in a 250 µm-thick material (**Figure 3.5B**). Since there was no magnetic flux density in the centre of the material as the electrical conductivity was increased, the induced currents were confined to a smaller region along the z-axis in materials with higher electrical conductivities.

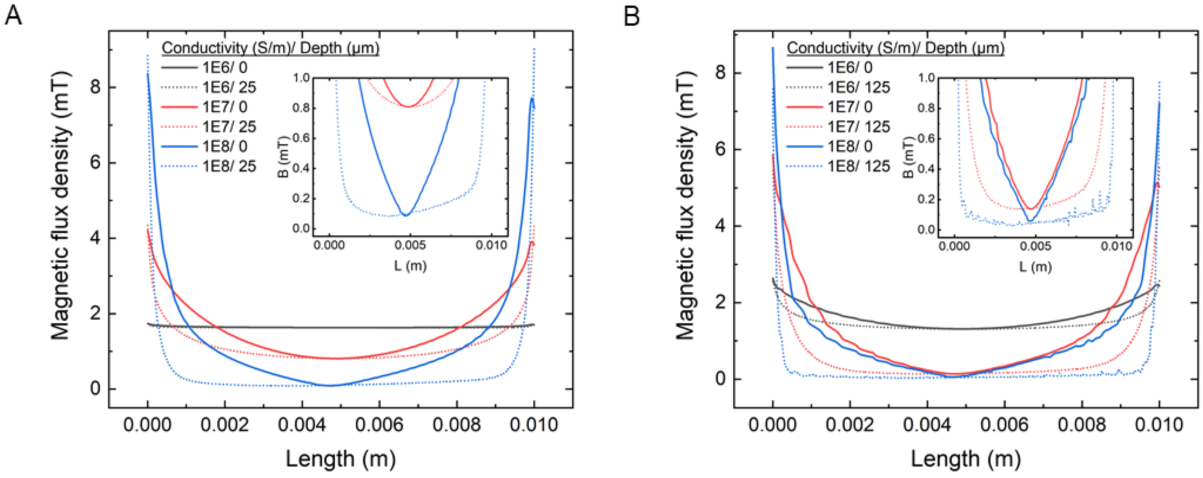

Figure 3.5: Simulated magnetic flux density. Different depths inside an aluminium scale. (A) 50 µm (B) 250 µm.

Apart from affecting the optimal thickness, changes in the electrical conductivity also resulted in a smaller skin depth, δ_{xy}. The formula for the calculation of the skin depth, δ_{xy}, is defined by **Eq. 3.2**:

$$\delta_{xy} = \sqrt{\frac{1}{\sigma \mu \pi f}}, \tag{3.2}$$

where σ is the electrical conductivity of the material, μ is the permeability of the material and f is frequency of the applied RF field.

Since the currents were now confined to flow in a narrower region, the length of the scale had to be decreased correspondingly to ensure that the entire material plane still contributed to Joule heating. As such, we hypothesised that there was an optimal electrical conductivity for every thickness and length. A plot of $\frac{1}{\delta xy}$ as a function of w was generated to condense the identified effects (**Figure 3.6A**). To validate this relationship, we characterised aluminium scales of different thicknesses ranging from 10 to 100 μm. For aluminium, the value $\frac{1}{\delta xy}$ was calculated to be 7.1 mm^{-1}. Using **Figure 3.6A**, the thickness of the scale had to be reduced to below 50 μm for optimal heating of a 10 mm scale. As shown in **Figure 3.6B**, the heating performance increased as the thickness decreased. The best performance was recorded at 20 μm for aluminium. If the thickness was further reduced, as shown in the 10 μm-thick aluminium scale, the maximum temperature generated started to drop. On top of generating a higher final temperature, another advantage of using thinner plates was that the rate of temperature rise was increased. As the plate thickness was decreased from 100 μm to 10 μm, the initial slope of the temperature-time graph increased (**Figure 3.6B-D**). The explanation for this is as follows.

Looking at **Eq. 3.1**, the heat losses at t = 0 s are zero since the metal will be at ambient temperature. As such, **Eq. 3.1** can be reduced to $\frac{\partial T}{\partial t} = \frac{P_{in}}{\rho V c_p}$, implying that all of P_{in} will be used to heat the scale. Consequently, materials with a lower $\rho V c_p$ (i.e., lower mass, volume and/or a specific heat capacity) will register a higher $\frac{\partial T}{\partial t}$, temperature rise. From the experiments, it was observed that a plate with a smaller thickness (less V) was able to generate heat at a faster rate than a thicker plate (**Figure 3.6B**). We also note that using a material with a lower density and/or the specific heat capacity as described by **Eq. 3.1** would also result in a higher $\frac{\partial T}{\partial t}$ (**Figure 3.10B, D**).

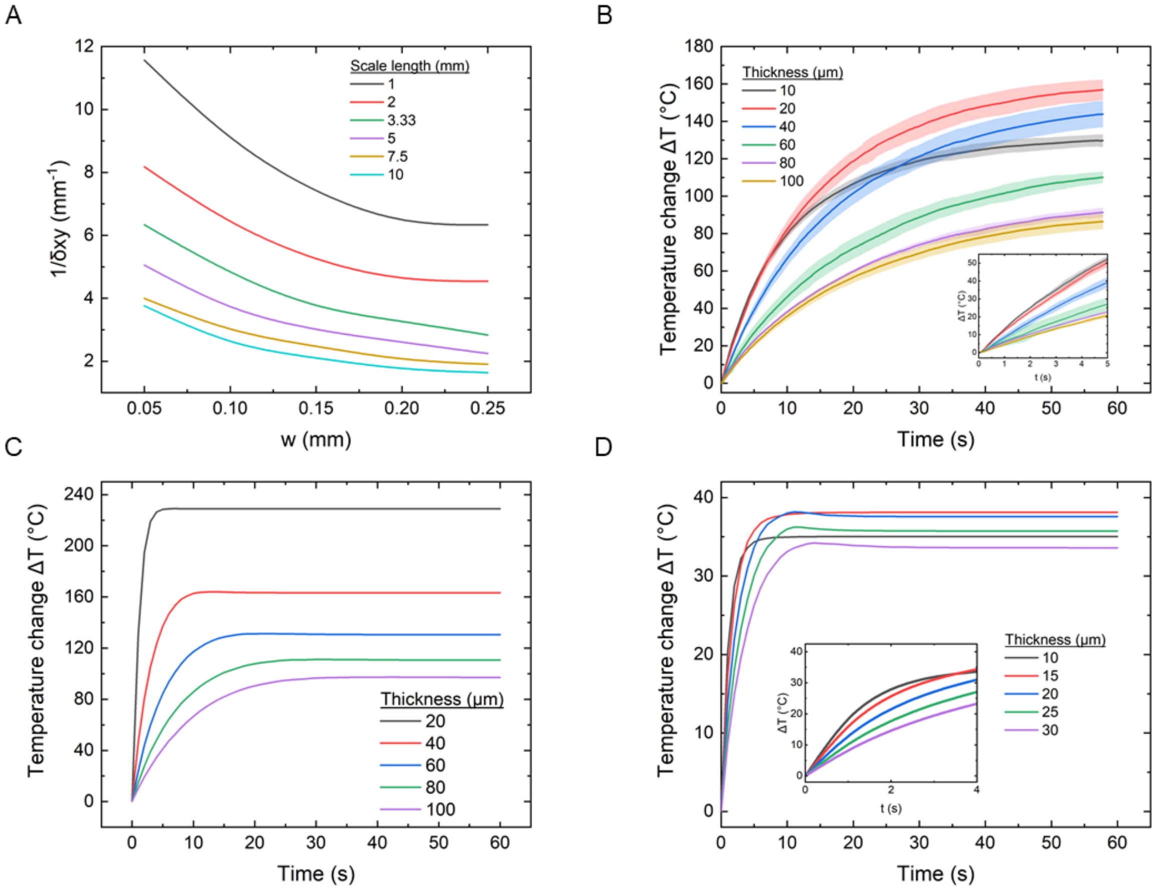

Figure 3.6: Characterisation of heating performance. (A) Simulated graphs for the selection of geometrical and material properties for optimal heating for different scale lengths. $\frac{1}{\delta_{xy}}$ on the y-axis represents the inverse of the skin depth. (B) Temperature change of aluminium scales with different thicknesses over time (n = 6). Error bars represent the standard deviation. (C) Simulated temperature change of aluminium scale with different thicknesses over time. (D) Simulated temperature change of aluminium scale with different thicknesses over time (for low thicknesses). Note that the simulated temperatures presented in this figure are lower than those presented previously because the metal scales are modelled with the thin shell approximation in COMSOL.

The optimal ratios presented in **Figure 3.6A** are also independent of the input current (**Figure 3.7**). Should a higher temperature be required with a smaller scale, a higher input RF current could be given to mitigate the decrease in heating performance arising from using a smaller scale. Moreover, since $\frac{1}{\delta xy}$ is also a function of the frequency, *f*, this implies that even if a more electrically conductive material is used, the same thickness can be used as long as the frequency is reduced to compensate for it.

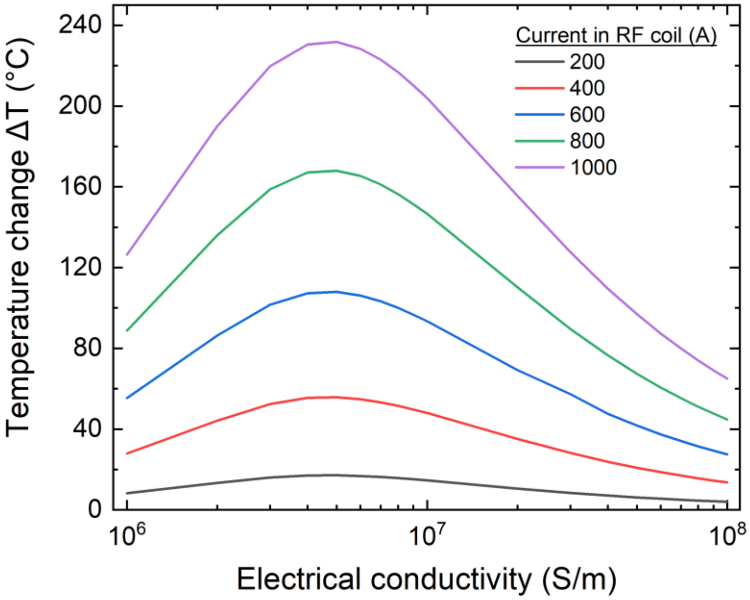

Figure 3.7: Simulated temperature change. 100 µm scale of different electrical conductivities when different currents are applied in the RF coil at t = 60 s.

As the use of scales with hierarchical arrangement to enhance flexibility and mechanical compliance in biological systems has been well-studied [113], [114], we looked into the effects of breaking up a single large structure into one composed of smaller scales. In this regard, the single 1 cm^2 metal scale was replaced with another of the same area, material and thickness, but composed of smaller scales. As the length of the scales decreased, the heating performance decreased. The drop in the heating performance occurred because the magnetic flux passing through each scale decreased, resulting in a lower induced emf and hence, temperature (**Figure 3.8A**). Even though the total area was kept constant at 1 cm^2, the maximum temperature dropped dramatically, up to 75% as compared to the uncut piece – since the maximum amount of heat that could be generated per scale was now reduced (**Figure 3.8B, C**). This indicates that there is a fundamental trade-off between mechanical compliance and heating with the use of scales.

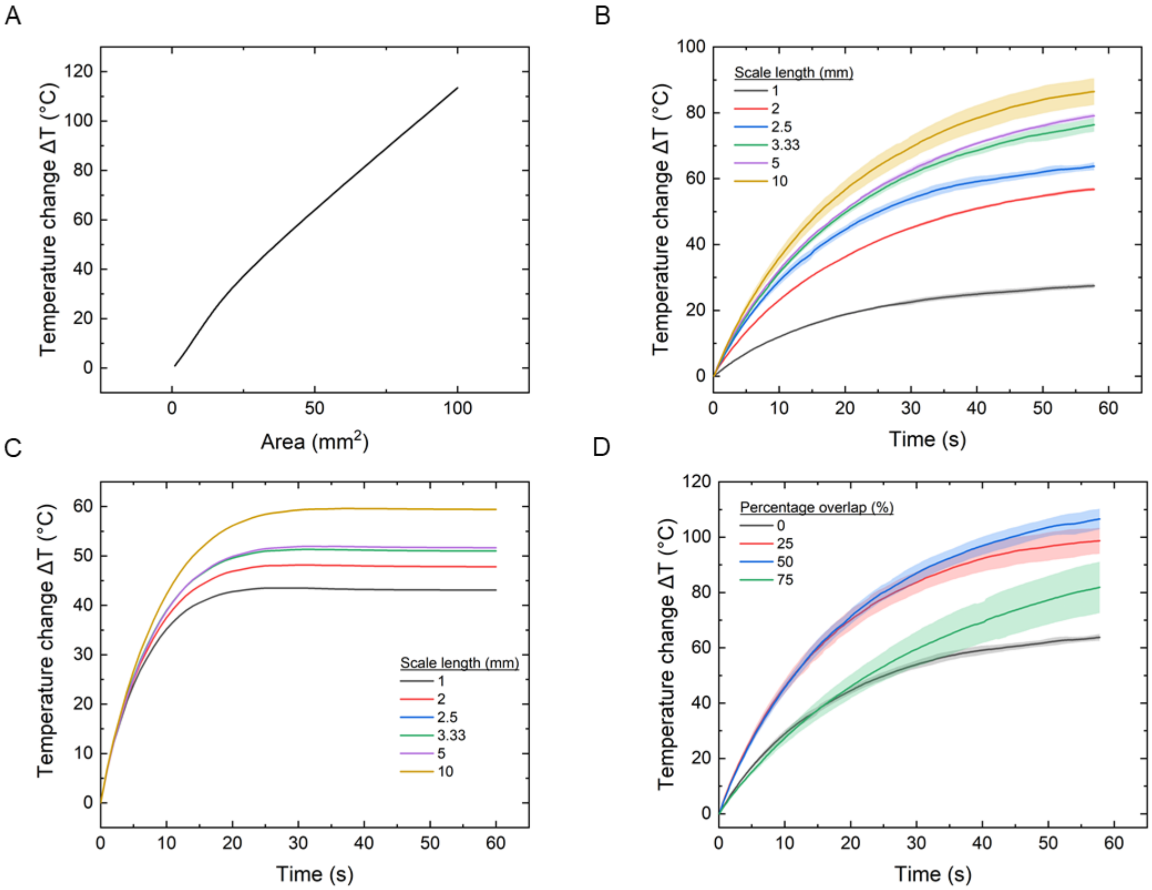

Figure 3.8: Characterisation of heating performance of smaller scales. (A) Simulated temperature change of a 100 µm-thick aluminium scale with different areas. (B) Temperature change of 100 µm-thick aluminium scales with identical areas but composed of different scale lengths over time (n = 6). Error bars represent the standard deviation. (C) Simulated temperature change of 100 µm-thick aluminium scales with identical areas but composed of different scale lengths over time. (D) Temperature change of 100 µm-thick aluminium scales with different percentage overlap over 60 s (n = 6). Error bars represent the standard deviation.

However, unlike other animals, such as armadillos [115], alligators [116] and lizards [117], which have scales arranged in a non-overlapping (i.e., osteoderm) configuration, the pangolin has overlapping scales, each of which are bonded directly to the underlying soft skin layer. This degree of overlap, or imbrication, ranges from 0.5 to 0.8 depending on the species [108]. We hypothesise that overlapping the scales would be advantageous for heating as it would increase the effective heating volume (i.e., P_{in}) while keeping any increase in exposed surface area minimal. As an example, for an equivalent 50 µm-thick sample with a fixed 1 cm^2 area, there would be a 75% increase in volume but only a 5.7% increase in the exposed surface area at 50% overlap. Since H_L is only proportional to the exposed surface area for a given change in temperature, this results in an overall gain in temperature since more volume is exposed to the RF field. As observed from **Figure 3.8D**, increasing the number of plates on the robot by overlapping the scales increased the final temperature after 60 s of RF exposure, by up to 67% depending on the configuration used. Using this strategy, the 100 µm-thick scales with 50% overlap was able to perform as well as a 60 µm-thick unscaled 1 cm^2 sample. This demonstrated that the pangolin-inspired overlapping design was able to compensate for the decrease in the temperature arising from the division of a larger scale into smaller scales whilst still providing the necessary mechanical compliance. The heat

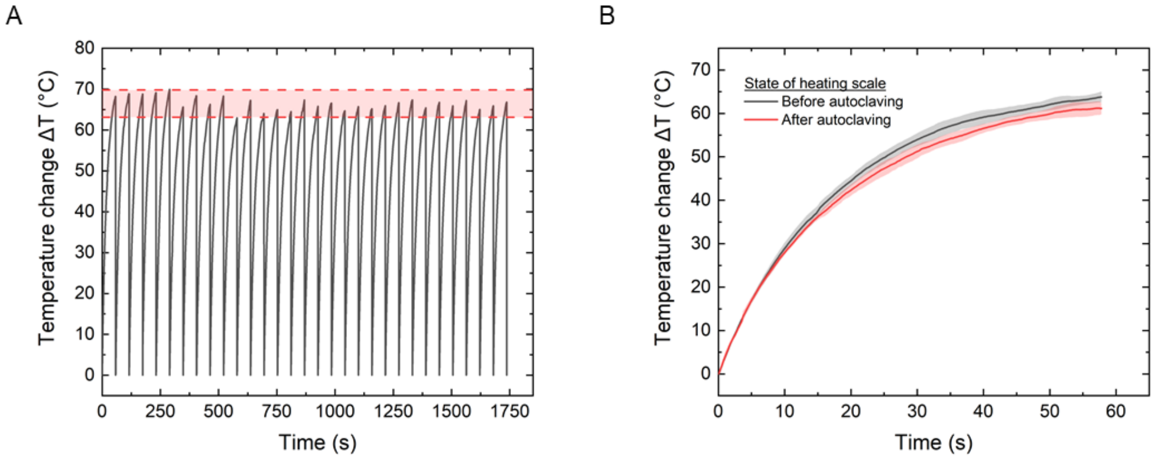

Figure 3.9: Repeatability of heating performance. (A) Temperature change of 16 non-overlapping 2.5 mm 100 µm-thick aluminium scales over 30 heating and cooling cycles. Region demarcated in red indicates the temperatures that fall within 5% of the average maximum value. Error bars represent the standard deviation. (B) Temperature change of 16 non-overlapping 2.5 mm 100 µm aluminium scales before and after autoclaving (n = 5). Error bars represent the standard deviation.

produced by the scales is also highly reliable and repeatable, with the maximum temperature reached varying by less than 5% over 30 cycles. Even after it was autoclaved, the heating performance degraded by less than 5% (**Figure 3.9**).

The effects of the other material properties on heating performance such as the specific heat capacity at constant pressure, c_p, thermal conductivity, k, and density, ρ, were also studied. Since the effects of each of the factors could not be independently studied in real life, simulations were used to study the effects. The range of values used in the simulations were kept within the limits of conductive materials found in real life. At t = ∞, the final temperature was independent of the density and specific heat capacity. The temperature of the scales in the simulations were independent of the thermal conductivity regardless of the time. At t = 1 s, a lower density and specific heat capacity would result in a higher rate of temperature increase. The results from the simulations are presented in **Figure 3.10**.

In summary, to achieve the best heating performance, the required mechanical compliance must be taken into consideration as it will determine the maximum size of a scale of L, and hence the thickness of the plate used (**Figure 3.6A**). Materials with a lower $\rho V c_p$ (i.e., lower mass, volume and/or a specific heat capacity) should be used to increase the rise time. Moreover, to overcome the disadvantages conferred by inducing cuts on the structure to increase the mechanical compliance, overlapping structures could be used. For ease of reference, the effects of changing the parameters are summarised and provided in **Table 3.1**.

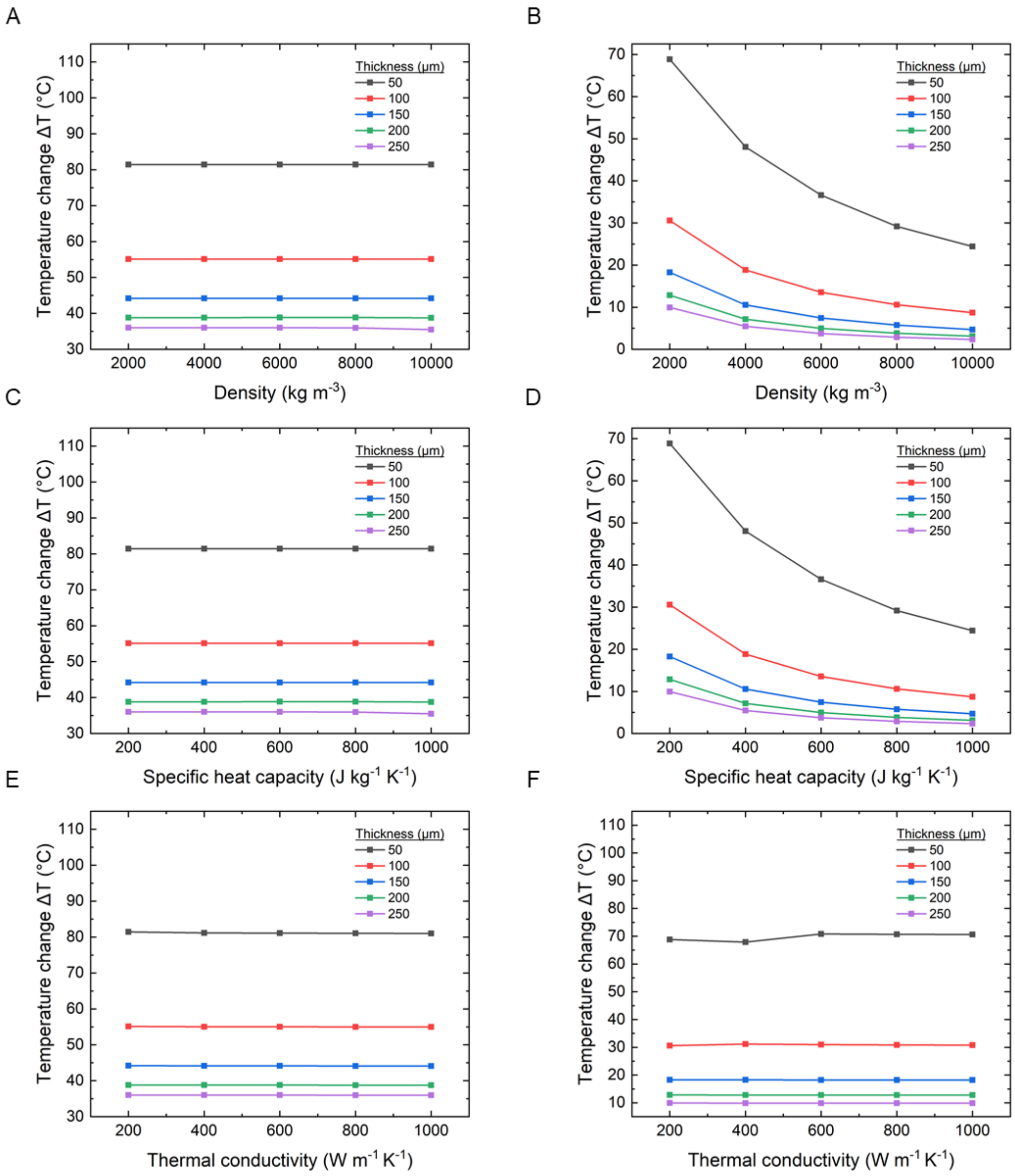

Figure 3.10: Characterisation of heating performance with simulations in COMSOL. (A) Simulated temperature change of a 100 μm-thick aluminium scale with different densities at t = 60 s. (B) Simulated temperature change of a 100 μm-thick aluminium scale with different densities at t = 1 s. (C) Simulated temperature change of a 100 μm-thick aluminium scale with different specific heat capacities at t = 60 s. (D) Simulated temperature change of a 100 μm-thick aluminium scale with different specific heat capacities at t = 1 s. (E) Simulated temperature change of a 100 μm-thick aluminium scale with different thermal conductivities at t = 60 s. (F) Simulated temperature change of a 100 μm-thick aluminium scale with different thermal conductivities at t = 1 s.

Table 3.1: Summary of the various parameters which can be controlled to optimise the heating performance of a single scale.

Control parameter	Classification	Effects	Considerations
L	Geometrical	Increasing L increases final temperature	$\frac{1}{\delta xy}$ must be kept constant Mechanical compliance
w	Geometrical	Increasing w decreases rate of temperature rise	$\frac{1}{\delta xy}$ must be kept constant Mechanical compliance
σ	Material	Increasing σ decreases w	$\frac{1}{\delta xy}$ must be kept constant
ρ	Material	Decreasing ρ increases rate of temperature rise	Mechanical compliance
c_p	Material	Decreasing c_p increases rate of temperature rise	-
f	RF field	Increasing f increases final temperature	$\frac{1}{\delta xy}$ must be kept constant
I_{in}	RF field	Increasing I_{in} increases final temperature	-

3.4.2 Mathematical model

Governing equation (per unit time)

Assuming no contributions from magnetic hysteresis, $T_{ambient}$ = 25 °C,

$$P_{in} = mc_p \frac{\partial T}{\partial t} + H_L.$$

$$P_{in} = \rho V c_p \frac{\partial T}{\partial t} + H_L, \tag{3.1}$$

where P_{in} is the input power, c_p is the specific heat capacity at constant pressure of the material in J kg^{-1} K^{-1}, $\frac{\partial T}{\partial t}$ is the rate of change of temperature in K s^{-1} and H_L is the heat losses in W.

Generated heat

From Faraday's law, the change in magnetic field, $\frac{\partial \mathbf{B}}{\partial t}$, induces a potential difference, $\mathbf{V_{in}}$, within the material with the following magnitude [97], [118]:

Since the plates are sufficiently far away (5 cm) and thin (< 300 μm), $\frac{\partial \mathbf{B_{applied}}}{\partial t}$ is assumed to be constant and homogenous.

Note: **B** does not necessarily refer to the $\mathbf{B_{applied}}$ because **B** decays as it travel through the material (i.e. current in preceding layers reduce the magnitude of **B** in the current layer).

$$\nabla \times \mathbf{V_{ind}} = -\frac{\partial \mathbf{B}}{\partial t}.$$

Since $\nabla . \mathbf{B} = 0, \mathbf{B} = \nabla \times \mathbf{A}$, where $\mathbf{A}$ is the magnetic vector potential,

$$\Rightarrow \frac{\partial \mathbf{B}}{\partial t} = \nabla \times \frac{\partial \mathbf{A}}{\partial t}.$$

$$\therefore \; \nabla \times \mathbf{V_{in}} = -\nabla \times \frac{\partial \mathbf{A}}{\partial t}.$$

$$\mathbf{V_{in}} = -\frac{\partial \mathbf{A}}{\partial t} - \nabla C, \tag{3.2}$$

where C = electric scalar potential.

Assuming material is ohmic $(\mathbf{J} = \boldsymbol{\sigma}\mathbf{V}_{\mathbf{in}})$, **Eq 3.2** becomes

$$\mathbf{J} = -\boldsymbol{\sigma}\frac{\partial \mathbf{A}}{\partial t} + \mathbf{J}_{\mathbf{s}}, \tag{3.3}$$

where $\mathbf{J}_{\mathbf{s}} = -\boldsymbol{\sigma}\, \nabla C$ = current density in the source (i.e. induction coil).

∴ At constant input power from the RF coil, $\mathbf{J}_{\mathbf{s}}$, the induced current density, $\mathbf{J}$, is directly proportional to the conductivity, $\boldsymbol{\sigma}$, which is an intensive property of the material.

For a thin layer where **B** can be assumed to be constant, $\mathbf{B}_{\mathbf{z}}$, and assuming an isotropic material,

$$\dot{P}_{layer_z} = \iint \frac{\mathbf{J}^2}{\boldsymbol{\sigma}} dA \approx \frac{\left[-\frac{d(\mathrm{B}_z.\mathrm{A}_\perp)}{dt}\right]^2}{\frac{\rho l}{0.5l}},$$

where $\mathrm{A}_\perp$= area perpendicular to the applied field (i.e. l^2 – square plate).

$$\Rightarrow \dot{P}_{layer_z} \,\alpha\, \sigma.$$

$$P_{in} = \int_o^h \dot{P}_{layer_z}\, dz \,\alpha\, \sigma \Rightarrow P_{in} \,\alpha\, \sigma. \tag{3.4}$$

<u>Heat loss</u>

Assuming incompressible flow and homogenous temperature throughout the scale.

Heat losses are caused by convective and radiative losses,

$$H_L = Convection + Radiation$$

$$= h_{top}A_{top}(T_s - T_{ambient}) + h_{side}A_{side}(T_s - T_{ambient}) + \sigma\epsilon A_{top\,\&\,side}(T_S^4 - T_{ambient}^4), \tag{3.5}$$

where σ is 5.67×10^{-8} W m^{-2} K^{-4}, ϵ is the emissivity of surface, A is the area in m^2 , T_s is the current temp of surface in K, $T_{ambient}$ is assumed to be 298.15 K and h is the convective heat transfer coefficient in W m^{-2} K^{-1}.

To calculate the convective heat transfer coefficient h [119],

$$Ra = Gr_{l_c} Pr = \frac{\beta(T_s - T_{ambient}) l_c^3 g}{\eta \alpha}. \tag{3.6}$$

β is the coefficient of thermal expansion at 25 °C (3.38×10^{-3} K^{-1}), g is the gravitational acceleration (9.81 $m\ s^{-2}$), l_c is the characteristic length in m, T_s is the current temperature of surface in K, $T_{ambient}$ is 298.15 K, η is the kinematic viscosity of air at 25 °C (1.568×10^{-5} Pa s) and α is the thermal diffusivity of air at 25 °C (19×10^{-6} $m^2\ s^{-1}$).

For $Ra_L < 10^9$ ($\because O(l_c) = O(w) = 10^{-6}$ m) and constant heat flux out of a vertical plate,

$$\therefore Nu = 0.68 + \frac{0.67 Ra^{1/4}}{\left[1 + \left(\frac{0.492}{Pr}\right)^{9/16}\right]^{4/9}}. \tag{3.7}$$

For $Gr_L Pr < 2 \times 10^8$ and constant heat flux out of a horizontal plate (heated side up),

$$\therefore Nu = 0.13 (Gr_L Pr)^{1/3} = 0.13\, Ra_L^{1/3}. \tag{3.8}$$

$$h = \frac{Nu.k}{L_c}. \tag{3.9}$$

where k is the thermal conductivity of air at 25 °C (26.38×10^{-3} $W\ m^{-1}\ K^{-1}$).

3.4.3 Mechanical deformation performance

After optimising the heating performance through the pangolin-inspired conductive scales, we verified the mechanical deformation performance of the overall soft robot to observe the effect of the scales on its locomotion. In this regard, the tests studied the response of the magnetic composite after addition of the metal scales. In the first series of experiments, the flexural compliance of the structure was examined by performing a three-point bending test on the hybrid robot in various configurations and percentage overlaps (**Figure 3.11A**). In this work, intrados is defined as the configuration where the scales are facing up and extrados for the converse, where the scales are facing down. This would allow us to estimate the forces required to bend the composite structure and hence the strength of the external magnetic fields required to actuate the robot.

The test method was adapted from the D7264 ASTM (American Society for Testing and Materials) standard. In this regard, a 20 mm × 10 mm × 0.2 mm sample was tested on a micro 3 point bending test fixture (2810-411, Instron) of an Instron machine (5942, Instron) with the 5 or 10 N load cell, depending on the maximum load. The supporting pins were positioned 10 mm apart and the samples were loaded at a rate of 20 μm s^{-1}. Stresses and strains were computed based on methods proposed in the standard. For the overlapping structures, the average height was used. The average height was defined as the height of the centre of the scale (**Figure 3.11B**). Three samples were tested once each. The flexural chord modulus was calculated from the linear region of the stress-strain graph. This value of the linear region ranged between 0.003 and 0.01 strain depending on the samples. The reported values are the engineering stresses and strains.

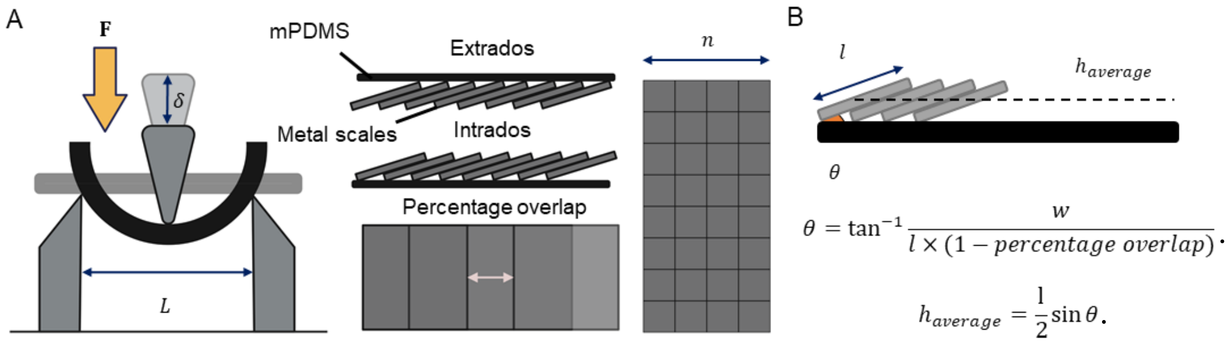

Figure 3.11: Characterisation of mechanical performance. (A) Schematic of experimental setup. Figure created with biorender.com. (B) Calculation of the average height for calculation of the stress and strain for overlapping scales.

First, the effects of the scale size were studied. Non-overlapping samples of different scale lengths were fabricated from a 50 µm-thick aluminium sheet. Once the scaled structures were introduced, the maximum stress experienced during the three-point bending test decreased by 87.9% from 8.3 MPa to 1 MPa (**Figure 3.12A**). This brought the stress levels to an order that was comparable to the maximum stress experienced (0.18 MPa) by the magnetic polymer without any scales (mPDMS), highlighting the mechanical advantage of adding scales to the structure. As the length of the scales decreased from 5 mm to 1 mm, the maximum stress was further reduced to 0.68 MPa, a value only 3.7 times larger than mPDMS. This maximum stress was even lower for overlapping structures, dropping by an additional 85%, from 1.0 MPa to 0.15 MPa for the structures with 0% and 75% overlap, respectively (**Figure 3.12B**). At 0.15 MPa, this meant that the structure was equally easy to deform as the mPDMS. Similar to how individual pangolin scales were directly connected to the soft skin layer and not interconnected [108], the scales on the robot were directly bonded to the magnetic polymer and were not bonded to each other. As such, the area directly bonded to the magnetic polymer decreased at increasing percentage overlaps. The scale, at increasing percentage overlaps, constrained less of the polymer and made the mechanical bending behaviour closer to that of the unscaled structures. In contrast, for the design with no overlap, the whole plate still rests on the surface of the soft magnetic polymer matrix. As such, the only way that the maximum stress could be decreased was to decrease the size of the scales.

As we were concerned about the load vs. deflection behaviour before and after addition of the scales, the flexural chord modulus of elasticity of the structure (E_{FC}) was calculated. A lower modulus of elasticity value was desired as it would mean that a lower force had to be applied to the structure per unit of deformation. As the length of the scales decreased from 5 mm to 1 mm, the modulus of elasticity dropped from 31.7 MPa to 19.5 MPa. For comparison, the values for mPDMS and the structure without any scales were 9.3 MPa and 583.7 MPa, respectively. As such, this meant that increasing the externally applied fields was a viable method to actuate these robots – it required at most three times more force per unit of deformation. We also characterised the effects of using different materials or thicknesses on E_{FC}. In this regard, we observed that E_{FC} was predominantly a geometrical property. Unscaled samples made from other materials differed at least one or two orders of magnitude in E_{FC} as compared to mPDMS. However, this value dropped to the same order of magnitude once the scales were added. The same trends were also observed even when the thickness of the material was changed (**Figure 3.12C**).

Finally, we looked at the flexural compliance of the overlapping scaled robot in various configurations and orientations. Apart from the intrados test configuration, similar trends were also observed for the other test configurations (i.e., significant drop in maximum stress and E_{FC}). Moreover, E_{FC} of the overlapping scaled robot in a transverse configuration, as denoted by the gradient of the stress-strain graphs, was comparable to the value of the scaled robot with no overlap tested in a longitudinal configuration (**Figure 3.12D**). Regardless of the overlapping scales in the longitudinal direction, the robot had a non-overlapping configuration in the transverse direction which gave rise to a similar E_{FC}. We also note that the intrados configuration had similar levels of E_{FC} as compared to the uncut scale (246.5 MPa vs. 583.7 MPa). Although not exploited in this work, such a capability could potentially allow the robot to lift or support large loads, whilst still remaining deformable enough for magnetic actuation-based shape programming.

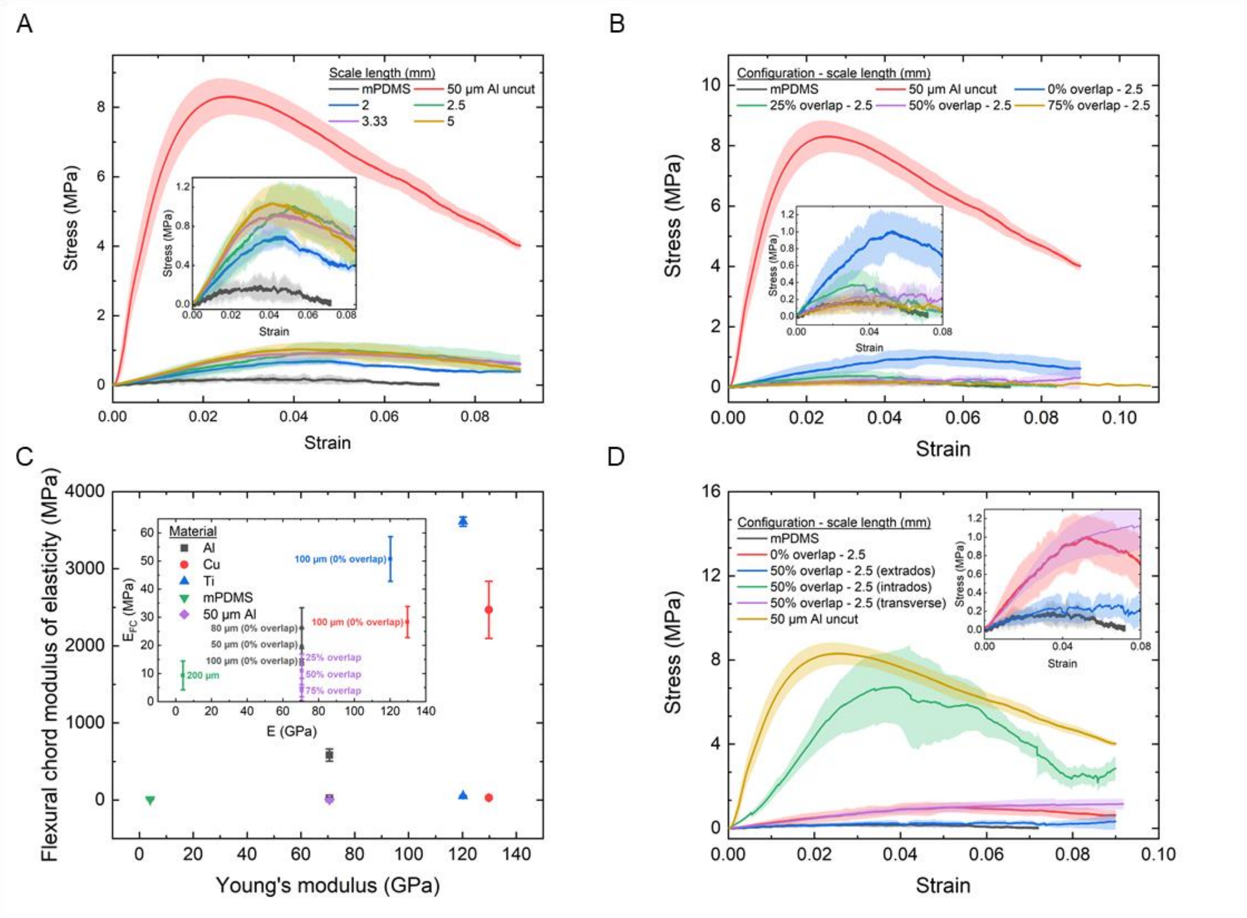

Figure 3.12: Stress-strain characteristics of composite structure. (A) Stress-strain curve for a 20 x 10 x 0.25 mm sample with different scale lengths (n = 3). Error bars represent the standard deviation. (B) Stress-strain curve for a 20 mm × 10 mm × 0.2 mm sample bonded to 0.05 mm aluminium with different percentage overlaps (n = 3). Error bars represent the standard deviation. (C) Comparison of the flexural chord modulus of elasticity (E_{FC}) for different materials and thicknesses (n = 3). Error bars represent the standard deviation. (D) Stress-strain curve for a 20 mm × 10 mm × 0.2 mm sample bonded to 0.05 mm aluminium at 50% overlap with different test configurations (n = 3). Error bars represent the standard deviation.

The second set of characterisation experiments focused on the bending response of the magnetic composite after addition of the scales. In this regard, the angle between the tip and the fixed support when subjected to different external magnetic fields was compared. Anti-clockwise angles were defined as positive in this work (**Figure 3.13A**). Similar to the flexural tests performed earlier, the tests focused on the effects of the scale length, overlap and material selection on the bending angles. To characterise the deformation of the magnetic polymer with scales, the robot was placed in a uniform magnetic field generated by a Halbach array. The robot was fixed on one end by clamping with a pair of flat tweezers while the other end of the robot was free to deflect. The angle between the tip and the fixed support was analysed in ImageJ. Three samples were tested once each.

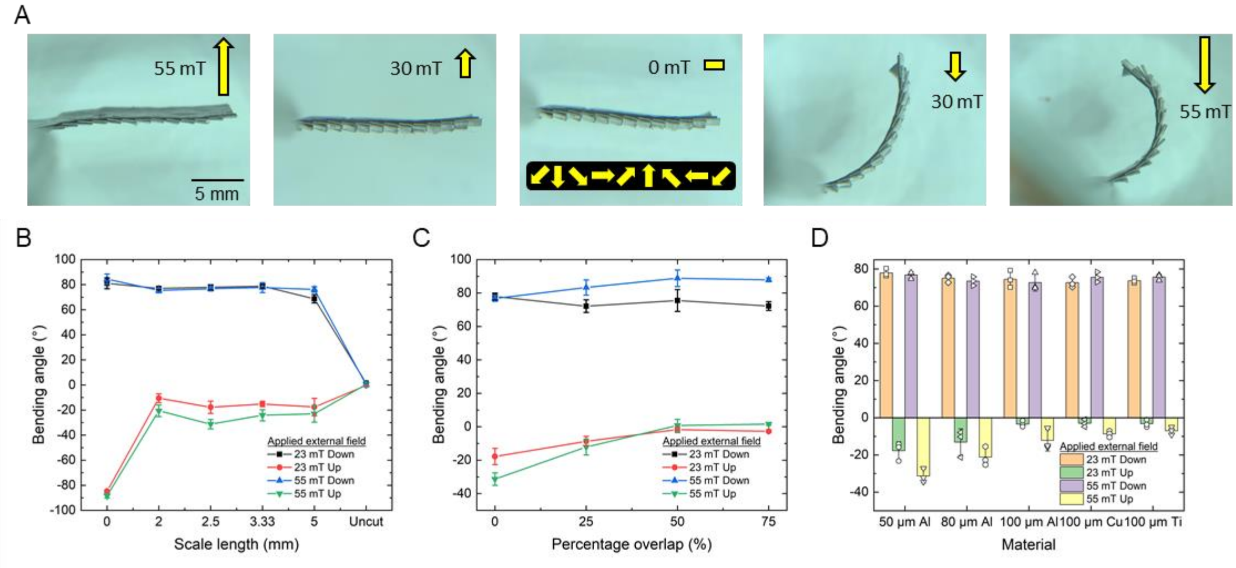

Figure 3.13: Bending performance of composite structure. (A) Deflection of a 20 mm × 10 mm × 0.2 mm sample bonded to 0.1 mm Al at 50% overlap at different applied external magnetic fields. Inset shows the magnetisation profile of the robot. (B) Deflection angles for a 20 mm × 10 mm × 0.25 mm sample with different scale lengths (n = 3). Error bars represent the standard deviation. (C) Deflection angles for a 20 mm × 10 mm × 0.2 mm sample bonded to 0.05 mm aluminium with different percentage overlaps (n = 3). Error bars represent the standard deviation. (D) Comparison of the deflection angles for different materials and thicknesses. Error bars represent the standard deviation.

First, we looked at the bending angles of the robot after the scales have been introduced. Similar to the experiments for flexural compliance, the same trends and observations for the scaled and overlapping samples were obtained. In this regard, it was observed that once the scales were added, the robot was able to achieve similar levels of deflection as the mPDMS (**Figure 3.13B**). Although there was a slight decrease in the anti-clockwise deformation (81° vs 76°), this deformation angle was noted to be insensitive to the strength of the externally applied magnetic field tested (23 mT and 55 mT). However, the robot's deflection in the direction of the scales was compromised and the robot was unable to reach the original levels of deflection. Deflection in the direction of the scales would cause the plates to come into contact with each other and as such, limit the maximum deflection. The same trends were also observed in the overlapping samples (**Figure 3.13C**). Finally, we looked at the deflection angles with respect to different materials and found that the deflection angles are predominantly a geometric property and are independent of the material properties. When the thickness of the scale was reduced, an increase in the anti-clockwise deflection was noted. For a thinner scale, the magnetic PDMS would be free to deflect more before the scales come into each other (**Figure 3.13D**). The experimental results were also consistent with the simulation results obtained in COMSOL (**Figure 3.14**).

In summary, we found that the pangolin-inspired overlap structures offered the best mechanical compliance, even matching the mPDMS at 75% overlap. Similar to the animals found in nature, we find that a higher degree of overlap offers better mechanical compliance. Scales found on African tree pangolins, have a higher overlapping ratio and as such, are more flexible and can perform a larger range of motion which might be necessary for survival in their habitat. In contrast, Chinese pangolins have a lower overlapping ratio and mainly live in burrows on the ground [108], [120], [121]. This means that the overlapping design could potentially allow a larger scale for better heating to be used without compromising the mechanical compliance.

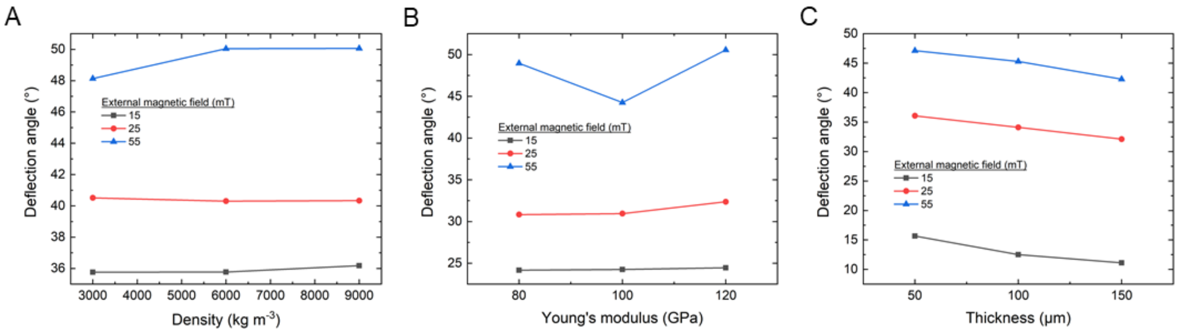

Figure 3.14: Simulated deflection angles in COMSOL showing that the deflection angles are independent of the identified material properties. (A) Simulated deflection angles at different densities for a scale length of 2.5 mm of thickness 50 µm at a constant Young's modulus of 80 GPa. (B) Simulated deflection angles at different Young's moduli for a scale length of 2.5 mm of thickness 50 µm at a constant density of 6000 kg m^{-3}. (C) Simulated deflection angles at different thicknesses for a scale length of 2.5 mm at a constant density of 6000 kg m^{-3} and constant Young's modulus of 100 GPa.

3.5 Multifunctional robotic capabilities

Finally, we demonstrate the capability of such robots based on active locomotion with magnetic actuation coupled with on-demand functionalities enabled by the addition of the heating scales. The functionalities shown in this work can be broken down into two main categories. The heat could be used to change certain properties of the robot on demand and then harnessed to achieve new functions, such as selective cargo release and in situ demagnetisation. Alternatively, the heat produced could potentially be directly used by untethered robots to perform medical treatments involving heat, such as hyperthermia for cancer treatment or to mitigate bleeding in hard-to-reach regions.

Aluminium was selected as the material for the subsequent demonstrations because it had a high electrical conductivity, allowing the thickness of the scale to be decreased. This, coupled with the low density and the non-ferromagnetic nature of aluminium, meant that it would be easier to actuate the robot and would also eliminate any possibility of the material interfering with magnetic actuation. The pull-out force of the aluminium scale on mPDMS was experimentally determined to be approximately 800 mN, implying that the scales are unlikely to fall off during actuation (**Figure 3.15**). With this, we demonstrated how an untethered robot comprising 100 µm aluminium scales with 50% overlap was able to actuate and move in a stomach phantom with a 65 mT rotating magnetic field even with a non-optimal configuration for heating and locomotion.

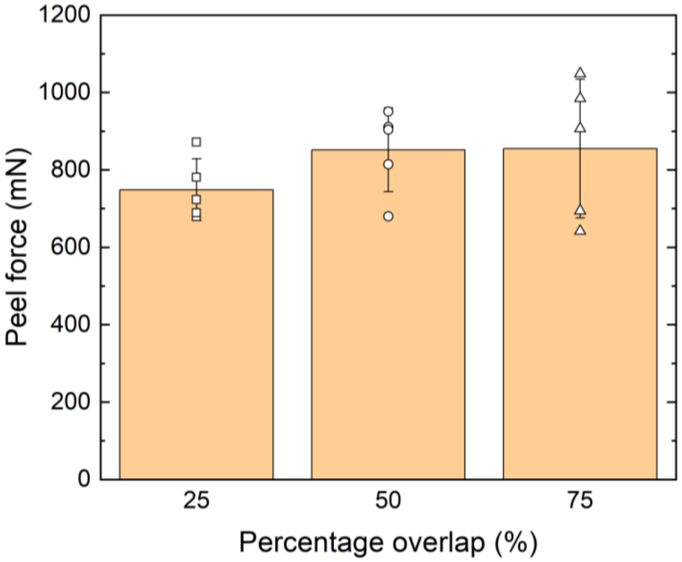

Figure 3.15. Pull-out force of a 100 µm-thick aluminium scale from mPDMS at different percentage overlaps (n = 5). Error bars represent the standard deviation.

In the first category, we demonstrate a version of an untethered magnetic robot that can perform on-demand in situ demagnetisation, a function enabled by the heating scales. In this demo, a robot with non-overlapping 50 µm aluminium scales was used to enable in situ demagnetisation, thereby allowing for the magnetisation profile on the robot to be changed in situ. Non-overlapping scales were used to ensure even heating of the magnetic polymer. In the first phase, the robot employed a rolling strategy for locomotion because it had a pre-programmed sinusoidal magnetisation profile imparted to it prior to deployment. After reaching the target location, the robot was exposed to the RF field. In doing so, the scales and the magnetic polymer were heated to temperatures above 219 °C. As this was above the Curie temperature of the magnetic particles (MQFP-10-8.5HD-20180, Magnequench) embedded in the soft matrix, the particles shifted to a paramagnetic state and the magnetisation profile previously encoded was lost. After in situ demagnetisation, the robot was observed to be unresponsive to any input magnetic fields, indicating that the robot no longer had any magnetisation profiles (**Figure 3.16A**). This was also confirmed separately when the magnetic flux density on the robot was measured (**Figure 3.16C**). Only after subsequent magnetisation with a uniform 1.8 T external magnetic field was the robot able to locomote again. The temperature required and magnetisation field could be lowered even further if magnetic particles with a lower coercivity and Curie temperature are used. Due to the difference in the magnetisation profile, the robot now utilised tumbling rather than rolling for locomotion (**Figure 3.16B**). Such system could enable in situ change of the robot's magnetisation profile, which could enhance the functionalities of these robots. Specifically, miniature magnetic soft robots reported in literature to date have a fixed magnetisation profile which, after deployment, cannot be changed in situ. As such, the response of the robot to an external magnetic field cannot be changed after it is deployed. Although reprogrammability by heating above the Curie temperature had been demonstrated previously [122], this process was not in situ and a laser was used to locally heat up the polymer. This process allowed very precise programming of the magnetisation profile, yet had limited use in biomedical applications inside the human body as the laser required line of sight for heating. As such, this demonstration highlights the ability of this method to allow these untethered robots to potentially change its magnetisation profile on the fly. This further opens up the design space and enhances the performance of untethered miniature robots, since a single robot design can now potentially change and adapt its locomotion based on the environment accordingly in situ. Moreover, the demagnetised robot is unresponsive to the actuating fields. As such, through judicious placement of the heating plates, demagnetisation of those parts could enable selective actuation of the robot for specific tasks after the robot has navigated to the target location. Alternatively, this demagnetisation feature could allow for better control of robotic swarms. For instance, untethered robots can be deployed singularly and then deactivated, thereby allowing another robot to be deployed to the same region without the concern that the actuating fields for the second robot would unintentionally actuate the first as well.

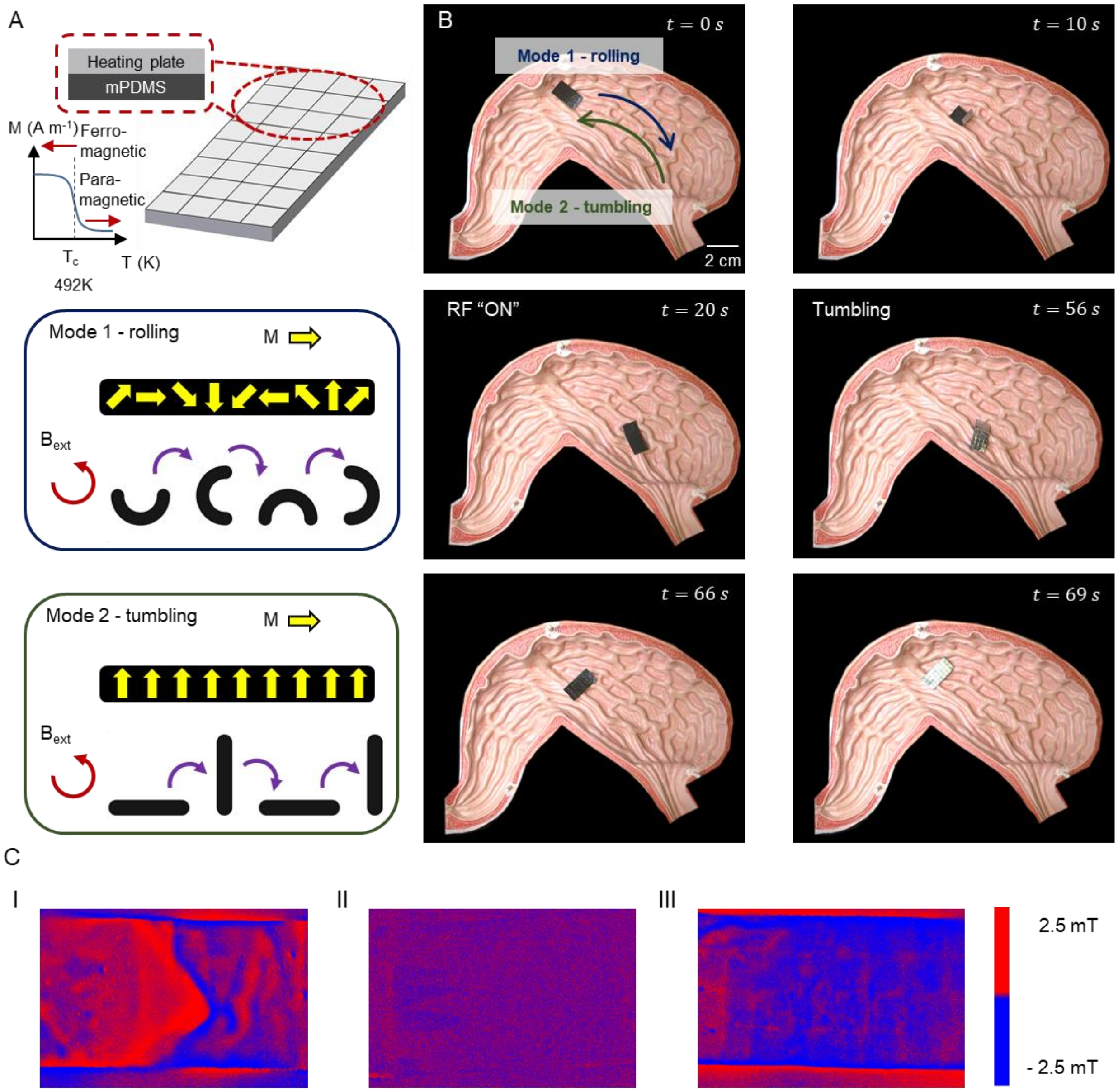

Figure 3.16: Enhanced functionalities of untethered miniature robots. (A) Schematic of the untethered magnetic robot which can perform in situ demagnetisation to switch the locomotion modes from Mode 1 – rolling to Mode 2 – tumbling. Inset shows the magnetisation profiles and the response of the robot to an externally applied magnetic field. Figure created with biorender.com. (B) Deployment of the robot in a stomach phantom. (C) Imaging of the magnetic fields generated by the soft magnetic polymer at various stages of actuation. (I) Before RF heating. (II) After RF heating. (III) After remagnetisation. Outlines of the heating plates can be seen.

Next, we demonstrate how the heating scales can enable selective on-demand cargo release. Magnetic miniature robots typically operate at a distance from the magnetic actuation coils. This, combined with their small size, imply that the robots perceive the external magnetic field as a homogenous field. As a result, a single robot can only have a monotonic response to the externally applied magnetic field. In this variant of the robot, we exploited the different heating rates of the scales to enable selective cargo release. The cargo was secured to the robot with beeswax, which had a melting point of 61 °C to 65 °C. A 50 µm and 80 µm aluminium scale was placed under the green and blue cargo, respectively, to heat up the beeswax (**Figure 3.18A**). When exposed to the RF field, the 80 µm-thick aluminium scale was able to reach the targeted temperature approximately 1 s faster than the 50 µm-thick aluminium scale (**Figure 3.17**). This allowed the robot to only release the blue cargo but not the green cargo (**Figure 3.18B**). It is important to note that the temperature required was slightly higher than the melting point of beeswax as the addition of beeswax increased the thermal load. Such a feature could not be easily integrated with other heating methods, such as those involving Joule heating (i.e., liquid metal droplets could be mixed in the polymer matrix) because the heating occurred homogenously throughout the liquid metal droplets dispersed inside the robot. The main limitation of this robot design lies in the selection of

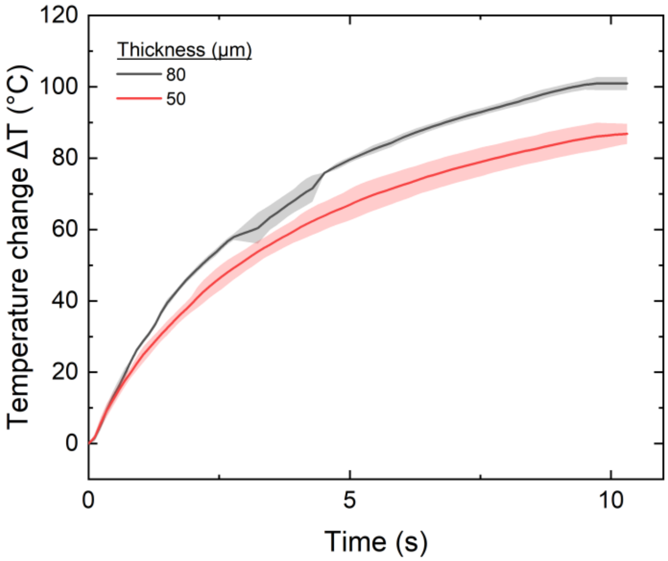

Figure 3.17: Heating performance of a square 2.5 mm aluminium plate of different thicknesses placed 3 cm away from the RF coil (n = 3). Error bars represent the standard deviation.

adhesive to secure the cargo to the robot. Although the beeswax used in this demonstration is biocompatible and can be safely ingested, the beeswax re-solidifies upon cooling. This does not pose a problem in this work because we intend to deploy the robot in the GI tract, where the wax can be safely excreted by the human body. However, to further extend the clinical utility of these robots, studies should be conducted to identify adhesives which thermally degrade upon heating into compounds which can be safely excreted or absorbed by the body. On a related note, any functionality requiring heat activation could also be implemented. For instance, with the addition of thermal adhesives on the heating scales, we were also able to show that the magnetic robot was able to adhere to P100 grade sandpaper which has an average particle diameter of 162 μm.

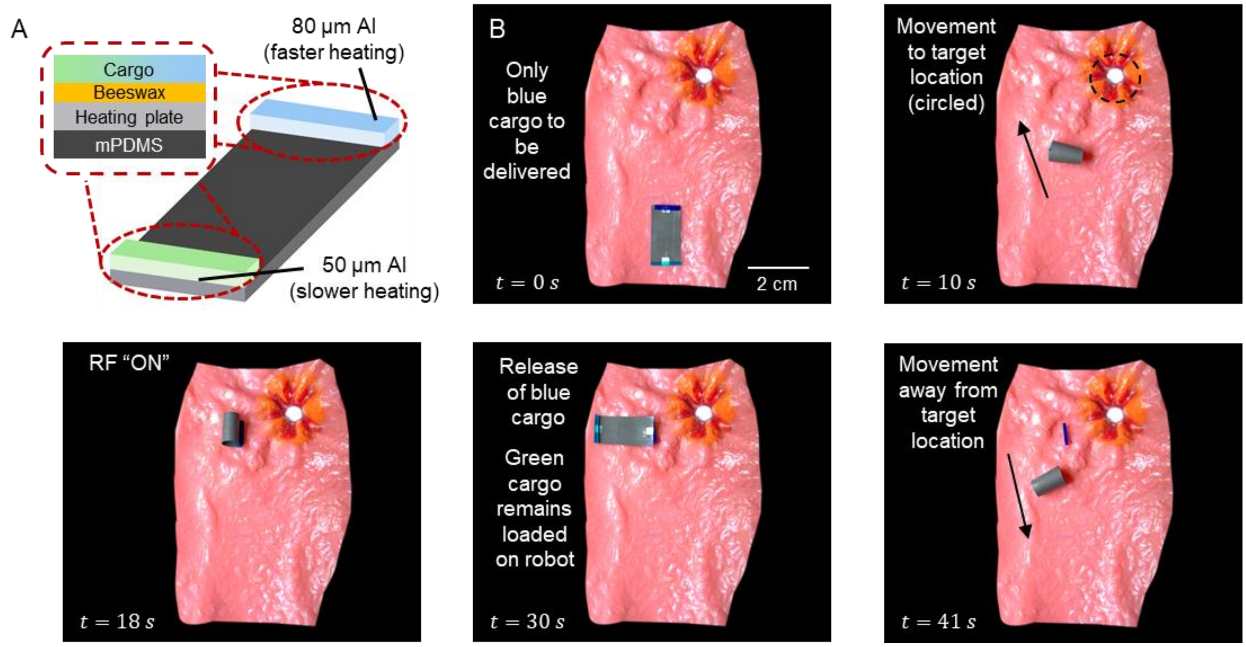

Figure 3.18: Enhanced functionalities of untethered miniature robots. (A) Schematic of the untethered magnetic robot which can perform selective cargo release. The selective cargo release is enabled by exploiting the different heating rates of materials with different thickness. It can also be enabled by using different materials. Figure created with biorender.com. (B) Deployment of the robot in a tissue phantom.

3.6 Untethered heating robots towards medical applications

In the latter category, we demonstrate how the heat could be used directly to perform medical treatments in the gastrointestinal tract. First, we showed how a robot with 50 µm-thick aluminium scales with 50% overlap could be easily incorporated into a standard size “0” gelatine capsule for oral deployment. Using such a method allows us to non-invasively deploy these robots in tortuous hard-to-reach regions, such as the small intestines, which are difficult to access using established techniques, such as endoscopy or colonoscopy. Moreover, to account for the highly heterogeneous environments inside the body, simulations were performed to determine the heating performance of the scales across different distances and convective heat transfer coefficients. This would provide insights on the heating performance of the robot under more realistic conditions. Based on the additional simulations performed (**Figure 3.19**), we observed that for a similar decrease in heating performance (i.e. final temperature of the metal scale after 60 s of RF exposure), the distance from the coil had to be increased by 3 times while the convective heat transfer coefficient had to be increased by 1000 times for a given RF input. This implies that the heating performance is more sensitive to changes in the magnetic flux (i.e., distance) as opposed to changes in heat losses (i.e., environmental conditions).

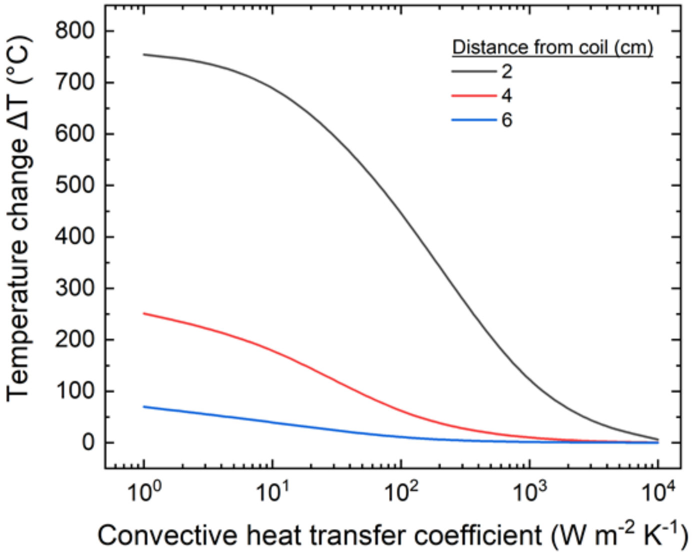

Figure 3.19: Simulated temperatures of a 100 µm aluminium scale at t = 60 s at different convective heat transfer coefficients and distances from the RF coil.

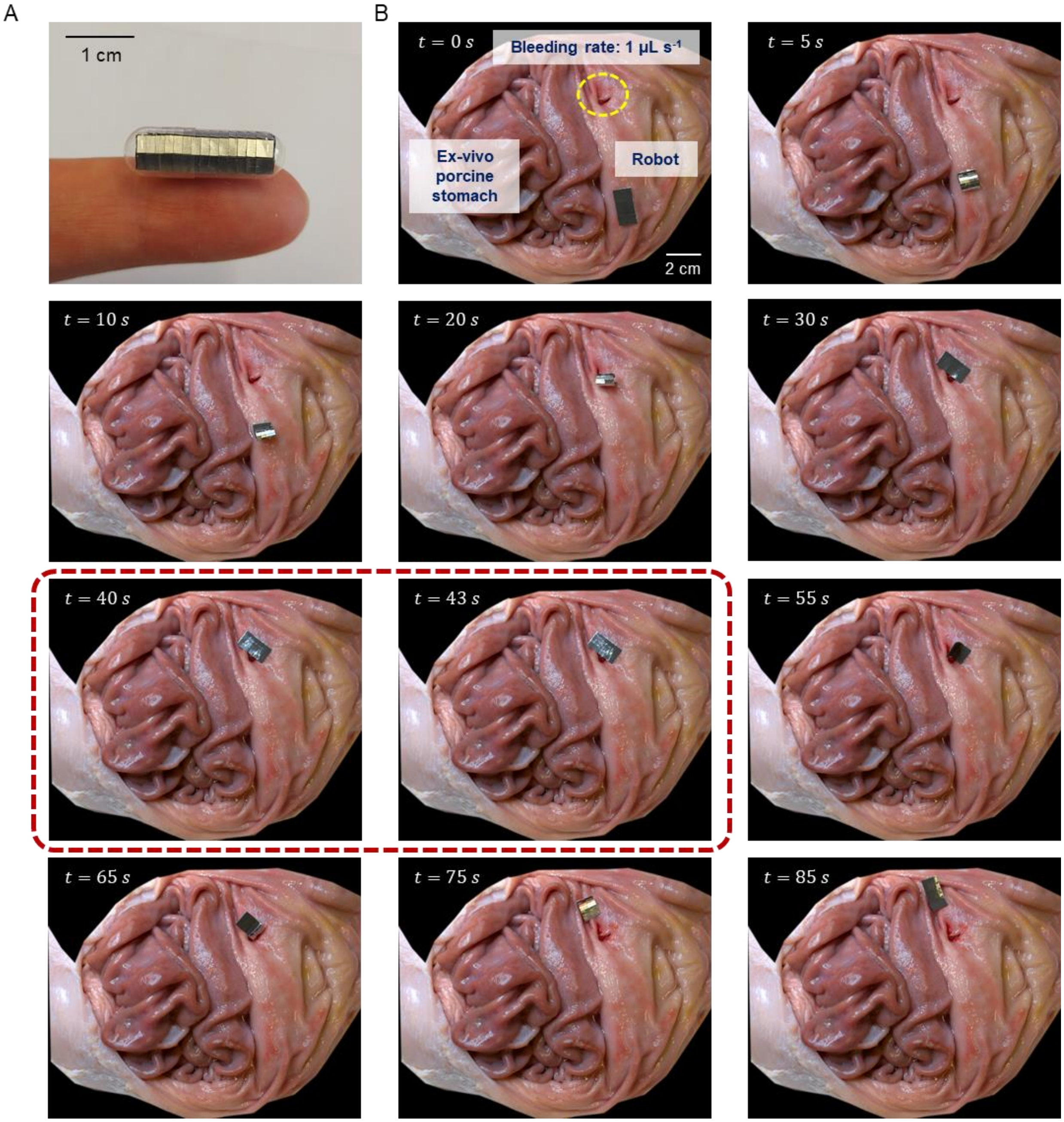

Figure 3.20: Ex vivo demonstration directly utilising heat energy to mitigate blood loss. (A) A 20 mm × 10 mm × 0.2 mm robot with 50 µm aluminium scales at 50% overlap inside a standard size "0" gelatine capsule (21.2 mm × 7.3 mm). (B) The integrated robot moves to the target location inside an ex vivo porcine stomach. Upon application of a 3 s RF pulse (frames circled in red), no more bleeding at the site was observed.

To demonstrate the potential clinical utility of such a robot (**Figure 3.20A)**, we simulated bleeding inside an ex vivo porcine stomach. The bleeding rate was set at 1 μL s^{-1}, to mimic capillary flow rates in the GI mucosa [123]. The robot was able to navigate to the bleeding site and upon application of a 3 s RF pulse, stop the bleeding at the site (**Figure 3.20B**). Although this demonstration was conducted in stomach, this robot could potentially be deployed in other parts of the GI tract as well. This robot design could be an enabling technology for the treatment of GI bleeding in hard-to-reach sites. One such example would be bleeding in the small intestine, which accounts for almost 5% of the GI bleeding, but remains challenging to diagnose and treat with conventional treatment methods [124]. Such an untethered robot could also offer clinicians with a less invasive alternative for elective procedures for small intestinal bleeding with various etiologies (i.e., ulcers, angiodysplasias, polyps or tumours) especially when coupled with medical imaging feedback. For this reason, we also explored how the robot is compatible with existing medical imaging modalities, such as ultrasound imaging (**Figure 3.21A**). Such a capability could

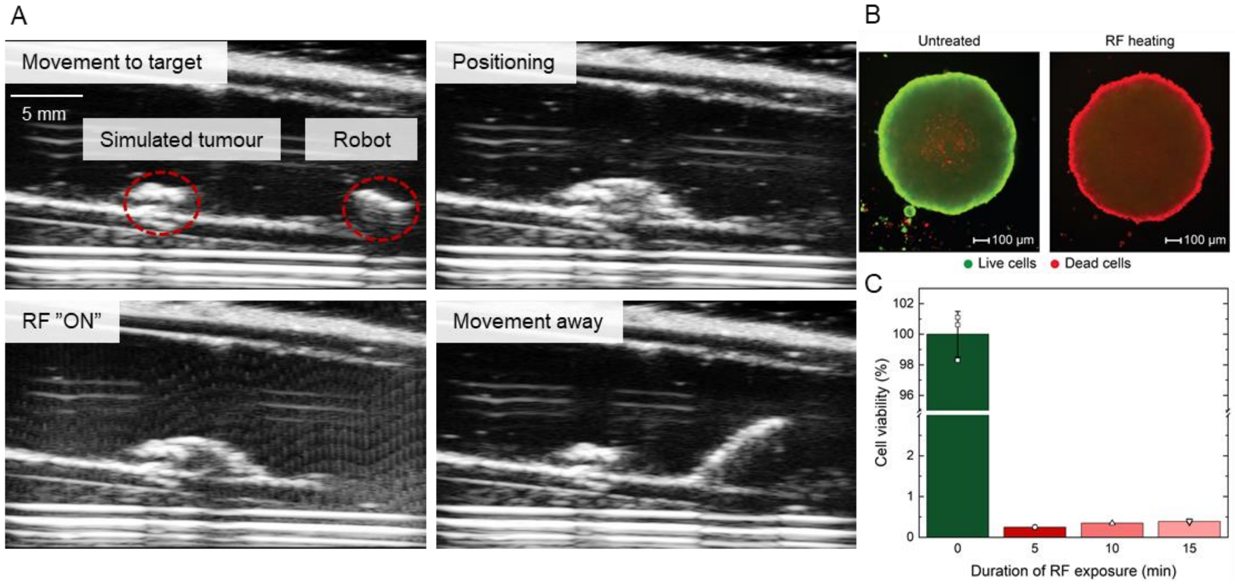

Figure 3.21: Ex vivo demonstration directly utilising heat energy for hyperthermia. (A) Ultrasound guided robot operating inside an ex vivo porcine small intestine with a simulated tumour. Small intestine is filled with DI water. (B) Representative fluorescence images of RF exposed HT-29 tumour spheroids stained with calcein-AM/ethidium homodimer-1 after 24 h of incubation. (C) Viability of HT-29 tumour spheroids after different durations of RF exposure (n = 3). Three spheroids were independently tested once for the experiments. Error bars represent the standard deviation.

also enable novel non-invasive treatments, such as hyperthermia for the treatment of cancer [125]. In this regard, we subjected tumour spheroids in direct contact with the heating scales to the RF field and observed that the tumour spheroids were destroyed after just 5 min of heating at 60 °C (**Figure 3.21B, C**).

Moreover, the safety of deploying these robots inside the human body can be further enhanced by adding fillets to the scales to reduce the likelihood of tissue puncture, without adversely affecting the overall heating performance (**Figure 3.22**).

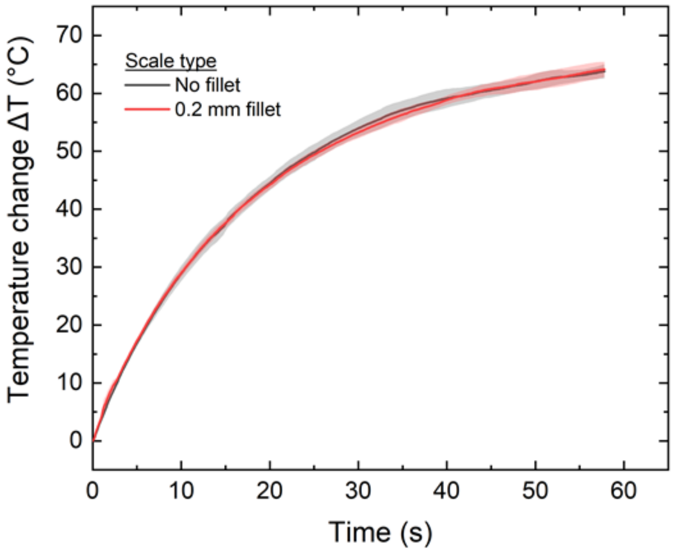

Figure 3.22: Heating performance of 16 non-overlapping 2.5 mm square 100 µm-thick aluminium scales with 0.2 mm fillets as compared to another with identical dimensions without fillets (n = 6). Error bars represent the standard deviation.

3.7 Preliminary biocompatibility tests

Results from an initial biocompatibility test are presented here. Biocompatibility assays were performed on (i) 1 cm × 1 cm aluminium squares with a thickness of 100 µm and (ii) different concentrations of aluminium powder. BJ fibroblasts, CRL-2522, were seeded on the top of 1 cm × 1 cm aluminium substrates and the viability of cells after 72 h of incubation was analysed. After 72 h of incubation, the fibroblasts were stained with a Live/Dead Cell Imaging Kit (Invitrogen) according to the supplier's instructions. Images of living (Ex/Em: 488/520 nm) and dead (Ex/Em: 528/617 nm) cells were obtained using a fluorescent microscope (Nikon Eclipse Ti-E). After 72 h of culture, the fibroblasts demonstrated clear viability in the culture environment with spindle-shaped, healthy morphology at the interface of the metal (**Figure 3.23A**).

The human skin fibroblast cells, CRL-2522, were seeded in a black/clear bottom 96-well plate (Corning) at a concentration of 1 × 10^4 cells per well the day before the experiment to allow for the attachment of cells. After 24 h of incubation, the cells were treated with different concentrations of aluminium powder (37.5 µg mL^{-1}, 75 µg mL^{-1}, 150 µg mL^{-1}, 300 µg mL^{-1}, 600 µg mL^{-1} and 1200 µg mL^{-1} in DMEM) in triplicates for 24 h and 72 h. After incubating for the

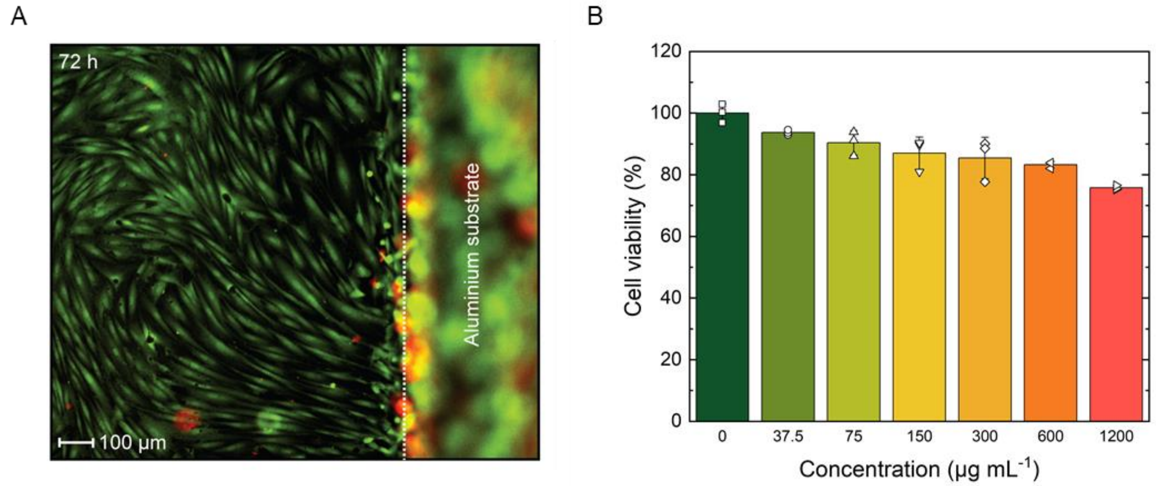

Figure 3.23: Results from the initial biocompatibility tests. (A) Live-dead staining of fibroblast cells cultured with the aluminium scale. The cells were viable after 72 h of culture and displayed healthy morphology even at the interface of the scale. (B) Cell viability as a function of aluminium powder concentration after 72 h of treatment, based on adenosine triphosphate (ATP) production. The cells showed more than 85% viability even at relatively high concentrations over 3 independent samples (n = 3). Error bars represent the standard deviation.

given periods, the cellular viabilities of BJ fibroblasts were measured using the CellTiter-Glo assay (Promega) (61). The luminescence values were measured in an opaque 96-well plate using a plate reader (BioTek's Synergy 2, Winooski, VT, USA). The viabilities of treated fibroblasts with different concentrations of aluminium powder were expressed as a percentage of the untreated fibroblasts, which was taken to be 100%. The cell viability analysis showed that the aluminium powder (up to the concentration of 600 µg mL^{-1}) did not cause any adverse effect on the cells after 72 h (**Figure 3.23B**).

To test the stability of aluminium in various fluids in the GI tract over 48 h, 1 cm^2 aluminium scale of 100 µm thickness was submerged in 2 mL of simulated gastric fluid (3082.1000, Th. Geyer), intestinal fluid (D020-00, Th. Geyer) and high-glucose Dulbecco's Modified Eagle Medium (DMEM, Gibco). The absorbance of the solutions was measured with a plate reader (Infinite M Plex, Tecan) at 300 nm. No observable degradation occurred for the samples submerged in intestinal fluid and DMEM. The aluminium scale submerged in simulated gastric fluid dissolved after 48 h. The absorbance of the resultant solution was 0.367 which corresponded to a concentration of 533.6 µg mL^{-1} (**Figure 3.24**). This preliminary data indicates that even if the aluminium scale dissolves, the concentration does not adversely affect cell viability.

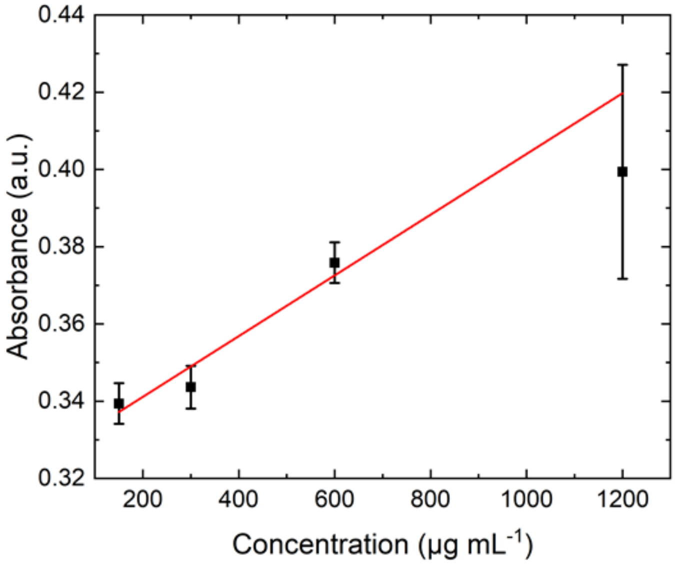

Figure 3.24: Absorbance calibration curve for aluminium powder of varying concentrations suspended in simulated gastric fluid at 300 nm. 3 independent samples were tested once each (n = 3). Red line indicates the line of best fit. Error bars represent the standard deviation.

3.8 Summary

In this work, we introduced a design to enable heating over long distances for untethered miniature robots. Inspired by pangolins found in nature, the scaled design introduced in this work allowed for two different competing requirements, namely the compliance and heating performance, to be concurrently realised on a single untethered robot. Although hierarchical structures have been implemented in literature primarily for their mechanical properties, we find that implementing the overlapping structures found in pangolins is also advantageous to remote heating. This allowed us to achieve significant heating on demand (ΔT > 70 °C) at large distances (> 5 cm) within a short period of time (< 30 s) without sacrificing on the bending compliance of the robot. Guidelines to optimise the heating performance and bending compliance were established. Most importantly, the mechanism was small and light enough to be mounted on existing magnetic soft millirobots. Enabled by the remote heating capabilities of the design in tandem with locomotion, integrated robots displaying advanced robotic functionalities such as in situ demagnetisation and selective cargo release were demonstrated. Initial steps for untethered robots targeting potential biomedical applications, such as mitigation of bleeding and hyperthermia were also demonstrated. These functionalities highlight the possibility of using such untethered robots in medical applications.

For successful translation, future studies should concentrate on four technical aspects on top of application specific issues, such as how residual intestinal content might still be present after flushing of the GI tract and how it may interfere with locomotion. Firstly, since both actuation and remote heating involve magnetic fields, future work should look into the possibility of creating a magnetic system in which both the high and low-frequency fields can be given with a single magnetic actuation setup. Doing so would significantly reduce the time and effort required to operate such a robot, while allowing for more accurate control of the magnetic fields. This would then allow true in situ reprogramming of the magnetisation profile to be achieved (i.e., both demagnetisation and magnetisation). Secondly, the heating efficiencies of RF fields could potentially be further increased by exploiting secondary effects, such as the proximity effect or through the addition of insulating layers such as Parylene C on the sides of the scales. This would generate more heat and further extend the operating range of the robot. Thirdly, regarding the safety of biological tissues to such an RF exposure, a maximum current of 621.6 A at 338 kHz was applied by the RF heater positioned 5 cm away for up to 15 min in all ex vivo demonstrations.

This translates to a magnetic field intensity of 34.6 kA m^{-1} and is comparable to the levels of RF that is being applied in in vivo experiments or clinical trials currently (**Table 3.2**). Although this highlights the potential of using such devices in a clinical context, in vivo tests should still be conducted to definitively conclude the safety of such an exposure and also the upper limit of exposure. A higher current would generate more heat for other applications, further extend the operating range of the robot or reduce the duration of RF exposure. Lastly, the use of better materials in terms of biocompatibility and biodegradability should be investigated. An example would be Dermabond, which is currently used in clinics for topical wound closures and hence, could potentially provide the necessary adhesion of the scales to mPDMS whilst simultaneously offering better biocompatibility. Further studies will have to be conducted to assess the suitability of this adhesive for applications inside the body as the working environment inside the human body varies greatly from the outside. Biocompatible and biodegradable materials such as FePt and hydrogels as substitutes for mPDMS should also be considered. Addressing these issues would further enhance the capabilities of the untethered robot and can potentially unlock a new range of minimally invasive long-term medical procedures, which are currently unavailable.

Table 3.2: Comparison of the RF fields applied in vivo in literature.

Study type	Frequency (kHz)	Maximum magnetic field intensity (kA/m)	Duration (min)	Reference
In vitro	118	30.6	30	[126]
Rats	118	30.6	30	[127]
Rats	118	30.6	30	[128]
Rats	118	30.6	30	[129]
Rats	100	18	40	[130]
Rats	150	11	20	[131]
Clinical trial	100	18	60	[132]
Clinical trial	100	15	60	[133]
Clinical trial	100	18	60	[134]
Clinical trial	100	18	60	[102]
This work	338	34.6	15	-

Chapter 4: Untethered electrical magnetic robot for on-demand multi-functional biomedical applications

4.1 Background

Untethered miniature robots can access regions deep inside the human body and as such, hold great potential in minimally invasive biomedical applications [36], [37]. Magnetic actuation, in particular, has emerged as a popular mode of actuation for these robots as magnetic fields can safely penetrate human tissues without significant attenuation and can be precisely controlled [35], [135]. Recent developments in this field have further increased the functionalities of these robots, equipping them with capabilities ranging from temperature-adaptive locomotion [89], [90], tubular anchoring [20], tissue penetration [65], to even remote heating [136]. Even so, these robots cannot be readily adapted for a variety of tasks because the designs are optimised for converting magnetic energy to its final form, such as strain or heat energy. Subsequent conversions of energy are usually avoided as it results in more losses. A more versatile form of energy which can be readily converted to other forms of energy to accomplish tasks would, therefore, further extend the capabilities and versatility of these robots and push them another step closer to the bedside.

Electricity is one such form of energy which can be readily converted to other forms of energy and has the added advantage of having a large variety of accompanying hardware for customisation. Although electricity is a desirable form of energy for untethered miniature robots to possess and there exists extensive research in using alternating magnetic fields to wirelessly transmit power, few untethered robotic systems developed to date possess such a capability. Lu et al. [15] proposed a method exploiting magneto-electric effects to generate power. However, as the robot depends on the piezoelectric layer for voltage generation, the robot is restricted to increasing the thickness or area of the piezoelectric layer to increase the power harvested from the robot [137]. This could result in stiff and bulky structures, impeding locomotion of the robots. On the other hand, Zhang et al. [25] proposed a liquid metal-elastomer composite exploiting near-field inductive coupling for wireless power transfer. However, because of the low electrical conductivities of the composite, the robot had to be placed on the surface of the magnetic coil, making it impractical to deploy the robot in real-life scenarios. Only wireless power transfer with magnetic fields is considered because wireless power transmission with light or acoustics can only reach peripheral regions of the body. Acoustic waves cannot pass through if there is a mismatch in acoustic impedance [138], while light photons cannot penetrate deeply due to tissue scattering [139].

In terms of wireless power transfer with alternating magnetic fields in untethered miniature robotics systems, three specific challenges exist. Firstly, as these robots typically exploit soft body deformation for locomotion, the use of stiff materials such as solid materials is avoided. However, such materials might exhibit desirable properties such as a high electrical conductivity. Secondly, the frequency of the alternating magnetic fields used does not typically exceed 13.56 MHz (26), as the absorption by the body increases as the frequency increases (27). This corresponds to a wavelength of at least 22 m in air, implying that near-field inductive coupling is the dominant mechanism for power transfer (i.e. Faraday's law of induction). As such, increasing the strength of the impinging magnetic field and increasing the area or number of turns of the receiver, are the only available methods to increase the harvested power. Lastly, although the power harvested can be increased by operating at the resonant frequency, this is difficult to achieve in reality for such robotic systems. The robot might encounter a variety of environmental conditions during operation which is hard to predict and cause the coupling efficiency and hence, harvested power to vary significantly. Therefore, for reliable and robust power transfer with alternating magnetic fields, a non-resonant inductive coupling approach is necessary.

4.2 Proposed approach

In view of this challenges and requirements, we propose a bi-layered design incorporating a metallic layer on a conventional sheet robot of the following dimensions (2 cm × 1 cm × 0.2 mm). Power is non-resonantly transferred to the metal layer on the robot inductively by a 338 kHz RF field, while locomotion is achieved with a low-frequency rotating magnetic field, not typically exceeding 100 Hz. Such a design combines robust, significant power transmission (~ 250 mW) at long distances (> 5 cm), with the existing locomotion capabilities of such untethered robots (**Figure 4.1A**). The reported design is easy to fabricate, scalable and most importantly, represents a hundredfold increase of usable power at least, for subsequent use in untethered robotic systems. Design strategies to optimise the electrical and mechanical performance based on simulations and experiments are presented. Enabled by this understanding and the increase in usable power, advanced robotic functionalities for untethered soft robots that can perform clinically relevant tasks, such as wireless sensing of the robot's environment properties through the use of an image sensor, are presented.

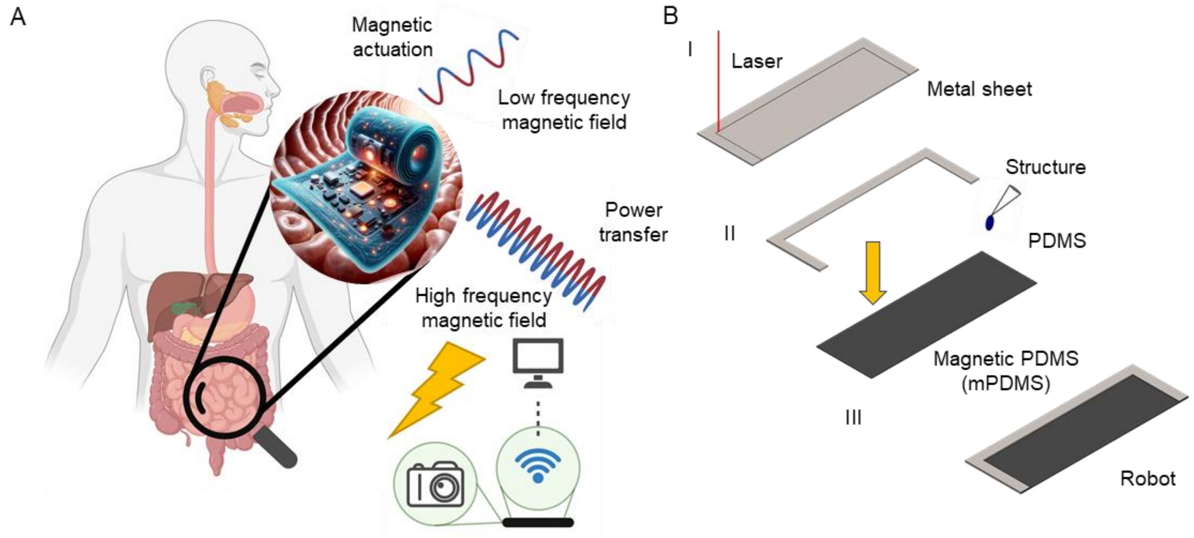

Figure 4.1: Proposed RF power transfer mechanism for untethered magnetic robots. (A) Conceptual illustration of the robot operating in the small intestine with enhanced functionalities enabled by electricity generation. Figure created with biorender.com. (B) Fabrication process. The design is first laser cut on a pre-selected metal sheet of appropriate thickness and material. The structure is detached and bonded directly to the magnetic PDMS with PDMS and left to cure on a hot plate.

4.3 Design and fabrication

200 µm PET tape (50650, Tesa) spacers were placed on a 3 mm acrylic sheet. Magnetic NdFeB microparticles (MQP−15–7, Magnequench) were mixed with 10:1 PDMS (Sylgard 184, Dow Corning) with a 3:1 weight ratio, hand-stirred for 5 min and degassed for 20 min. The mixture was then poured on the acrylic sheet with the excess mixture removed with a doctor blade. The sample was left on a hot plate to cure at 90 °C for 2 h before it was laser cut to the specified dimensions. The structures were then removed from the substrate, wrapped around a 6.4 mm diameter rod, and magnetised in a vibrating sample magnetometer (EZ7, Microsense) by exposure to a 1.8 T homogeneous magnetic field for 10 s. A thin layer of water-soluble glue (822095, Pritt) was applied between the robot and the rod to ensure good conformity of the robots to the profile of the rod. After magnetisation, the robots were soaked in DI water and detached from the rod. The pre-cut metal structures were then bonded to the robots with 10:1 PDMS and left to cure on a hot plate at 90 °C for 2 h (**Figure 4.1B**). A stereomicroscope (ZEISS Stemi 508, Carl Zeiss MicroscopyGmbH) was used to guide the assembly process.

4.4 Device characterisation

4.4.1 Electrical characterisation

Unless otherwise stated, square samples with a length of 1 cm were used for the characterisation experiments. These samples were laser cut (ProtoLaser U3, LPKF Laser & Electronics AG) from a larger sheet of the appropriate thickness and cleaned with IPA before removal. Before bonding, the connections were sandpapered with a P2000 grade sandpaper to remove any passivating oxide layers to ensure good electrical conductivity. The samples were attached perpendicularly to a circuit board (AA720, CIF) with conductive paint (SCP03B, Electrolube). A 1 Ω resistor (RC0100FR-071RL, YAGEO) was connected in series to the sample. During the tests, the RF heater (EASYHEAT 8310LI, Ambrell) was turned on for 10 s at 622 A and placed at a distance of 5 cm away from the sample. The circuit board was connected to an oscilloscope (WaveRunner 8404, Teledyne LeCroy) with micro-miniature coaxial cables (135-9701-311, Cinch Connectivity Solutions Johnson). From the data, the highest 10 peaks were extracted (**Figure 4.2A**) and recorded. The frequency response of the 1 Ω resistor was also tested and found to vary by less than 5% in the range of frequencies tested (**Figure 4.2B**).

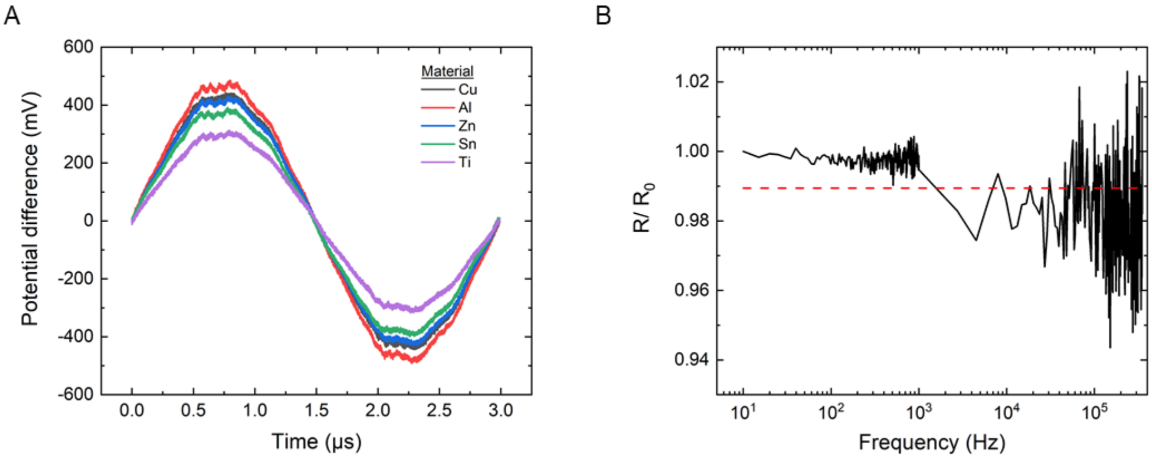

Figure 4.2: Electrical characterisation. (A) Experimentally recorded signal from the oscilloscope of one cycle for different 100 μm-thick materials. (B) Frequency response of the 1 Ω resistor used in subsequent characterisation tests. The red line denotes the average resistance across the frequencies tested (0.989 Ω).

To quantify the amount of power that the design can generate and the effects of changing the geometry, the design was characterised by placing it at a distance of 5 cm away and exposed to a RF field (**Figure 4.3A**). A 1 Ω resistor was connected in series to measure the power output. The voltage drop across the 1 Ω resistor was then measured with an oscilloscope. From an analysis of the system, controllable parameters (i.e. geometric, material and RF field) which would affect the power transfer were identified (**Figure 4.3B**).

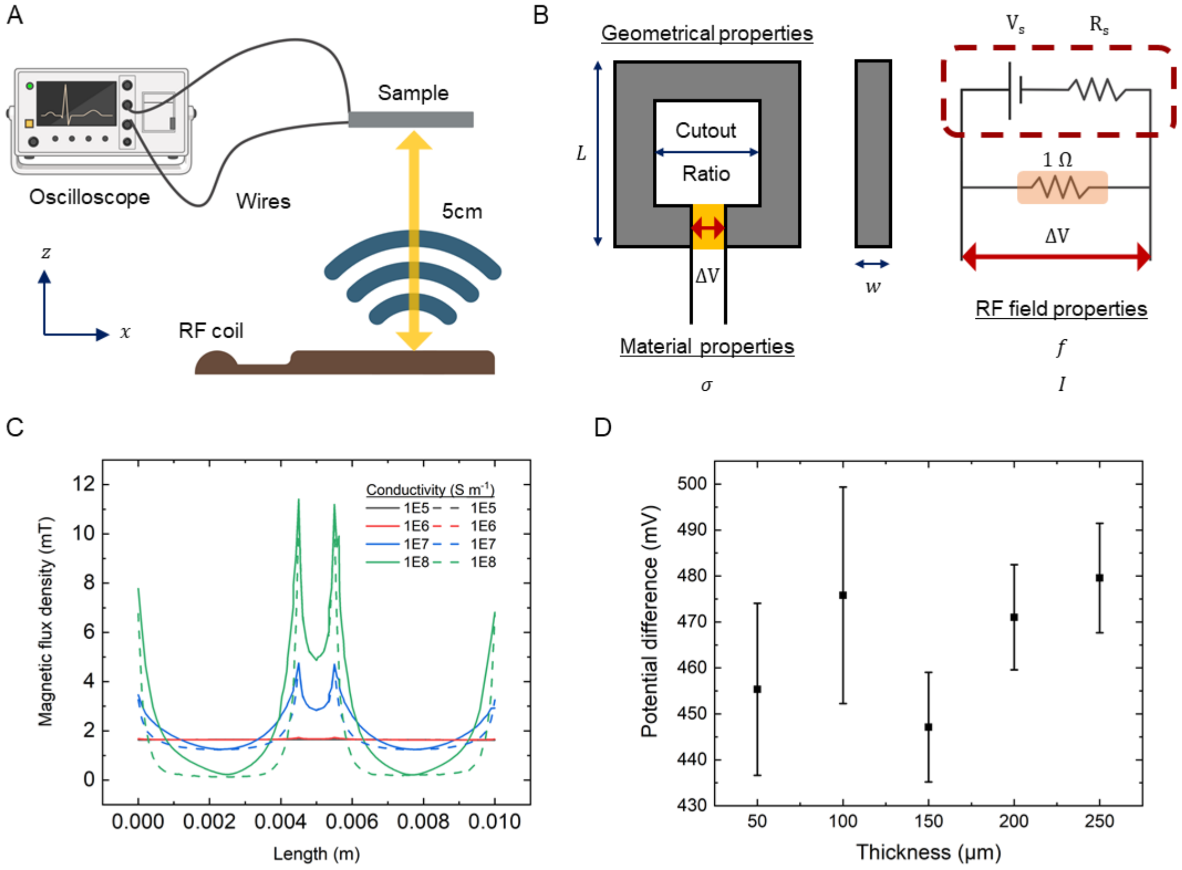

Figure 4.3: Characterisation of electrical performance. (A) Schematic of experimental setup. Figure created with biorender.com. (B) Identified geometric, material and RF field parameters affecting the potential difference recorded across a 1 Ω resistor. (C) Simulated magnetic flux density inside a 50 µm-thick sheet of different electrical conductivities. Dotted line represents the field at the centre of the sheet at 25 µm. (D) Experimentally determined peak values for copper of various thicknesses. Note that the values are not greater than 5% of the average value. Error bars represent the standard deviation.

In terms of material properties, the electrical conductivity (σ) is the dominant material property affecting power transfer. As σ increases, each layer in the material is able to support a larger electrical current density. For a given voltage induced by the applied magnetic flux through the loop, V_{in}, a corresponding current, I_{in}, is induced. At higher electrical conductivities, a larger I_{in} is induced for the given V_{in}, generating a larger flux to oppose this change in the process. Hence, the magnetic field penetrates less into the material, allowing a thinner material to be used when high σ materials are used. For maximum power transfer, the magnetic field should decay to 0 mT at the centre of the material, as this would signify that all the impinging magnetic fields have been converted to electrical energy (**Figure 4.3C, D**).

As such, in an ohmic material, increasing σ would either lead to an overall increase in V_{in} if saturation is not reached, or allow a thinner sample to be used while maintaining the saturation voltage, V_{sat}. It is observed experimentally that before V_{sat} is reached, increasing σ would result in a larger V_{in} across the 1 Ω resistor. As the material changed from titanium (σ = 1.85 × 10^6 S m^{-1}) to aluminium (σ = 3.75 × 10^7 S m^{-1}), the recorded V_{in} increases from 328 mV to 486 mV. (**Figure 4.4A**). The same increase in V_{in} to V_{sat} can also be achieved by increasing the thickness of the metallic layer (**Figure 4.4C, D**), although this would be undesirable for actuation. The results corresponded well with the simulations where it was observed that for a 100 µm-thick identical sample, the optimal electrical conductivity to achieve the maximum potential difference across the 1 Ω resistor occurred at σ = 2 × 10^7 S m^{-1}, close to that of the value of aluminium (**Figure 4.4B**).

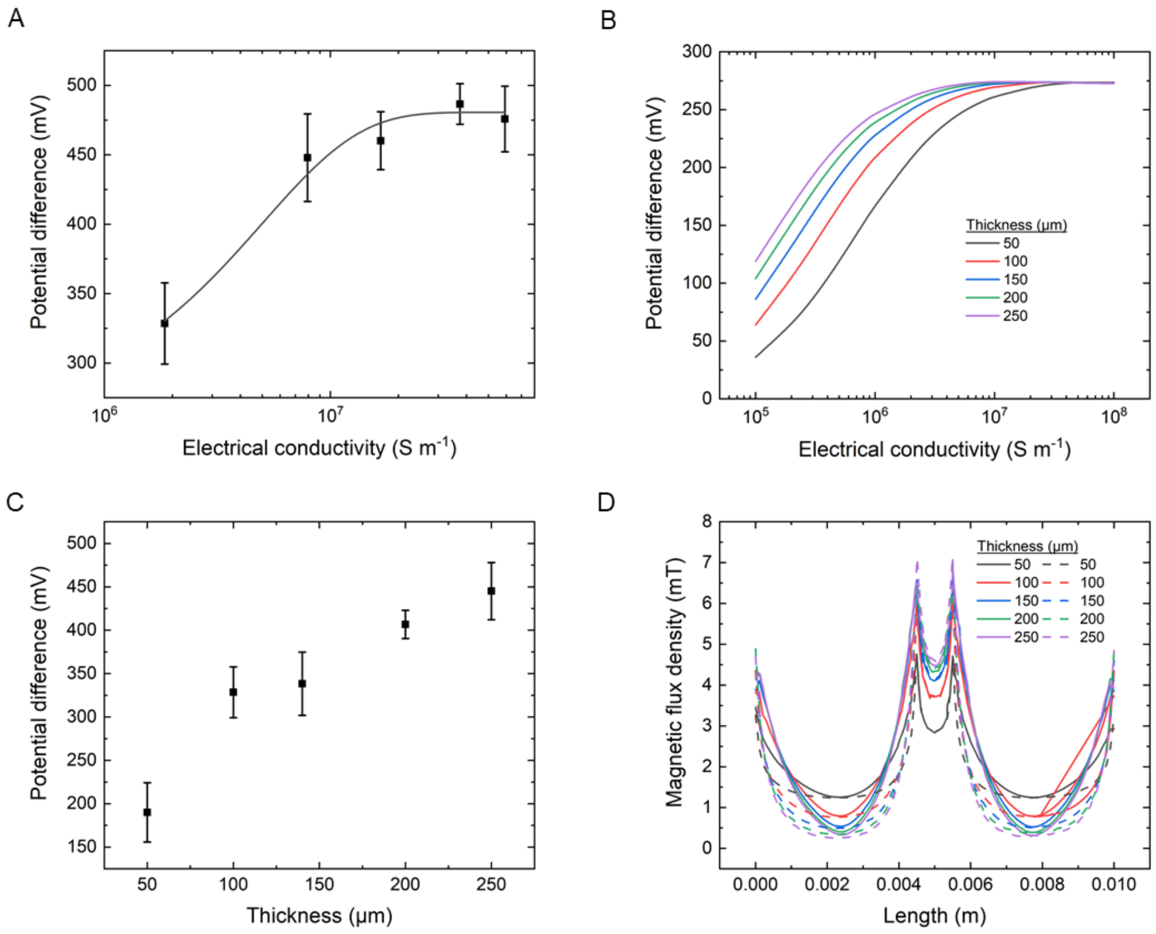

Figure 4.4: Characterisation of electrical performance. (A) Experimentally recorded potential difference peaks of 100 µm-thick samples made of different materials (n = 6). A cutout ratio of 0.8, corresponding to a channel width of 1 mm, is used. Error bars represent the standard deviation. (B) Simulated potential difference peaks of samples with different electrical conductivities and thicknesses. A cutout ratio of 0.8, corresponding to a channel width of 1 mm, is used. (C) Experimentally recorded potential difference peaks of titanium samples (cutout ratio = 0.8) of different thicknesses (n = 6). Error bars represent the standard deviation. (D) Simulated magnetic flux density inside samples of different thicknesses (cutout ratio = 0.8). Dotted line represents the field at the centre of the sheet.

Another effect of applying a RF field is the skin effect, which confines the induced I to run in a channel, and is defined by the equation:

$$\delta_{xy} = \sqrt{\frac{1}{\sigma \mu \pi f}}\,, \tag{4.1}$$

In non-magnetic materials, the current can be assumed to decay exponentially with depth (28) – 86% of the current would be confined to run in a layer two times of the skin depth. For materials with a higher σ, δ_{xy} will be smaller and the width of the channel can be further reduced without significantly affecting the flow of I, thereby increasing the area enclosed by the loop. Combined, this allows one to simultaneously achieve a higher V while increasing the mechanical compliance. We experimentally verified this effect with titanium samples (δ_{xy} = 0.635 mm) where it was observed that 1 cm square samples with a cutout ratio of 0.8 (i.e. channel width of 1 mm) recorded the highest V. When the channel width was decreased further below 1 mm, a drop in V was observed as the flow of I was affected, causing R_S to increase. The experimental results corresponded well with results obtained from simulations (**Figure 4.5**), where it was observed that the ratio at which the peak occurs shifts right as σ increases. This rightward shift indicates that a sample with a larger cutout ratio can be used. For instance, at $\sigma = 1 \times 10^5$ S m^{-1} (δ_{xy} = 2.73 mm) and 1×10^6 S m^{-1} (δ_{xy} = 0.865 mm), the optimal channel width was 3 mm and 1.5 mm,

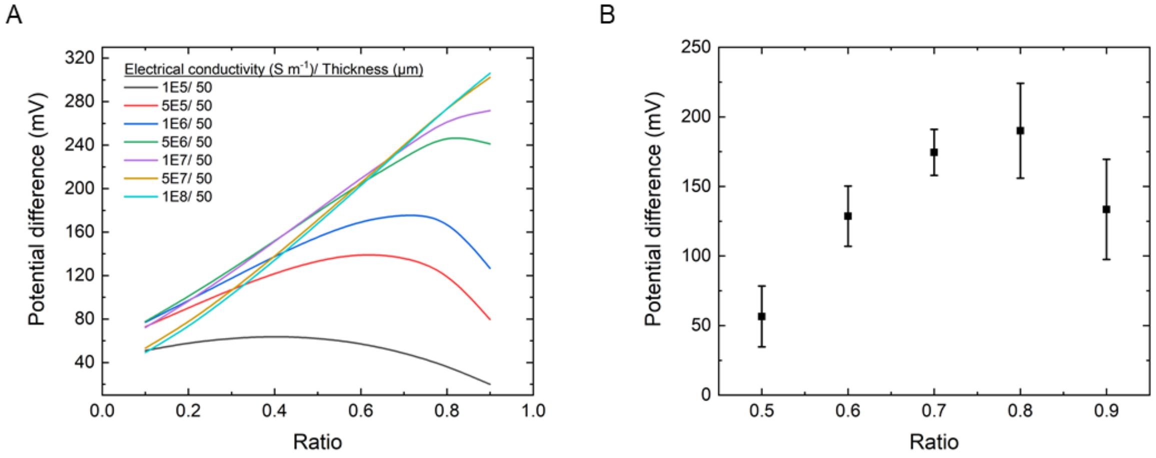

Figure 4.5: Characterisation of electrical performance. (A) Simulated potential difference peaks of 50 µm-thick samples with different cutout ratios and electrical conductivities. (B) Experimentally recorded potential difference peaks of 50 µm-thick titanium samples with different cutout ratios (n = 6). Error bars represent the standard deviation.

respectively. Moreover, to enhance the mechanical compliance of the robot, one side of the loop can be entirely removed because the enclosed area would still be identical. From experiments, we observe no difference in V_{in} (472 mV vs 486 mV) between a sample with all 4 sides present as compared to a sample with only 3 sides (**Figure 4.6A**). To further increase power harvested, the design can be looped to increase the enclosed area. Although the loops can be overlapped on top of one another, a planar design to looping was adopted because of how it would affect the mechanical properties of the robots (please see next section). As the number of loops was increased from 1 to 2, the voltage recorded increased by 56% from 486 mV to 759 mV (**Figure 4.6A**). Finally, the temperature rise of the metal strip when exposed to the RF field was assessed. As the cutout ratio increases and the volume available for heating decreases, the temperature change after 20 s of RF exposure drops from over 80 °C to 10 °C (**Figure 4.6B**).

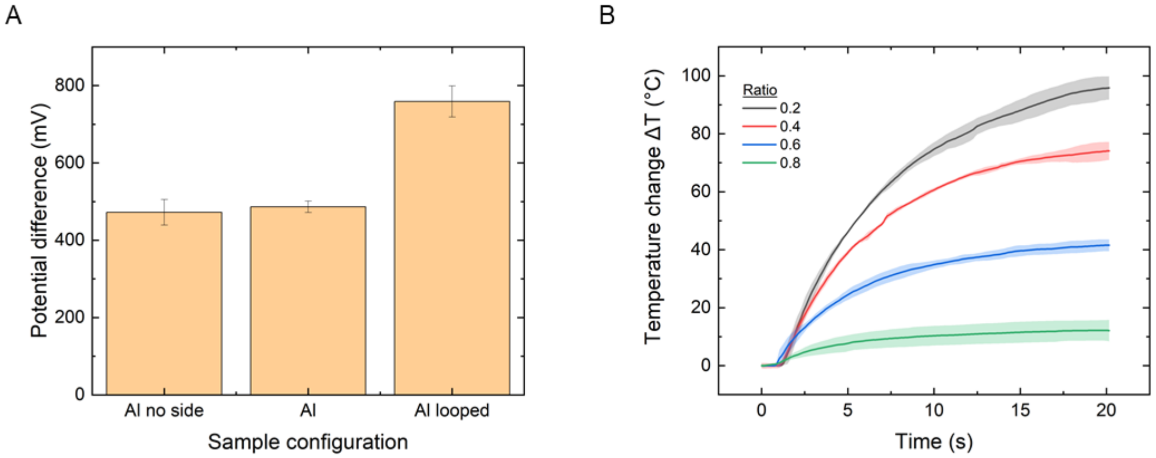

Figure 4.6: Characterisation of electrical performance. (A) Experimentally recorded potential difference peaks of 100 µm-thick aluminum samples with different configurations (n = 6). Error bars represent the standard deviation. (B) Temperature change of 50 µm-thick aluminum scales with identical areas but different cutout ratios over 20 s (n = 4). Error bars represent the standard deviation.

Without increasing the number of loops, another way to increase the power harvested would be to increase the rate of change of magnetic flux through the loop. This can be done either by increasing the input current into the RF coil or by increasing the frequency of the applied magnetic field. When the input frequency is increased from 200 Hz to 1000 Hz, the potential difference recorded across the resistor increases from 52 mV to 255 mV (**Figure 4.7A**). Similarly, increasing the input current from 200 A to 1000 A, increases the potential difference recorded across the resistor from

87 mV to 438 mV (**Figure 4.7B**). **Table 4.1** summarises the key effects and trade-offs of changing the various parameters.

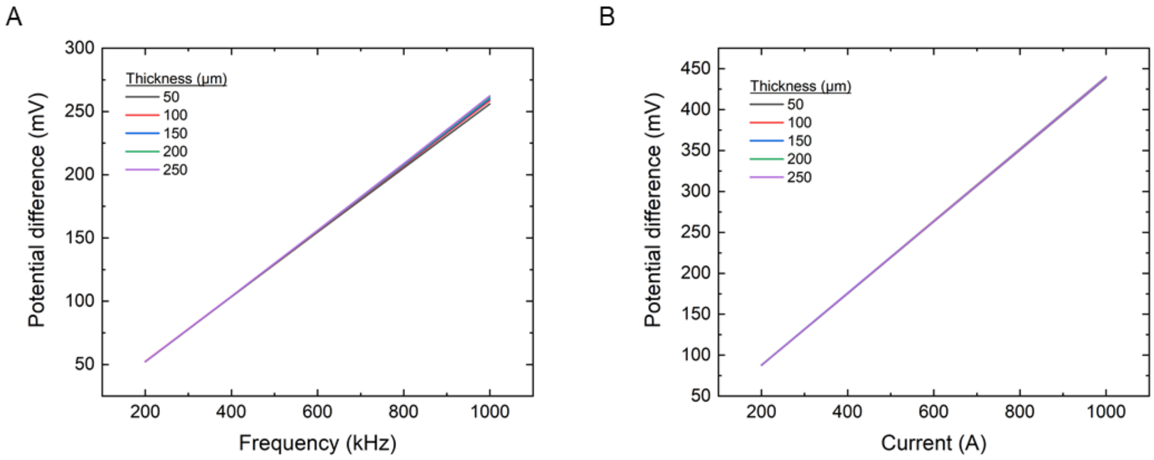

Figure 4.7: Characterisation of electrical performance with simulations in COMSOL. (A) Simulated potential difference peaks of 100 μm-thick aluminium samples (cutout ratio = 0.8) at different input RF frequencies. (B) Simulated potential difference peaks of 100 μm-thick aluminium samples (cutout ratio = 0.8) at different input RF currents.

Table 4.1: Summary of the various parameters which can be controlled to optimise the electrical performance.

Control parameter	**Classification**	**Effects**	**Considerations**
L	Geometrical	Increasing L increases V_{in}	Mechanical compliance decreases
w	Geometrical	Increasing w increases V_{in}	Mechanical compliance decreases
Cutout ratio	Geometrical	Increasing cutout ratio increases V_{in} and mechanical compliance	Lower limit dictated by δ_{xy}
σ	Material	Increasing σ decreases optimal w, increasing mechanical compliance	Cutout ratio can be increased to increase V_{in}
E	Material	Decreasing E increases mechanical compliance	Electrical conductivity changes
f	RF field	Increasing f increases V_{in}	Channel width can be decreased due to drop in δ_{xy}
I_{in}	RF field	Increasing I_{in} increases V_{in}	-

4.4.2 Mechanical characterisation

Next, we conducted characterisation experiments to observe and study the effects of adding the metallic layer on locomotion. To estimate the forces required to bend the composite structure and hence, the strength of the external magnetic fields required to actuate the robot, we looked at the flexural compliance of the composite structure by performing a three-point bending test on the robot. By looking at the equation governing mechanical deformation, the channel width, b_{Metal}, thickness, w_{Metal}, and Young's modulus, E, have to be reduced in order to reduce the bending moment and the magnetic torque required. Details of the equation governing mechanical deformation are provided in the next section (**Eq. 4.2**).

We first studied the effects of changing the thickness of the layer and also the width of the channel. Aluminium was used because it offered high electrical conductivity to density ratio. Since the frequency of RF exposure was 338 kHz, the skin depth was calculated to be approximately 141 µm. As such, we hypothesised based on results presented earlier that a b_{Metal} of 0.3 mm for a 50 µm-thick aluminium layer would offer the best combination of power harvesting and mechanical flexibility. As such, the characterisations focused on values of b_{Metal} and w_{Metal} in this range. From the experiments conducted, we find that although addition of the aluminium layer on the magnetic polymer increases the maximum stress experienced of the composite, this value did not exceed 4 times of the magnetic polymer (mPDMS). The maximum stress recorded was 0.31 MPa and 1.38 MPa for mPDMS and the structure with 0.5 mm channel, respectively (**Figure 4.8A**). Consistent with the theoretical analysis performed, we find that using both narrower b_{Metal} and lower w_{Metal}were advantageous in reducing the maximum stress of the composite. In fact, when a 40 µm-thick aluminium layer with a 0.3 mm channel was used, the maximum stress recorded was 0.38 MPa, which implied that the composite structure was almost as easy to deform as mPDMS.

To estimate the magnetic fields required to actuate the robot, we calculated the flexural chord modulus of elasticity of the structure (E_{FC}), which is denoted by the gradient of the linear region of the stress-strain curve. Consistent with the theoretical analysis performed, we find that reducing the b_{Metal}, w_{Metal} and E (in this order) are important in reducing the E_{FC}, and hence, the magnetic fields required to actuate the robot. When the thickness of the aluminium layer used was reduced by 30% from 60 µm to 40 µm, the E_{FC} fell by over 66% from 68.4 MPa to 22.8 MPa. As compared to the mPDMS, which gave a value of 9.16 MPa, this meant that the 40 µm-thick, 0.3 mm channel width aluminium-mPDMS composite required a field which was two times larger for actuation. When the channel size was decreased by 40% from 0.5 mm to 0.3 mm, E_{FC} dropped by 32% from 76.8 MPa to 52.0 MPa. Similarly, when the Young's modulus was reduced by 45.6% from 129.8 GPa to 70.6 GPa, E_{FC} dropped by 14.5% from 60.8 MPa to 52.0 MPa (**Figure 4.8B**).

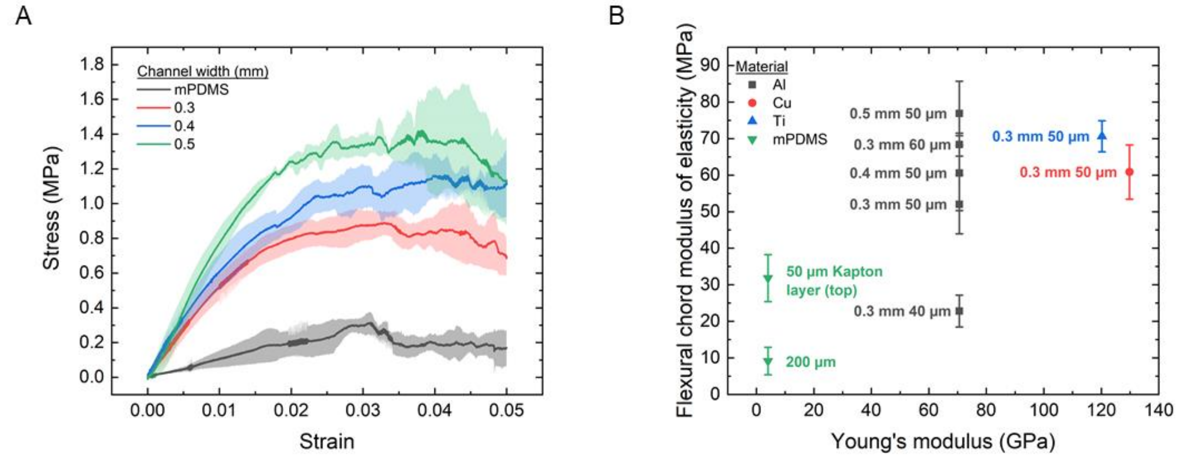

Figure 4.8: Characterisation of mechanical performance. (A) Stress-strain curve for a 20 × 10 × 0.25 mm sample with different channel widths (n = 3). Error bars represent the standard deviation. (B) Comparison of the flexural chord modulus of elasticity (E_{FC}) for different materials and thicknesses (n = 3). Error bars represent the standard deviation.

As the robot would also have to carry electrical components to perform the specified tasks, we also looked at the effects of placing the components on the robot. In this regard, we find that isolating the rigid electrical components onto islands is an effective strategy in lowering the maximum stress, and hence the magnetic fields required to actuate the composite robot. Specifically, the maximum stress experienced decreased by 84.3% from 10.4 MPa to an average 1.63 MPa. This drop was also observed to be independent of the size of the island. Islands with lengths ranging from 2 mm to 5 mm all recorded the same drop in maximum stress (**Figure 4.9A**).

Next, we focused on the bending response of the robot. The test involved analysing the free deflection of the robot when it was fixed at one end and exposed to a uniform magnetic field. From the tests performed, we observed that there was a drop in the bending performance after addition of the metallic layer, with the largest drop of 39% recorded by a 50 µm-thick aluminium layer with a channel width of 0.5 mm, from 74.6° to 45.4°. Consistent with the conclusions drawn from the three-point bending test, we observe that lower thicknesses and channel widths enhances mechanical compliance. This, in turn, makes the robot easier to actuate with magnetic fields (**Figure 4.9B**). Alternatively, this could be offset by increasing the strength of the magnetic field applied or by utilising a material with a higher σ – a material with a higher σ would allow a thinner, narrower channel to be used.

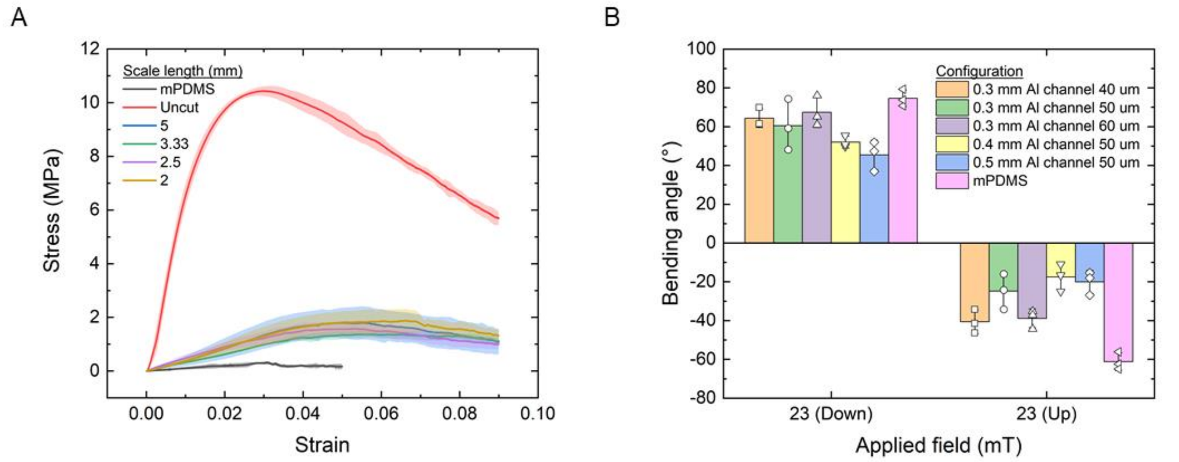

Figure 4.9: Characterisation of mechanical performance. (A) Stress-strain curve for a 20 × 10 × 0.25 mm sample with different scale length to simulate the effects of placing electrical components on the robot (n = 3). Error bars represent the standard deviation. (B) Deflection of magnetic polymer with aluminium layers of different thicknesses and geometries (n = 3). Error bars represent the standard deviation.

4.4.3 Analysis of the system

For a composite material with a rectangular cross-section of width, b and thickness, w, the deflection, w_d, can be described by the Euler-Bernoulli equation for beams (**Eq. 4.2**).

$$\boldsymbol{M_b} = E_{Metal}\, V_{F_{Metal}}\, I_{2nd_{Metal}} \frac{\partial^2 w_d}{\partial x^2} + E_{mPDMS} V_{F_{mPDMS}}\, I_{2nd_{mPDMS}} \frac{\partial^2 w_d}{\partial x^2}. \tag{4.2}$$

where $I_{2nd_{mat}}$ is the second moment of area ($\frac{bw^3}{12}$ for a rectangular cross-section), M_b is the bending moment and V_F is the volume fraction. Since the Young's modulus of most metals is in the order of GPa while the Young's modulus of mPDMS is in the order of MPa, assuming the thickness of both layers is in the order of microns, the properties of the metallic layer are dominant in the calculation of the $\boldsymbol{M_b}$ required. To minimise $\boldsymbol{M_b}$, b_{Metal}, E_{Metal} and w_{Metal} need to be minimised.

4.5 Multifunctional robotic capabilities

To highlight the advantages of implementing such a design in untethered magnetic miniature robots, we exploited the higher power which could be non-resonantly harvested. In this regard, the electrical energy harvested was used to power a camera (NanEye, ams Osram) and transmit an image wirelessly via Bluetooth to a receiver placed 10 cm away. The camera was selected because it was a functionality requiring at least 1.5 mW of power for operation. To implement such a system, the AC voltage generated during exposure to the 338 kHz RF field was passed through an energy harvester power supply (LTC 3588, Analog Devices), operating in the piezoelectric configuration, for conversion into a stable 3.3 V DC voltage. This voltage was then fed to a microprocessor controller unit comprising a Surface Mount Device (SMD) crystal oscillator (ECS-400-6-47B2-CKM-TR, ECS), a Bluetooth communication module (ESP32-C3FN4, Espressif Systems) and the camera (**Figure 4.10A**). This allowed an image 80 × 80 pixels wide to be transmitted every 5 s to the external receiver (**Figure 4.10B**). Although a camera was implemented here in this work, any other functionalities such as an accelerometer, temperature sensor or strain sensor could technically also be implemented on this developed platform. Implementation of the energy harvester power supply also grants more flexibility in supporting the necessary electronic infrastructure by allowing for four different set voltages to be achieved on a single setup (**Figure 4.10C**).

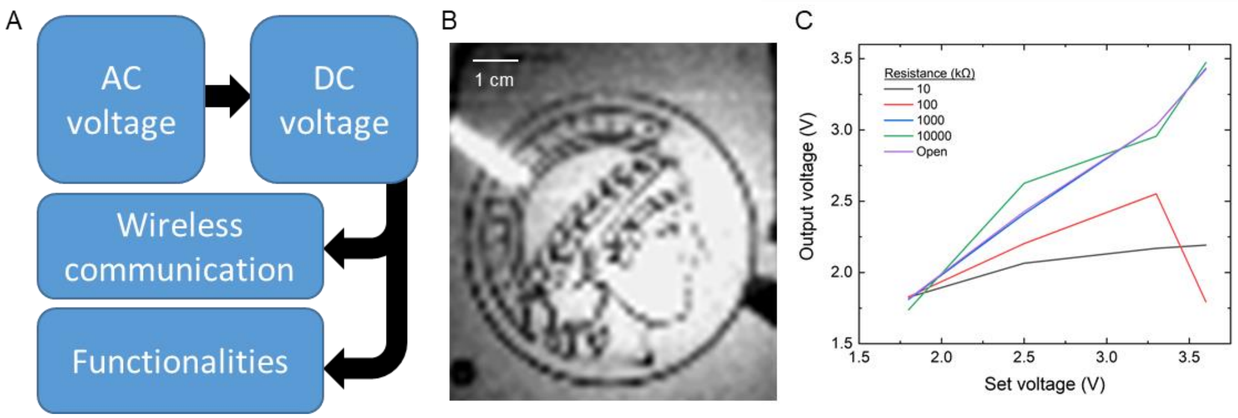

Figure 4.10: Integration of design with electronics towards multi-functional robots. (A) Block diagram. Details of implementation are provided in **Figure 4.11**. (B) Image captured and transmitted via Bluetooth by a camera powered with the design. (C) Graph of set against output voltage of the energy harvester power supply across various resistances.

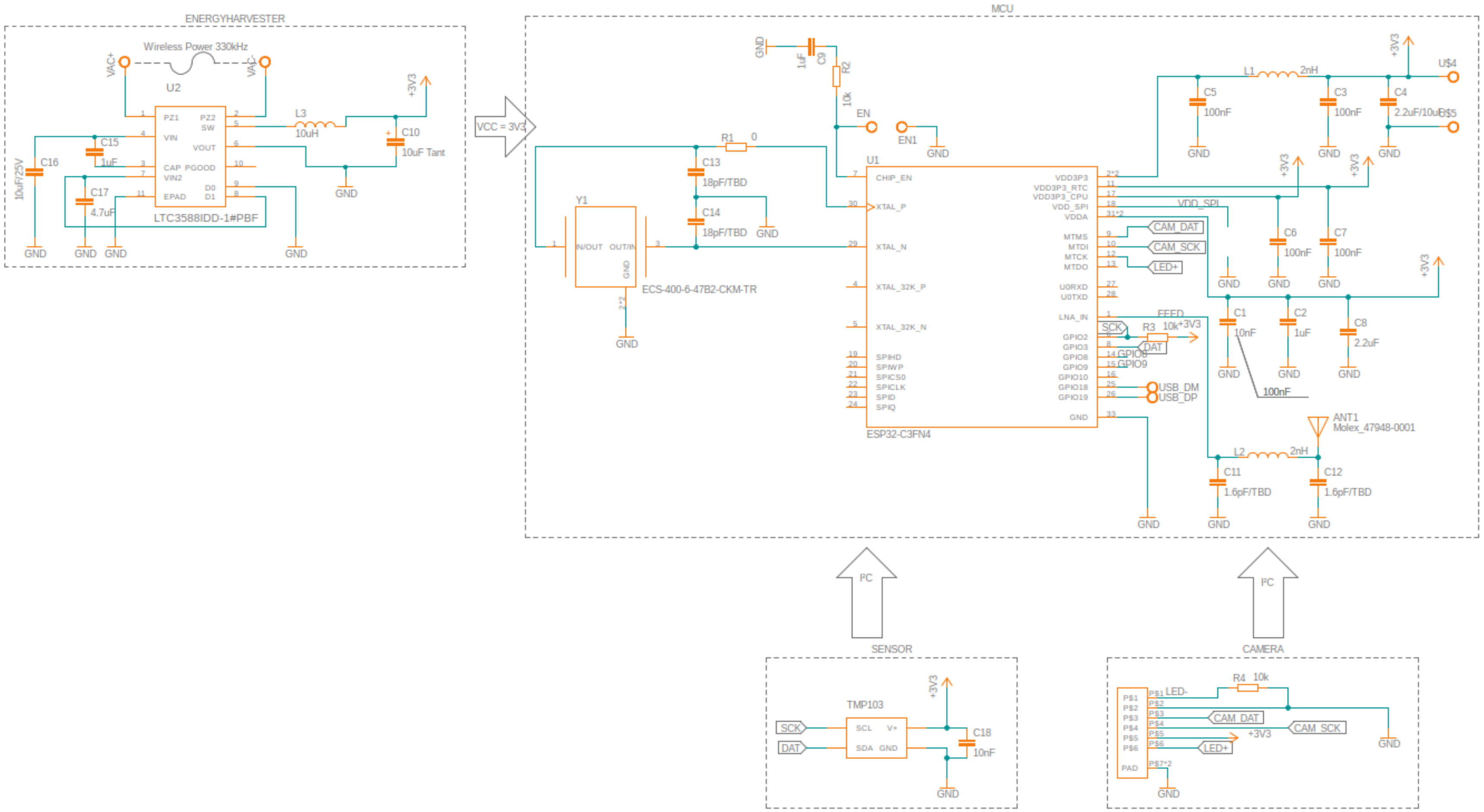

Figure 4.11: Detailed schematic of the demonstrated implementation.

4.6 Summary

In this work, we introduced a bi-layered design to allow power to be non-resonantly transferred to an untethered magnetic robot via inductive power transfer with a 338 kHz RF field. Actuation is achieved with a low-frequency rotating magnetic field. The optimised bi-layer design allowed rigid materials to be incorporated on the soft magnetic robot body without sacrificing on the bending compliance and hence locomotion of the robot. This allowed significant power (~250 mW) to be transmitted at distances over 5 cm. With the presence of on-board power, multifunctional robotic capabilities such as wireless sensing of the robot's environment, through the use of a camera, were realised. As the reported design works in the non-resonant regime, it presents a more robust and reliable method of transferring power to the robot. This is especially crucial in biomedical applications because the inter-patient and even intra-patient heterogeneity of tissue properties makes it difficult for a design to consistently work in the resonant regime.

For successful translation, future studies should focus on downsizing the required electronics to a size compatible with the magnetic soft robot. As of now, the demonstrations were performed with the design harvesting the power and then transferred to an off-board external circuit. In the next step, the electronics can be fabricated on a flexible circuit board instead of the printed circuit board used currently. This will further increase the deformability and hence, locomotion abilities of the robot, allowing it to access a larger workspace with the functionalities it carries.

Chapter 5: Conclusion

5.1 Summary of the thesis contributions

In this thesis, three modules were introduced to enhance the functionalities of untethered miniature robots beyond locomotion and surface cargo delivery. Specifically, the modules developed allows these robots to generate high forces, heat and electricity. The modules exploit physical intelligence and smart design to allow rigid materials to be incorporated on the soft substrates without compromising on their locomotion and mechanical compliance.

The specific contributions of each chapter are as follows:

In Chapter 2,

- a wireless spring-preloaded barbed needle on-demand release mechanism, which can provide up to 1.6 N of force to drive a barbed needle into soft tissues is proposed.
- design guidelines aimed at maximising anchoring over the range of the most biological tissues (kPa range) and extending the operating depth of the device inside the body (up to 75%) are also presented.
- mechanism can be easily integrated into existing untethered soft robotic platforms without sacrificing their mobility.
- robust on-demand anchoring on 3D ex vivo tissue surfaces can now be achieved.
- additional functionalities such as controlled detachment and sub-surface drug delivery into 3D cancer spheroids can be simply achieved by changing the needle type.

In Chapter 3,

- a pangolin-inspired bi-layered soft robot design which gives these robots the ability to locally generate heat without compromising mechanical compliance is proposed.
- design guidelines aimed at maximising heating are presented. The pangolin-inspired design allows for mechanical compliance and heating performance to be simultaneously achieved.
- the reported design achieves heating > 70 °C at large distances > 5 cm within a short period of time < 30 s, allowing users to realise on-demand localised heating in tandem with shape-morphing capabilities.

- advanced robotic functionalities, such as selective cargo release, in situ demagnetisation, hyperthermia and mitigation of bleeding, on tissue phantoms and ex vivo tissues are shown with the new functionality.

In Chapter 4,

- a design to allow these robots to wirelessly harvest electricity from the RF field is proposed.
- design guidelines aimed at maximising power are presented. The non-resonant energy harvesting allows for robust power transfer, which is useful in biomedical applications.
- despite a small footprint < 2 cm^2, the robot is able to harvest power > 250 mW at large distances > 5 cm.
- enabled by these advances, functionalities such as wireless sensing of the robot's environment, through the use of a camera is demonstrated.

Each of the functional modules introduced in this work serves as the backbone on which future, application-specific variants of these untethered robots can be introduced. Moreover, the working principles of the functional modules have been elucidated and methods to optimise the modules across different size scales were presented. Wherever possible, experiments were performed on ex vivo tissues to better simulate the actual working environment. Taken together, the results presented in this thesis would facilitate future development of these robots towards biomedical applications.

5.2 Outlook

Recent advances in this field, including those introduced in this work, have pushed the capabilities of these robots beyond locomotion and cargo delivery, by deploying these robots in ever more realistic models and by increasing the number of functionalities these robots possess.

Despite these advances, significant obstacles remain before these robots can be deployed to tackle real-world biomedical issues. Specifically, researchers have predominantly approached this field from a robotics perspective, rather than starting from a medical need. As such, while the reported advances represent a significant contribution in the field of robotics, the impact of such robots in actual scenarios might be limited. Even in instances where a medical scenario was identified with conceptual demonstrations performed on ex vivo tissues, the efficacy of the potential treatment was not comprehensively evaluated – the studies still focused primarily on evaluating the robot's performance. In the next phase of the development of these robots, researchers should focus on three aspects, which are listed in no order of priority.

Firstly, researchers should aim to address and bridge the above-mentioned inward focus of the field by designing functional miniature magnetic robots based on actual clinical requirements or around an actual medical problem and evaluating their therapeutic efficacy. Working from a needs-based approach is necessary because the intended application of the robot often dictates the design specifications of the robot, ranging from the size to the functionalities that the robot should ultimately carry on board. Adopting such an approach, therefore, would allow researchers to demonstrate how miniature magnetic robots can complement or even supersede existing treatment options. Successful validation of the therapeutic efficacy of these untethered miniature robots would also address the long-standing question about the value of deploying untethered robots in biomedical applications and bring these robots another step closer to the bedside. This would greatly strengthen the case for labs to invest resources for in vivo experiments and for application-specific research questions to be tackled. For instance, in the proposed working environment, what would be the best locomotion strategy that these robots should adopt, the imaging modality which can be used to track and control these robots among many others?

Secondly, many of the functionalities in question focus on physical (i.e. mechanical) methods such as heat rather than chemical methods (i.e. medication). However, over 70% of visits to clinicians in the United States in 2020 involved pharmacological methods, a chemical-based method [140].

As such, if robotics researchers collaborated with biologists working to uncover physiological (i.e. relationship from cells to tissues to organs to body functions) and pathophysiological (i.e. how changes in physiology results in diseases) processes underlying diseases, treatments based on physical methods which have been developed on these robots could then be possibly exploited. This will further expand the utility of these untethered robots. In the same vein, these functionalities might enable new forms of localised drug delivery. For instance, two inert compounds can be brought to the target location, allow for on-site fabrication of a drug or compound which might have been too reactive to have been delivered through normal means. With regards to these two points, researchers must still closely work with clinicians in order to find the most appropriate medical problem to tackle.

Finally, research should still continue on the current track of developing new functionalities for these robots. The objectives of this are twofold. Firstly, new functionalities might enable more treatments or at the very least, continue to close the gap between the current state-of-the-art medical instruments and untethered miniature robots. Secondly, the new functionalities might also inspire new applications in other fields beyond biomedical applications, such as in biomechanics. Specifically, untethered magnetic robots might serve as a good model system for biomechanics researchers to study and understand animal locomotion. With the incorporation of new functionalities, it may now be possible to take into account a wider variety of characteristics affecting locomotion. For instance, the heating scales introduced in Chapter 3 might allow for researchers to use thermal responsive polymers, which can change properties such as its stiffness upon application of heat, to better study how temperature changes in the animal’s body can affect locomotion (i.e. cold vs warm muscles).

This would allow the field to thrive and remain relevant in the coming decades.

Appendix: MATLAB codes used for data processing

three_pt_bending_processing.m

```
 % % Test variables
L = 10; % support span [mm]
h = 0.2 + 0.0499600479360895; % thickness of beam including plate thickness [mm]
b = 10; % width of beam [mm]

 % % INPUT FILE LOCATION
A{1} = readmatrix('C:\Users\Desktop\1 (1).csv');
A{2} = readmatrix('C:\Users\Desktop\1 (2).csv');
A{3} = readmatrix('C:\Users\Desktop\1 (3).csv');

force_combin = zeros(15000,3);
mid_span_deflection = zeros(15000,3);

for n = 1:3
    T = A{n};
    for i = 1:15000
    force_combin(i,n) = T(i,3);
    mid_span_deflection(i,n) = T(i,2);
    end
end
```

```
 % % GET AVERAGE AND STD

stress = zeros(15000,3);

strain = zeros(15000,1);

export = zeros(15000,3);


for j = 1:3

    stress (:,j) = force_combin(:,j) * 10^-3 * 1.5 * L / (b * h^2);

    strain (:,j) = mid_span_deflection(:,j) * 6 * h / L^2;

end

export(:,1) = mean(strain,2);

export(:,2) = mean(stress,2);

export(:,3) = std(stress,[],2);
```

temperature_data_processing_batch.m

```
% % INPUT FRAME SIZE AND FILE LOCATION

frame_size = 60;


A{1} = readmatrix('C:\Users\Desktop\1 (1).csv');

A{2} = readmatrix('C:\Users\Desktop\1 (2).csv');

A{3} = readmatrix('C:\Users\Desktop\1 (3).csv');

A{4} = readmatrix('C:\Users\Desktop\1 (4).csv');

A{5} = readmatrix('C:\Users\Desktop\1 (5).csv');

A{6} = readmatrix('C:\Users\Desktop\1 (6).csv');


temp_combin = zeros(500,6);


for n = 1:6

    T = A{n};

    rows = size(T,1);

    columns = size(T,2);

    frames = rows/ frame_size;

    B = zeros(rows/2, columns/2);

    C = zeros(frames,1);

    temp = zeros(frames,1);

    temp_1 = zeros(frames+1,1);

    temp_final = zeros(frames,1);
```

```
  % % CONVERT TEMPERATURE

for j = 1:rows

   for k = 1:columns/2

       B(j,k) = T(j,2*k)+ T(j,(2*k))/ 1000;

   end

end

% % GET AVERAGE

for i = 1:frames

   for j = 1:frame_size

       for k = 1:frame_size

       C(i) = C(i) + B(j+ frame_size*(i-1),k);

       end

   end

end

C = C/ frame_size^2;

temp = C - C(1,1);

i = 2;

% % REMOVE INITIAL ZERO-PORTION

for j = 1:frames

   if temp (j,1) >= 0.1

       temp_1 (i,1) = temp (j,1);

       i = i + 1;

 end
```

```
    end

    % % REMOVE RF OFF

    for i = 1:frames

        if temp_1 (i+1,1) - temp_1 (i,1) <= 0 && i > 500

            temp_1 (i,1) = 0;

        end

    end

    % % REMOVE NOISE

        temp_final = medfilt1 (temp_1,20);


    % % Remove last digits from filtered results

        for i = 1:500

            temp_combin(i,n) = temp_final(i,1);

        end

end


% % Final

temp_process = zeros (500,2);

for i = 1:500

   temp_process(:,1) = mean(temp_combin,2);

   temp_process(:,2) = std(temp_combin,[],2);

 end
```

peak_finder_top10_v2.m

```
% % INPUT NUMBER OF SAMPLES

 k = 6;


% % INPUT FILE LOCATION

A{1} = readmatrix('C:\Users\Desktop\1 (1).csv');

A{2} = readmatrix('C:\Users\Desktop\1 (2).csv');

A{3} = readmatrix('C:\Users\Desktop\1 (3).csv');

A{4} = readmatrix('C:\Users\Desktop\1 (4).csv');

A{5} = readmatrix('C:\Users\Desktop\1 (5).csv');

A{6} = readmatrix('C:\Users\Desktop\1 (6).csv');


curve_combin = zeros(10,k);

curvature_export = zeros(1,2);


for n = 1:k

    T = A{n};

    T1 = medfilt1(T(3:end,2));

    [pks, locs] = findpeaks(T1, 3, 'MinPeakDistance', 6500);

    T2 = maxk(pks,10);

    curve_combin(:,n) = T2*1000;

    figure

    plot(T1)
```

```
    hold on

    plot(3*locs, pks, 'o')

    hold off

end


% % GET AVERAGE AND STD

 curvature_export(:,1) = mean(curve_combin, "all");

curvature_export(:,2) = std(curve_combin, 0, "all");
```

References

[1] M. Sitti *et al.*, "Biomedical Applications of Untethered Mobile Milli/Microrobots," *Proc. IEEE*, vol. 103, no. 2, pp. 205–224, 2015.

[2] F. Mark and B. Lawrence S., Friedman Lawrence J., *Sleisenger and Fordtran's Gastrointestinal and Liver Disease*, 11th ed. Elsevier, 2020.

[3] M. Shi *et al.*, "A Protein-Binding Molecular Photothermal Agent for Tumor Ablation," *Angew. Chemie - Int. Ed.*, vol. 60, no. 24, pp. 13564–13568, 2021.

[4] Q. Zhuang *et al.*, "Bacteria-derived membrane vesicles to advance targeted photothermal tumor ablation," *Biomaterials*, vol. 268, p. 120550, Jan. 2021.

[5] L. Zhao, X. Zhang, X. Wang, X. Guan, W. Zhang, and J. Ma, "Recent advances in selective photothermal therapy of tumor," *J. Nanobiotechnology*, vol. 19, no. 1, pp. 1–15, 2021.

[6] J. Li *et al.*, "Development of a magnetic microrobot for carrying and delivering targeted cells," *Sci. Robot.*, vol. 3, no. 19, Jun. 2018.

[7] H. Lu *et al.*, "A bioinspired multilegged soft millirobot that functions in both dry and wet conditions," *Nat. Commun.*, vol. 9, no. 1, p. 3944, Sep. 2018.

[8] U. Bozuyuk, O. Yasa, I. C. Yasa, H. Ceylan, S. Kizilel, and M. Sitti, "Light-Triggered Drug Release from 3D-Printed Magnetic Chitosan Microswimmers," *ACS Nano*, vol. 12, no. 9, pp. 9617–9625, Sep. 2018.

[9] W. Hu, G. Z. Lum, M. Mastrangeli, and M. Sitti, "Small-scale soft-bodied robot with multimodal locomotion," *Nature*, vol. 554, no. 7690, pp. 81–85, Feb. 2018.

[10] S. Jeon *et al.*, "Magnetically actuated microrobots as a platform for stem cell transplantation," *Sci. Robot.*, vol. 4, no. 30, p. eaav4317, May 2019.

[11] I. C. Yasa, A. F. Tabak, O. Yasa, H. Ceylan, and M. Sitti, "3D-Printed Microrobotic Transporters with Recapitulated Stem Cell Niche for Programmable and Active Cell Delivery," *Adv. Funct. Mater.*, vol. 29, no. 17, p. 1808992, Apr. 2019.

[12] O. Onaizah and E. Diller, "Tetherless Mobile Micro-Surgical Scissors Using Magnetic Actuation," in *2019 International Conference on Robotics and Automation (ICRA)*, 2019, pp. 894–899.

[13] M. Dong *et al.*, "3D-Printed Soft Magnetoelectric Microswimmers for Delivery and Differentiation of Neuron-Like Cells," *Adv. Funct. Mater.*, vol. 30, no. 17, p. 1910323, Apr. 2020.

[14] Y. Alapan, U. Bozuyuk, P. Erkoc, A. C. Karacakol, and M. Sitti, "Multifunctional surface microrollers for targeted cargo delivery in physiological blood flow," *Sci. Robot.*, vol. 5, no. 42, p. eaba5726, May 2020.

[15] H. Lu, Y. Hong, Y. Yang, Z. Yang, and Y. Shen, "Battery-Less Soft Millirobot That Can Move, Sense, and Communicate Remotely by Coupling the Magnetic and Piezoelectric Effects," *Adv. Sci.*, vol. 7, no. 13, p. 2000069, Jul. 2020.

[16] D. Son, H. Gilbert, and M. Sitti, “Magnetically Actuated Soft Capsule Endoscope for Fine-Needle Biopsy,” *Soft Robot.,* vol. 7, no. 1, pp. 10–21, Feb. 2020.

[17] M. B. Akolpoglu, N. O. Dogan, U. Bozuyuk, H. Ceylan, S. Kizilel, and M. Sitti, “High-Yield Production of Biohybrid Microalgae for On-Demand Cargo Delivery,” *Adv. Sci.*, vol. 7, no. 16, Aug. 2020.

[18] X. Fan, X. Dong, A. C. Karacakol, H. Xie, and M. Sitti, “Reconfigurable multifunctional ferrofluid droplet robots,” *Proc. Natl. Acad. Sci.*, vol. 117, no. 45, pp. 27916–27926, Nov. 2020.

[19] H. Ceylan, N. O. Dogan, I. C. Yasa, M. N. Musaoglu, Z. U. Kulali, and M. Sitti, “3D printed personalized magnetic micromachines from patient blood–derived biomaterials,” *Sci. Adv.*, vol. 7, no. 36, pp. 1–11, Sep. 2021.

[20] J. Zhang *et al.*, “Voxelated three-dimensional miniature magnetic soft machines via multimaterial heterogeneous assembly,” *Sci. Robot.*, vol. 6, no. 53, p. eabf0112, Apr. 2021.

[21] Z. Ren *et al.*, “Soft-bodied adaptive multimodal locomotion strategies in fluid-filled confined spaces,” *Sci. Adv.*, vol. 7, no. 27, p. eabh2022, Jul. 2021.

[22] C. Hong *et al.*, “Magnetically actuated gearbox for the wireless control of millimeter-scale robots,” *Sci. Robot.*, vol. 7, no. 69, Aug. 2022.

[23] T. Wang *et al.*, “Adaptive wireless millirobotic locomotion into distal vasculature,” *Nat. Commun.*, vol. 13, no. 1, p. 4465, Aug. 2022.

[24] M. B. Akolpoglu *et al.*, “Magnetically steerable bacterial microrobots moving in 3D biological matrices for stimuli-responsive cargo delivery,” *Sci. Adv.*, vol. 8, no. 28, Jul. 2022.

[25] J. Zhang, R. H. Soon, Z. Wei, W. Hu, and M. Sitti, “Liquid Metal-Elastomer Composites with Dual-Energy Transmission Mode for Multifunctional Miniature Untethered Magnetic Robots,” *Adv. Sci.*, vol. 9, no. 31, p. 2203730, Nov. 2022.

[26] Y. Tang, M. Li, T. Wang, X. Dong, W. Hu, and M. Sitti, “Wireless Miniature Magnetic Phase-Change Soft Actuators,” *Adv. Mater.*, vol. 34, no. 40, p. 2204185, Oct. 2022.

[27] M. Sun *et al.*, “Reconfigurable Magnetic Slime Robot: Deformation, Adaptability, and Multifunction,” *Adv. Funct. Mater.*, vol. 32, no. 26, Jun. 2022.

[28] M. Li, Y. Tang, R. H. Soon, B. Dong, W. Hu, and M. Sitti, “Miniature coiled artificial muscle for wireless soft medical devices,” *Sci. Adv.*, vol. 8, no. 10, p. eabm5616, Mar. 2022.

[29] N. O. Dogan *et al.*, “Remotely Guided Immunobots Engaged in Anti-Tumorigenic Phenotypes for Targeted Cancer Immunotherapy,” *Small*, vol. 18, no. 46, p. 2204016, Nov. 2022.

[30] Y. Lee *et al.*, “Multifunctional 3D-Printed Pollen Grain-Inspired Hydrogel Microrobots for On-Demand Anchoring and Cargo Delivery,” *Adv. Mater.*, vol. 35, no. 10, Mar. 2023.

[31] M. Sun *et al.*, “Magnetic Microswarm and Fluoroscopy-Guided Platform for Biofilm Eradication in Biliary Stents,” *Adv. Mater.*, vol. 34, no. 34, Aug. 2022.

[32] Y. Yan, T. Wang, R. Zhang, Y. Liu, W. Hu, and M. Sitti, “Magnetically assisted soft milli-tools for occluded lumen morphology detection,” *Sci. Adv.*, vol. 9, no. 33, Aug. 2023.

[33] C. Wang, Y. Wu, X. Dong, M. Armacki, and M. Sitti, “In situ sensing physiological properties of biological tissues using wireless miniature soft robots,” *Sci. Adv.*, vol. 9, no. 23, Jun. 2023.

[34] E. H. Wu *et al.*, “Procedural and interpretive skills of medical students: experiences and attitudes of fourth-year students.,” *Acad. Med.*, vol. 83, no. 10 Suppl, pp. 48–51, 2008.

[35] M. Sitti and D. S. Wiersma, “Pros and Cons: Magnetic versus Optical Microrobots,” *Adv. Mater.*, vol. 32, no. 20, p. 1906766, May 2020.

[36] M. Sitti, *Mobile Microrobotics*. Cambridge, MA: The MIT Press, 2017.

[37] M. Cianchetti, C. Laschi, A. Menciassi, and P. Dario, “Biomedical applications of soft robotics,” *Nat. Rev. Mater.*, vol. 3, no. 6, pp. 143–153, Jun. 2018.

[38] S. Fusco *et al.*, “An Integrated Microrobotic Platform for On-Demand, Targeted Therapeutic Interventions,” *Adv. Mater.*, vol. 26, no. 6, pp. 952–957, Feb. 2014.

[39] Y. Kim, G. A. Parada, S. Liu, and X. Zhao, “Ferromagnetic soft continuum robots,” *Sci. Robot.*, vol. 4, no. 33, p. eaax7329, Aug. 2019.

[40] T. Xu, J. Zhang, M. Salehizadeh, O. Onaizah, and E. Diller, “Millimeter-scale flexible robots with programmable three-dimensional magnetization and motions,” *Sci. Robot.*, vol. 4, no. 29, p. eaav4494, Apr. 2019.

[41] J. Cui *et al.*, “Nanomagnetic encoding of shape-morphing micromachines,” *Nature*, vol. 575, no. 7781, pp. 164–168, Nov. 2019.

[42] Y. Kim, H. Yuk, R. Zhao, S. A. Chester, and X. Zhao, “Printing ferromagnetic domains for untethered fast-transforming soft materials,” *Nature*, vol. 558, no. 7709, pp. 274–279, Jun. 2018.

[43] Z. Liu *et al.*, “High-Adhesion Stretchable Electrodes Based on Nanopile Interlocking,” *Adv. Mater.*, vol. 29, no. 2, p. 1603382, Jan. 2017.

[44] S. Y. Yang *et al.*, “A bio-inspired swellable microneedle adhesive for mechanical interlocking with tissue,” *Nat. Commun.*, vol. 4, no. 1, p. 1702, Jun. 2013.

[45] C. Hollinsky *et al.*, “Comparison of a New Self-Gripping Mesh with Other Fixation Methods for Laparoscopic Hernia Repair in a Rat Model,” *J. Am. Coll. Surg.*, vol. 208, no. 6, pp. 1107–1114, Jun. 2009.

[46] D.-M. Drotlef, M. Amjadi, M. Yunusa, and M. Sitti, “Bioinspired Composite Microfibers for Skin Adhesion and Signal Amplification of Wearable Sensors,” *Adv. Mater.*, vol. 29, no. 28, p. 1701353, Jul. 2017.

[47] V. Liimatainen, D. Drotlef, D. Son, and M. Sitti, “Liquid-Superrepellent Bioinspired Fibrillar Adhesives,” *Adv. Mater.*, vol. 32, no. 19, p. 2000497, May 2020.

[48] J. Giltinan, E. Diller, and M. Sitti, “Programmable assembly of heterogeneous microparts

by an untethered mobile capillary microgripper," *Lab Chip*, vol. 16, no. 22, pp. 4445–4457, 2016.

[49] Y. Wang, V. Kang, E. Arzt, W. Federle, and R. Hensel, "Strong Wet and Dry Adhesion by Cupped Microstructures," *ACS Appl. Mater. Interfaces*, vol. 11, no. 29, pp. 26483–26490, Jul. 2019.

[50] S. Song, D.-M. Drotlef, C. Majidi, and M. Sitti, "Controllable load sharing for soft adhesive interfaces on three-dimensional surfaces," *Proc. Natl. Acad. Sci.*, vol. 114, no. 22, pp. E4344–E4353, May 2017.

[51] S. Baik, D. W. Kim, Y. Park, T.-J. Lee, S. Ho Bhang, and C. Pang, "A wet-tolerant adhesive patch inspired by protuberances in suction cups of octopi," *Nature*, vol. 546, no. 7658, pp. 396–400, Jun. 2017.

[52] C. H. Fry and B. Vahabi, "The Role of the Mucosa in Normal and Abnormal Bladder Function," *Basic Clin. Pharmacol. Toxicol.*, vol. 119, pp. 57–62, Oct. 2016.

[53] W. Hoffmann, "Regeneration of the Gastric Mucosa and its Glands from Stem Cells," *Curr. Med. Chem.*, vol. 15, no. 29, pp. 3133–3144, Dec. 2008.

[54] R. Donnelly, R. Shaikh, T. Raj Singh, M. Garland, and Ad. Woolfson, "Mucoadhesive drug delivery systems," *J. Pharm. Bioallied Sci.*, vol. 3, no. 1, p. 89, 2011.

[55] S. Baik, J. Kim, H. J. Lee, T. H. Lee, and C. Pang, "Highly Adaptable and Biocompatible Octopus-Like Adhesive Patches with Meniscus-Controlled Unfoldable 3D Microtips for Underwater Surface and Hairy Skin," *Adv. Sci.*, vol. 5, no. 8, p. 1800100, Aug. 2018.

[56] S. Baik, H. J. Lee, D. W. Kim, H. Min, and C. Pang, "Capillarity-Enhanced Organ-Attachable Adhesive with Highly Drainable Wrinkled Octopus-Inspired Architectures," *ACS Appl. Mater. Interfaces*, vol. 11, no. 29, pp. 25674–25681, Jul. 2019.

[57] J. Li *et al.*, "Tough adhesives for diverse wet surfaces," *Science (80-.).*, vol. 357, no. 6349, pp. 378–381, Jul. 2017.

[58] T. Yu, G. P. Andrews, and D. S. Jones, "Mucoadhesion and Characterization of Mucoadhesive Properties," in *Mucosal Delivery of Biopharmaceuticals*, Boston, MA: Springer US, 2014, pp. 35–58.

[59] J. SMART, "The basics and underlying mechanisms of mucoadhesion," *Adv. Drug Deliv. Rev.*, vol. 57, no. 11, pp. 1556–1568, Nov. 2005.

[60] R. Bansil and B. S. Turner, "The biology of mucus: Composition, synthesis and organization," *Adv. Drug Deliv. Rev.*, vol. 124, pp. 3–15, Jan. 2018.

[61] A. Abramson *et al.*, "An ingestible self-orienting system for oral delivery of macromolecules," *Science (80-.).*, vol. 363, no. 6427, pp. 611–615, Feb. 2019.

[62] A. Abramson *et al.*, "A luminal unfolding microneedle injector for oral delivery of macromolecules," *Nat. Med.*, vol. 25, no. 10, pp. 1512–1518, Oct. 2019.

[63] A. T. Becker, O. Felfoul, and P. E. Dupont, "Toward tissue penetration by MRI-powered millirobots using a self-assembled Gauss gun," in *2015 IEEE International Conference on*

Robotics and Automation (ICRA), 2015, vol. 2015-June, no. June, pp. 1184–1189.

[64] J. Leclerc, A. Ramakrishnan, N. Tsekos, and A. Becker, "Magnetic Hammer Actuation for Tissue Penetration using a Millirobot," *IEEE Robot. Autom. Lett.*, vol. 3, no. 1, pp. 1–1, 2017.

[65] R. H. Soon *et al.*, "On-demand anchoring of wireless soft miniature robots on soft surfaces," *Proc. Natl. Acad. Sci.*, vol. 119, no. 34, pp. 1–11, Aug. 2022.

[66] Z. Ren, W. Hu, X. Dong, and M. Sitti, "Multi-functional soft-bodied jellyfish-like swimming," *Nat. Commun.*, vol. 10, no. 1, p. 2703, Dec. 2019.

[67] M. Mahvash and P. E. Dupont, "Mechanics of Dynamic Needle Insertion into a Biological Material," *IEEE Trans. Biomed. Eng.*, vol. 57, no. 4, pp. 934–943, Apr. 2010.

[68] J. W. Jewett and R. A. Serway, *Physics for scientists and engineers*, 7th ed. Thomson-Brooks/Cole, 2008.

[69] Henkel AG & Co., "Loctite ® 431^{TM} Technical Datasheet," 2010.

[70] C. F. Guimarães, L. Gasperini, A. P. Marques, and R. L. Reis, "The stiffness of living tissues and its implications for tissue engineering," *Nat. Rev. Mater.*, vol. 5, no. 5, pp. 351–370, May 2020.

[71] A. M. Okamura, C. Simone, and M. D. O'Leary, "Force Modeling for Needle Insertion Into Soft Tissue," *IEEE Trans. Biomed. Eng.*, vol. 51, no. 10, pp. 1707–1716, Oct. 2004.

[72] O. Thoumine and A. Ott, "Time scale dependent viscoelastic and contractile regimes in fibroblasts probed by microplate manipulation," *J. Cell Sci.*, vol. 110, no. 17, pp. 2109–2116, Sep. 1997.

[73] S. Jiang, P. Li, Y. Yu, J. Liu, and Z. Yang, "Experimental study of needle–tissue interaction forces: Effect of needle geometries, insertion methods and tissue characteristics," *J. Biomech.*, vol. 47, no. 13, pp. 3344–3353, Oct. 2014.

[74] M. Fisk, "Induction Heating," in *Encyclopedia of Thermal Stresses*, R. B. Hetnarski, Ed. Dordrecht: Springer Netherlands, 2014, pp. 2419–2426.

[75] A. Costa-Ferreira, P. Rodrigues-Pereira, M. Rebelo, L. O. Vásconez, and J. Amarante, "Morphometric Study (Macroscopic and Microscopic) of the Lower Abdominal Wall," *Plast. Reconstr. Surg.*, vol. 134, no. 6, pp. 1313–1322, Dec. 2014.

[76] S. R. Khan *et al.*, "Kidney stones," *Nat. Rev. Dis. Prim.*, vol. 2, no. 1, p. 16008, Dec. 2016.

[77] A. C. Barnett, Y.-S. Lee, and J. Z. Moore, "Fracture Mechanics Model of Needle Cutting Tissue," *J. Manuf. Sci. Eng.*, vol. 138, no. 1, pp. 1–8, Jan. 2016.

[78] M. Oyen-Tiesma and R. F. Cook, "Technique for estimating fracture resistance of cultured neocartilage," *J. Mater. Sci. Mater. Med.*, vol. 12, no. 4, pp. 327–332, 2001.

[79] K. Koombua, R. M. Pidaparti, and M. W. Beatty, "Fracture toughness estimation for the TMJ disc," *J. Biomed. Mater. Res. Part A*, vol. 79A, no. 3, pp. 566–573, Dec. 2006.

[80] M. V. Chin-Purcell and J. L. Lewis, "Fracture of Articular Cartilage," *J. Biomech. Eng.*,

vol. 118, no. 4, pp. 545–556, Nov. 1996.

[81] D. Taylor, N. O'Mara, E. Ryan, M. Takaza, and C. Simms, "The fracture toughness of soft tissues," *J. Mech. Behav. Biomed. Mater.*, vol. 6, pp. 139–147, Feb. 2012.

[82] Z. Chen *et al.*, "Additive Manufacturing of Honeybee-Inspired Microneedle for Easy Skin Insertion and Difficult Removal," *ACS Appl. Mater. Interfaces*, vol. 10, no. 35, pp. 29338–29346, Sep. 2018.

[83] D. Han *et al.*, "4D Printing of a Bioinspired Microneedle Array with Backward-Facing Barbs for Enhanced Tissue Adhesion," *Adv. Funct. Mater.*, vol. 30, no. 11, p. 1909197, Mar. 2020.

[84] W. K. Cho *et al.*, "Microstructured barbs on the North American porcupine quill enable easy tissue penetration and difficult removal," *Proc. Natl. Acad. Sci.*, vol. 109, no. 52, pp. 21289–21294, Dec. 2012.

[85] P. C. Benias and D. L. Carr-Locke, "Principles of Electrosurgery," in *ERCP*, Elsevier, 2019, pp. 86-92.e1.

[86] N. N. Massarweh, N. Cosgriff, and D. P. Slakey, "Electrosurgery: History, Principles, and Current and Future Uses," *J. Am. Coll. Surg.*, vol. 202, no. 3, pp. 520–530, Mar. 2006.

[87] M. Shang, R. H. Soon, C. T. Lim, B. L. Khoo, and J. Han, "Microfluidic modelling of the tumor microenvironment for anti-cancer drug development," *Lab Chip*, vol. 19, no. 3, pp. 369–386, 2019.

[88] S. E. Chung, X. Dong, and M. Sitti, "Three-dimensional heterogeneous assembly of coded microgels using an untethered mobile microgripper," *Lab Chip*, vol. 15, no. 7, pp. 1667–1676, 2015.

[89] J. Zhang, Y. Guo, W. Hu, and M. Sitti, "Wirelessly Actuated Thermo- and Magneto-Responsive Soft Bimorph Materials with Programmable Shape-Morphing," *Adv. Mater.*, vol. 33, no. 30, p. 2100336, Jul. 2021.

[90] J. Zhang, Y. Guo, W. Hu, R. H. Soon, Z. S. Davidson, and M. Sitti, "Liquid Crystal Elastomer-Based Magnetic Composite Films for Reconfigurable Shape-Morphing Soft Miniature Machines," *Adv. Mater.*, vol. 33, no. 8, p. 2006191, Feb. 2021.

[91] M. G. Geeslin and E. N. Cressman, "Thermochemical Ablation: A Device for a Novel Interventional Concept," *J. Med. Devices, Trans. ASME*, vol. 6, no. 1, pp. 1–5, 2012.

[92] Z. Guo, Q. Zhang, X. Li, and Z. Jing, "Thermochemical ablation therapy of VX2 tumor using a permeable oil-packed liquid," *PLoS One*, vol. 10, no. 4, pp. 1–11, 2015.

[93] E. N. K. Cressman *et al.*, "Concentration and volume effects in thermochemical ablation in vivo: Results in a porcine model," *Int. J. Hyperth.*, vol. 28, no. 2, pp. 113–121, 2012.

[94] Z. Izadifar, Z. Izadifar, D. Chapman, and P. Babyn, "An introduction to high intensity focused ultrasound: Systematic review on principles, devices, and clinical applications," *J. Clin. Med.*, vol. 9, no. 2, pp. 1–22, 2020.

[95] A. Stabile *et al.*, "Medium-term oncological outcomes in a large cohort of men treated with

either focal or hemi-ablation using high-intensity focused ultrasonography for primary localized prostate cancer," *BJU Int.*, vol. 124, no. 3, pp. 431–440, 2019.

[96] L. Zhu *et al.*, "Ultrasound Hyperthermia Technology for Radiosensitization," *Ultrasound Med. Biol.*, vol. 45, no. 5, pp. 1025–1043, May 2019.

[97] V. Rudnev, D. Loveless, R. L. Cook, and M. Black, *Handbook of Induction Heating.* CRC Press, 2002.

[98] S. M. Mirvakili, D. Sim, I. W. Hunter, and R. Langer, "Actuation of untethered pneumatic artificial muscles and soft robots using magnetically induced liquid-to-gas phase transitions," *Sci. Robot.*, vol. 5, no. 41, p. eaaz4239, Apr. 2020.

[99] S. Kumar *et al.*, "Curcumin and 5-Fluorouracil-loaded, folate- and transferrin-decorated polymeric magnetic nanoformulation: a synergistic cancer therapeutic approach, accelerated by magnetic hyperthermia," *Int. J. Nanomedicine*, p. 437, Jan. 2014.

[100] B. Thiesen and A. Jordan, "Clinical applications of magnetic nanoparticles for hyperthermia," *Int. J. Hyperth.*, vol. 24, no. 6, pp. 467–474, Jan. 2008.

[101] M. Johannsen, B. Thiesen, P. Wust, and A. Jordan, "Magnetic nanoparticle hyperthermia for prostate cancer," *Int. J. Hyperth.*, vol. 26, no. 8, pp. 790–795, Dec. 2010.

[102] F. K. H. van Landeghem *et al.*, "Post-mortem studies in glioblastoma patients treated with thermotherapy using magnetic nanoparticles," *Biomaterials*, vol. 30, no. 1, pp. 52–57, 2009.

[103] M. B. Bilgin, M. E. Tiryaki, J. Lazovic, and M. Sitti, "Radio Frequency Sensing-Based In Situ Temperature Measurements during Magnetic Resonance Imaging Interventional Procedures," *Adv. Mater. Technol.*, vol. 7, no. 9, p. 2101625, Sep. 2022.

[104] C.-C. Yeh and Y.-J. Yang, "An RF-Powered Wireless Micro-Heater Integrated with Acrylate-Composite-Based Temperature Regulator for Hyperthermia Treatment," *2020 IEEE 33rd Int. Conf. Micro Electro Mech. Syst.*, pp. 357–360, Jan. 2020.

[105] S. Jeon *et al.*, "A Magnetically Controlled Soft Microrobot Steering a Guidewire in a Three-Dimensional Phantom Vascular Network," *Soft Robot.*, vol. 6, no. 1, pp. 54–68, 2019.

[106] S. Charkhabi, Y. J. Chan, D. Hwang, S. T. Frey, M. D. Bartlett, and N. F. Reuel, "Kirigami-Enabled, Passive Resonant Sensors for Wireless Deformation Monitoring," *Adv. Mater. Technol.*, vol. 4, no. 5, p. 1800683, May 2019.

[107] T. Voigt, U. Katscher, and O. Doessel, "Quantitative conductivity and permittivity imaging of the human brain using electric properties tomography," *Magn. Reson. Med.*, vol. 66, no. 2, pp. 456–466, Aug. 2011.

[108] B. Wang, W. Yang, V. R. Sherman, and M. A. Meyers, "Pangolin armor: Overlapping, structure, and mechanical properties of the keratinous scales," *Acta Biomater.*, vol. 41, pp. 60–74, Sep. 2016.

[109] M. Adler, "A field-theoretical approach to magnetic induction heating of thin circular plates," *IEEE Trans. Magn.*, vol. 10, no. 4, pp. 1118–1125, Dec. 1974.

[110] J. S. Park, S. Taniguchi, and Y. J. Park, "Maximum Joule heat by tubular susceptor with

critical thickness on induction heating," *J. Phys. D. Appl. Phys.*, vol. 42, no. 4, p. 045509, Feb. 2009.

[111] N. Tsopelas and N. J. Siakavellas, "Influence of Some Parameters on the Effectiveness of Induction Heating," *IEEE Trans. Magn.*, vol. 44, no. 12, pp. 4711–4720, Dec. 2008.

[112] M. Frivaldsky, M. Pavelek, and T. Donic, "Modeling and Experimental Verification of Induction Heating of Thin Molybdenum Sheets," *Appl. Sci.*, vol. 11, no. 2, p. 647, Jan. 2021.

[113] W. Yang, I. H. Chen, B. Gludovatz, E. A. Zimmermann, R. O. Ritchie, and M. A. Meyers, "Natural Flexible Dermal Armor," *Adv. Mater.*, vol. 25, no. 1, pp. 31–48, Jan. 2013.

[114] R. Martini and F. Barthelat, "Stretch-and-release fabrication, testing and optimization of a flexible ceramic armor inspired from fish scales," *Bioinspir. Biomim.*, vol. 11, no. 6, p. 066001, Oct. 2016.

[115] I. H. Chen *et al.*, "Armadillo armor: Mechanical testing and micro-structural evaluation," *J. Mech. Behav. Biomed. Mater.*, vol. 4, no. 5, pp. 713–722, Jul. 2011.

[116] I. H. Chen, W. Yang, and M. A. Meyers, "Alligator osteoderms: Mechanical behavior and hierarchical structure," *Mater. Sci. Eng. C*, vol. 35, pp. 441–448, Feb. 2014.

[117] C. Williams *et al.*, "A review of the osteoderms of lizards (Reptilia: Squamata)," *Biol. Rev.*, vol. 97, no. 1, pp. 1–19, Feb. 2022.

[118] D. J. Griffiths, *Introduction to Electrodynamics*. Cambridge University Press, 2017.

[119] Jack P. Holman, *Heat Transfer*, Tenth Edit. New York: McGraw-Hill, 2010.

[120] S. Acharya, H. P. Sharma, R. Bhattarai, B. Poudyal, S. Sharma, and S. Upadhaya, "Distribution and habitat preferences of the Chinese Pangolin Manis pentadactyla (Mammalia: Manidae) in the mid-hills of Nepal," *J. Threat. Taxa*, vol. 13, no. 8, pp. 18959–18966, Jul. 2021.

[121] L. Hua *et al.*, "Captive breeding of pangolins: current status, problems and future prospects," *Zookeys*, vol. 507, pp. 99–114, Jun. 2015.

[122] Y. Alapan, A. C. Karacakol, S. N. Guzelhan, I. Isik, and M. Sitti, "Reprogrammable shape morphing of magnetic soft machines," *Sci. Adv.*, vol. 6, no. 38, p. eabc6414, Sep. 2020.

[123] D. Zaidi, L. Churchill, H. Q. Huynh, M. W. Carroll, R. Persad, and E. Wine, "Capillary Flow Rates in the Duodenum of Pediatric Ulcerative Colitis Patients Are Increased and Unrelated to Inflammation," *J. Pediatr. Gastroenterol. Nutr.*, vol. 65, no. 3, pp. 306–310, Sep. 2017.

[124] N. Ohmiya *et al.*, "Diagnosis and treatment of obscure GI bleeding at double balloon endoscopy," *Gastrointest. Endosc.*, vol. 66, no. 3, pp. S72–S77, Sep. 2007.

[125] P. Wust *et al.*, "Hyperthermia in combined treatment of cancer," *Lancet Oncol.*, vol. 3, no. 8, pp. 487–497, Aug. 2002.

[126] M. Shinkai, M. Yanase, H. Honda, T. Wakabayashi, J. Yoshida, and T. Kobayashi, "Intracellular Hyperthermia for Cancer Using Magnetite Cationic Liposomes: In vitro

Study," *Japanese J. Cancer Res.*, vol. 87, no. 11, pp. 1179–1183, Nov. 1996.

[127] M. Yanase, M. Shinkai, H. Honda, T. Wakabayashi, J. Yoshida, and T. Kobayashi, "Antitumor Immunity Induction by Intracellular Hyperthermia Using Magnetite Cationic Liposomes," *Japanese J. Cancer Res.*, vol. 89, no. 7, pp. 775–782, Jul. 1998.

[128] A. Ito *et al.*, "Heat shock protein 70 expression induces antitumor immunity during intracellular hyperthermia using magnetite nanoparticles," *Cancer Immunol. Immunother.*, vol. 52, no. 2, pp. 80–88, Feb. 2003.

[129] B. Le *et al.*, "Preparation of Tumor-Specific Magnetoliposomes and Their Application for Hyperthermia.," *J. Chem. Eng. JAPAN*, vol. 34, no. 1, pp. 66–72, 2001.

[130] A. Jordan *et al.*, "The effect of thermotherapy using magnetic nanoparticles on rat malignant glioma," *J. Neurooncol.*, vol. 78, no. 1, pp. 7–14, May 2006.

[131] I. Rabias *et al.*, "Rapid magnetic heating treatment by highly charged maghemite nanoparticles on Wistar rats exocranial glioma tumors at microliter volume," *Biomicrofluidics*, vol. 4, no. 2, pp. 1–8, 2010.

[132] K. Maier-Hauff *et al.*, "Intracranial thermotherapy using magnetic nanoparticles combined with external beam radiotherapy: Results of a feasibility study on patients with glioblastoma multiforme," *J. Neurooncol.*, vol. 81, no. 1, pp. 53–60, 2007.

[133] K. Maier-Hauff *et al.*, "Efficacy and safety of intratumoral thermotherapy using magnetic iron-oxide nanoparticles combined with external beam radiotherapy on patients with recurrent glioblastoma multiforme," *J. Neurooncol.*, vol. 103, no. 2, pp. 317–324, 2011.

[134] ClinicalTrials.gov, "Study of Focal Ablation of the Prostate With NanoTherm® Therapy System for Intermediate-Risk Prostate CancerNo Title," 2022. [Online]. Available: https://clinicaltrials.gov/ct2/show/study/NCT05010759. [Accessed: 21-Oct-2022].

[135] Z. Yang and L. Zhang, "Magnetic Actuation Systems for Miniature Robots: A Review," *Adv. Intell. Syst.*, vol. 2, no. 9, p. 2000082, Sep. 2020.

[136] R. H. Soon *et al.*, "Pangolin-inspired untethered magnetic robot for on-demand biomedical heating applications," *Nat. Commun.*, vol. 14, no. 1, p. 3320, Jun. 2023.

[137] C. Wan and C. R. Bowen, "Multiscale-structuring of polyvinylidene fluoride for energy harvesting: the impact of molecular-, micro- and macro-structure," *J. Mater. Chem. A*, vol. 5, no. 7, pp. 3091–3128, 2017.

[138] V. T. Rathod, "A Review of Acoustic Impedance Matching Techniques for Piezoelectric Sensors and Transducers," *Sensors*, vol. 20, no. 14, p. 4051, Jul. 2020.

[139] G. Hong, A. L. Antaris, and H. Dai, "Near-infrared fluorophores for biomedical imaging," *Nat. Biomed. Eng.*, vol. 1, no. 1, p. 0010, Jan. 2017.

[140] "Therapeutic Drug Use," *National Center for Health Statistics*, 2023. [Online]. Available: https://www.cdc.gov/nchs/fastats/drug-use-therapeutic.htm. [Accessed: 01-May-2023].